A study of the effects of spatially localized time-delayed feedback schemes on spatio-temporal patterns

Jason Edward Czak

Dissertation submitted to the Faculty of the
Virginia Polytechnic Institute and State University
in partial fulfillment of the requirements for the degree of

Doctor of Philosophy
in
Physics

Michel Pleimling, Chair
Uwe C. Täuber
Shengfeng Cheng
Leo E. Piilonen

May 2, 2022
Blacksburg, Virginia

Keywords: non-equilibrium systems, chaos, control theory, pattern formations

A study of the effects of spatially localized time-delayed feedback schemes on spatio-temporal patterns

Jason Edward Czak

(ABSTRACT)

In typical attempts to control spatio-temporal chaos, spatially extended systems were subjected to protocols that perturbed them as a whole, often overlooking the potential stabilizing interaction between adjacent regions. We have shown that through the application of a time-delayed feedback scheme to a specific localized region of a system periodic patterns can be generated that are distinct from those observed when controlling the whole system. In this thesis, we present the results of two interconnected studies:

1) Spatio-temporal patterns emerging from spatially localized time-delayed feedback perturbations within transient chaotic states of the Gray-Scott reaction-diffusion system

2) Spatio-temporal patterns emerging from spatially localized time-delayed feedback perturbations within chaotic states of the cubic complex Ginzburg-Landau equation

We present an investigation of two model systems: the Gray-Scott reaction-diffusion equation and the complex Ginzburg-Landau equation. Specifically we numerically study two models characterized by exhibiting various chaotic regimes.

We first consider a comprehensive study of the Gray-Scott model highlighting key details about different parameter space regimes and their relative proximity to the chaotic regime. Through a systematic investigation of the effects of the model control parameters, time-delayed feedback control strength parameters, perturbed region widths, and other quantities, we show that novel patterns can be formed through the appropriate choice of perturbation region and strength.

For the second study we use spatially localized time-delayed feedback on the one-dimensional complex Ginzburg-Landau equation and demonstrate, through the numerical integration of the resulting real and imaginary equations, the stabilization of novel periodic patterns within three distinct chaotic regimes.

In these studies we have shown that selectively applying a time-delayed feedback scheme to a specific spatially localized region of a chaotic system can bring forth periodic patterns that are distinct from those observed when applying a perturbation to the whole system. Depending on the protocol used, these new patterns can emerge either in the perturbed or the unperturbed region. The mechanism underlying the observed pattern generation is related to the interplay between diffusion across the interfaces separating the different regions and time-delayed feedback.

Research was sponsored by the Army Research Office and was accomplished under Grant No. **W911NF-17-1-0156**.

A study of the effects of spatially localized time-delayed feedback schemes on spatio-temporal patterns

Jason Edward Czak

(GENERAL AUDIENCE ABSTRACT)

In typical attempts to control spatio-temporal chaos, spatially extended systems were subjected to protocols that perturbed them as a whole, often overlooking the potential stabilizing interaction between adjacent regions. We have shown that through the application of a time-delayed feedback scheme to a specific localized region of a system periodic patterns can be generated that are distinct from those observed when controlling the whole system.

We present an investigation of two model systems: the Gray-Scott reaction-diffusion equation and the complex Ginzburg-Landau equation. We first consider a comprehensive study of the Gray-Scott model highlighting key details about different parameter space regimes and their relative proximity to the chaotic regime. Through a systematic investigation of the effects of the model control parameters, time-delayed feedback control strength parameters, perturbed region widths, and other quantities, we show that novel patterns can be formed through the appropriate choice of perturbation region and strength.

For the second study we use spatially localized time-delayed feedback on the one-dimensional complex Ginzburg-Landau equation and demonstrate, through the numerical integration of the resulting real and imaginary equations, the stabilization of novel periodic patterns within chaotic regimes.

In these studies we have shown that selectively applying a time-delayed feedback scheme to a specific region of a chaotic system can generate periodic patterns that are distinct from those observed when controlling the whole system. Depending on the protocol used, these new patterns can emerge either in the perturbed or the unperturbed region. The mechanism underlying the observed pattern generation is related to the interplay between diffusion across the interfaces separating the different regions and time-delayed feedback.

Research was sponsored by the Army Research Office and was accomplished under Grant No. **W911NF-17-1-0156**.

I dedicate this work to my family who have supported me in all stages of my life.

Acknowledgments

First and foremost, I thank my advisor, Professor Michel Pleimling, for his support, advice, and encouragement throughout my development as a researcher. This would not have been possible without him, and I have greatly valued my time as his student.

Thanks to Professor Uwe C. Täuber for constructive feedback and helpful discussions sharing his expertise. I also thank my committee members, Professor Shengfeng Cheng and Professor Leo Piilonen, and the chair of the graduate committee, Professor Camillo Mariani. I thank them all for their support along the way. My gratitude extends to Professor John Simonetti, and Alma Robinson for teaching me the value of exceptional teaching.

A special thanks to Dr. Karen DePauw for her support during my formulate time as a graduate student at Virginia Tech. I express my sincerest gratitude to Dr. Robyn Hudson and Deborah Smith for helping me through a difficult time in the early stages of my graduate career. I thank Professor James Gray for his kind and persistent support during the time of my qualifier examination. I thank Dr. Catherine Dugan for her support over many years.

I am grateful for the administrative staff of the physics department, especially Katrina Loan, and Betty Wilkins, who have gone above and beyond the call of duty when dealing with all things administrative. I appreciate Roger Link and Travis Heath for their support in the IT department with their willingness to help especially during the time of Covid-19.

I would like to thank the people that made my time in Blacksburg a bit brighter, in a random order: John Burton, Donovan Buterakos, Rebekah Pestes, Narae Yu, Ying Shen, Ian Sandum, Britannia Vondrasek, Bart Brown, Ahmadreza Azizi, Jacob Carroll, Priyanka, Taylor Kimmel, Dennis Kiptoo, Yifei Wang, Teshani Omanthika and many others. Many thanks to my friends from Virginia Tech who have all helped me along the way. I appreciate and cherish the times spent with my friends at BCF, I thank you all for your caring and support. A special thanks to Justin Petucci who has been a true friend for so long has become family.

And last but by no means least, a loving thanks goes to my Pam for her ever-present love and support. The whole world becomes a much brighter place with the future we will share in mind.

Contents

List of Figures

List of Tables

Chapter 1

Introduction

1.1 Spatio-temporal patterns

We begin this dissertation with an introduction to spatio-temporal patterns to motivate the later chapters. An overview of the remaining chapters is given at the end.

The formation of spatio-temporal patterns [1, 2] is ubiquitous in the physical world and these patterns are found at scales ranging from the micro scale, magnon interactions within time crystals [3], to the largest observed scales, as for example galaxy superclusters [4] or the Sloan Great Wall [5].

Understanding the complexities of spatio-temporal patterns has been of keen interest to physicists for centuries. Like the tessellation of hexagons found in Henri Bénard's work [6] on the stability of a thin fluid layer open to air and exposed to a vertical temperature gradient, first explained by Rayleigh and further expanded upon by Pearson [1], the field of observing and quantifying spatio-temporal patterns experiences developments as rich as the patterns themselves.

Controlling and designing space-time patterns has numerous potential applications. The goal is often either to design patterns and influence traveling waves or to move a chaotic system to a steady state or to an oscillatory behavior [7, 8, 9, 10, 11, 12, 13]. Experimentally, this control is achieved by exerting some external perturbation, involving for example modulated light pulse or voltage variations [14] when designing optical systems. The two fundamental keystones of chaos control protocols are the Ott-Grebogi-Yorke scheme [7] and time-delayed feedback control [8].

The use of time-delayed feedback schemes has shown tremendous usefulness to experimental systems [15, 16, 17, 18, 19, 20]. Numerical simulations results have been used to guide experimental findings. For instance numerical simulation results to guide laser control experiments have been used for control of the unstable orbits of a CO_2 laser with modulated

losses by Bielawski et al [15]. The application of an adjustable time-delayed feedback routine within a localized region of a rabbit heart was used to suppress an alternans rhythm type cardiac arrhythmia [16]. The effects of time-delayed feedback on spatio-temporal structures are well studied [21, 22, 23]. Studies explicitly focusing on the effects of spatially localized time-delayed feedback perturbations are lacking in quantity. This prompts us to undertake a study focusing on the effects of applying spatially localized perturbations to systems exhibiting spatio-temporal patterns.

We can start with a simple definition of what a spatio-temporal pattern is in the broad sense. A physical variable within a model can be represented as a spatio-temporal data set when we have a system that changes properties across space and time. One easy example to think of would be the formation of patterns from throwing a rock into a puddle. At the moment of impact the ripples that form on the surface of the pond will create a pattern across the spatial dimensions of the puddle that propagates outward as time moves forward. The collection of individual snapshots of the pond will be the spatio-temporal representation of the system.

1.2 Gray-Scott Reaction-Diffusion model

The Gray-Scott model system is a variant of the auto-catalytic Sel'kov model of glycolysis [24], consequently named after Peter Gray and Peter K. Scott for their groundbreaking work on "Autocatalytic reactions in the isothermal continuous stirred tank reactor" [25]. As claimed in their original body of work the model system is one of the simplest to exhibit exotic behaviors, often observed in the form of various space-time patterns. As such this model exhibits a wide range of spatio-temporal patterns in response to finite amplitude perturbations.

The Gray-Scott model is a simple reaction-diffusion system that displays very rich and complex space-time patterns in one and two space dimensions. The two-reaction scheme can be expressed as [26]

$$U + 2V \rightarrow 3V \qquad \text{chemical reaction rate} = k_1 uv^2, \tag{1.1}$$

$$V \rightarrow P \qquad \text{chemical reaction rate} = k_2 v, \tag{1.2}$$

where we have k_1 as the rate of converting U to V, and k_2 the rate of decay of V to inert product P. Using a mean field approximation to the chemical reactions above, we can express the relation of the rates of the chemical steps to the inflow or outflow rates, or the Mass Balance equations as:

$$\frac{du}{dt} = -k_1 uv^2 + k_f(u_0 - u) \tag{1.3}$$

$$\frac{dv}{dt} = k_1 uv^2 - k_2 v + k_f(v_0 - v) \tag{1.4}$$

The quantities u_0 and v_0 are the concentrations of u and v in the inlet stream. The quantity k_f is the inverse of the average time each molecule spends within the system, often labeled as the mean residence time [25]. If the condition is applied that the inlet stream is a feed of u only without v present, the second equation reduces to

$$\frac{dv}{dt} = k_1 uv^2 - k_2 v - k_f v = k_1 uv^2 - (k_2 + k_f)v. \tag{1.5}$$

A reference to a steady state solution [26] is used to normalize the unit-less concentration densities to 1 by dividing through by k_1 giving

$$\frac{du}{dt} = -uv^2 + \underbrace{\frac{k_f}{k_1}}_{A}(\underbrace{u_0}_{1} - u) \tag{1.6}$$

$$\frac{dv}{dt} = uv^2 - (\underbrace{\frac{k_2}{k_1}}_{B} + \underbrace{\frac{k_f}{k_1}}_{A})v \tag{1.7}$$

Therefore with this the cubic autocatalytic system in an open flow reactor is governed by the reactions:

$$U + 2V \longrightarrow 3V, \qquad V \longrightarrow P, \tag{1.8}$$

where the substrate U is continuously supplied. This form of the reaction is irreversible, meaning that the inert product, P, will be removed by the outlet stream. The Gray-Scott model is of the activation-substrate depletion type. Therefore, the two concentrations u and v tend to vary opposite to one another. The corresponding deterministic kinetic equations for the space- and time-dependent species concentration densities $u(\mathbf{x}, t)$ and $v(\mathbf{x}, t)$ with diffusion is often cast in the following form

$$\frac{\partial u}{\partial t} = D_u \nabla^2 u - uv^2 + A(1 - u) \tag{1.9}$$

$$\frac{\partial v}{\partial t} = D_v \nabla^2 v + uv^2 - (A + B)v \tag{1.10}$$

with the species-dependent diffusion rates D_u and D_v. We can see from equations 1.9 and 1.10 that A is the re-scaled U feed rate and $A + B$ is the effective removal rate of V. The parameter B represents the re-scaled rate of converting V to an inert product. The inflow stream A, containing only substrate, acts to lower the overall activator concentration. For the different ratios of the diffusion coefficients we see much different patterns forming for the A,B parameter space [27]. For $D_u \gg D_v$ propagating pulses and pulse splittings dominate, for $D_u \gtrsim D_v$ a variety of regimes, including traveling pulses, spatio-temporal chaos, and self-replicating patterns, are encountered. This will be further explored in Chapters 2 and 3.

1.3 Complex Ginzburg-Landau equation

The complex Ginzburg-Landau equation (CGLe) is a well studied equation in the fields of physics and mathematics. It can be used to model and describe a large number of phenomena within the physical world. Some of the phenomena that can be quantitatively described are second order phase transitions, superfluidity, superconductivity, and Rayleigh-Bénard convection [1]. With this model being well studied, there is a collection of well written resources going over the various details and applications of the complex Ginzburg-Landau equation [28]. The cubic complex Ginzburg-Landau equation (CGLe) in one space dimension is a nonlinear partial differential equation that reads as follows [29]:

$$\frac{\partial A_c}{\partial t} = A_c + (1 + i\alpha)\frac{\partial^2}{\partial x^2}A_c - (1 + i\beta)|A_c|^2 A_c, \tag{1.11}$$

where we have the complex field $A_c(x,t) = \rho(x,t)e^{i\phi(x,t)}$ with modulus $\rho(x,t)$ and phase $\phi(x,t)$. We have α as the linear dispersion coefficient and β as the nonlinear dispersion coefficient.

To apply integration schemes we can separate the complex field $A_c(x,t)$ into its real and imaginary components, $A_c(x,t) = A_r(x,t) + iA_i(x,t)$. We then can represent the equation as two coupled partial differential equations given as:

$$\frac{\partial}{\partial t}A_r = A_r + \frac{\partial^2}{\partial x^2}A_r - |A_c|^2 A_r - \alpha\frac{\partial^2}{\partial x^2}A_i + \beta|A_c|^2 A_i, \tag{1.12}$$

$$\frac{\partial}{\partial t}A_i = A_i + \frac{\partial^2}{\partial x^2}A_i - |A_c|^2 A_i + \alpha\frac{\partial^2}{\partial x^2}A_r - \beta|A_c|^2 A_r. \tag{1.13}$$

The system exhibits a variety of different dynamic regimes. The attention of this work is focused to within regimes that exhibits spatio-temporal chaos. The spatio-temporal chaotic regimes are defect turbulence, or amplitude turbulence (AT), phase turbulence (PT), and bi-chaos. Shown in previous works [30], the values of the linear and nonlinear dispersion dictate the chaotic properties of the system. The complex Ginzburg-Landau equation will be at the center of chapter 4 where we will explore in detail perturbation induced patterns.

1.4 Spatio-temporal chaos

Dynamical systems are systems whose state varies over time and can be represented by differential equations. The system can be expressed as a function describing the time dependency of the points in space. In order for the system to be a deterministic dynamical system the future and present state must be directly obtained from the past states. This is a way of saying that there are no random fluctuations or noisy behavior within the system.

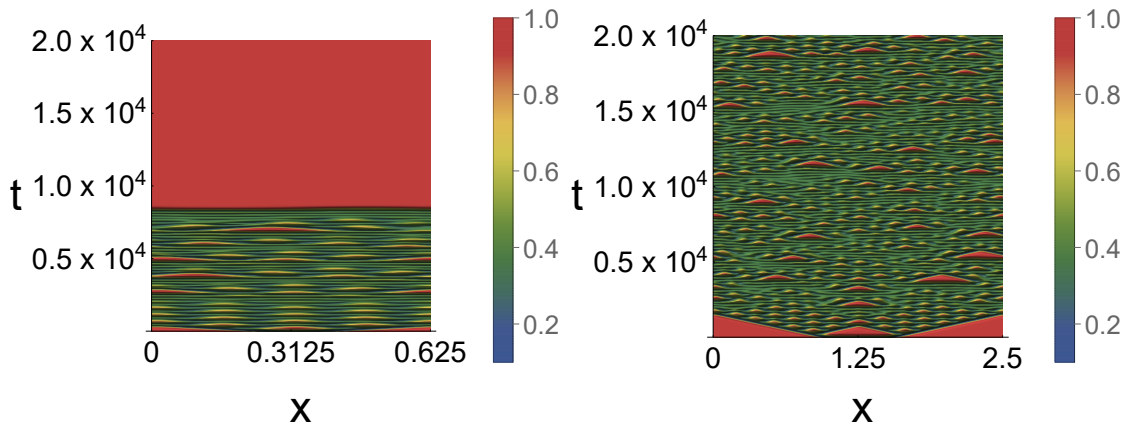

Figure 1.1: The Gray-Scott model exhibits transient chaos where the lifetime of the chaotic behavior depends on the size of the system [34]. The left figure shows that in a small system transient chaos dies out quickly. In the larger system shown in the right figure, the chaotic system persists for as long as the system's temporal evolution is followed.

A way to define aperiodic in the sense we are about to use is when the long term or asymptotic behavior of a trajectory will not settle down into periodic patterns, or to fixed points. In simpler words the system will continue on without established order for all of time.

A system's sensitivity is how much by changing one control parameter the system's overall trajectory changes. With some understanding of the above we can now define deterministic chaos. Deterministic chaos is an aperiodic long term behavior observed within a deterministic system that has a high level of sensitivity to initial system states or conditions [31, 32].

An interesting aspect of chaos is that is it typically defined with reference to a never ending time window. By a practical standpoint an experiment to test the full extent of chaos would require infinite amount of time. As expressed in [33] a well defined separation of time scales is needed to observe chaos. If we can define an internal system characteristic time t_{sys}, we use this as a unit of time. After some time the appearance of chaotic behavior occurs where we can define the average life time of these chaotic signals as T_C, or the chaotic time. For the observation of chaotic behavior it is required that $T_C >> t_{sys}$. For the standard or sustained chaos the value of $T_C = \infty$, whereas for transient chaos it is finite.

A more readily understandable explanation of the above definition of chaos is to use specific examples within the Gray-Scott and complex Ginzburg-Landau equation models. The first Fig. 1.1 displays the transient nature of the Gray-Scott model's chaotic regime, showing that for different spatial lattice sizes the chaotic behavior diminishes after some lifetime related to the system size [34] and initial perturbation. Fig. 1.2 shows that for the complex Ginzburg-Landau equation highly diverging trajectories result from slight changes in initial conditions, a behavior typical for chaos.

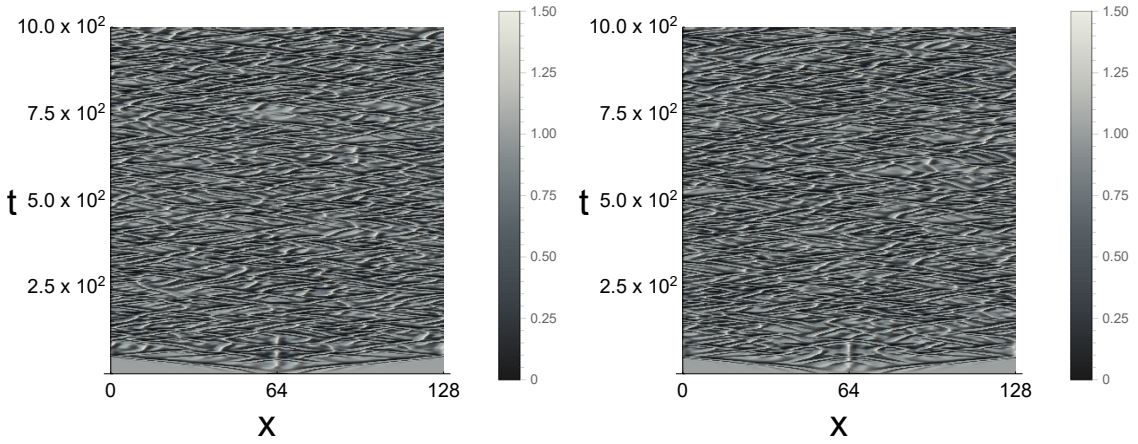

Figure 1.2: The complex Ginzburg-Landau equation system exhibits sustained chaos. The system was subjected to initial conditions with an inhomogeneous initial state with different widths. We have $h_t = 0.01$, whereas the grid size $h_x = 0.25$. Left: initial inhomogeneous width = 8, right: initial inhomogeneous width = 16. A large sensitivity to the initial condition is observed.

1.5 Overview

In this Chapter the models and a brief introduction to chaos were given. We also presented the motivation for our study: applying spatially localized perturbations to systems exhibiting spatio-temporal patterns with a focus on creating novel patterns. The main focus has been on systems with chaotic regimes due to their ubiquity in real physical systems [35, 36, 37]. The following chapters will build up the background and framework needed to understand and appreciate the significance of using a spatially localized setting to create novel patterns within chaotic systems.

In Chapter 2 we give a formal introduction to the specific methods and protocols used to numerically investigate and manipulate chaotic systems. The iteration methods used, discretization schemes, perturbation routines, and analysis techniques will be explored and explained.

In Chapter 3 the first model, the Gray-Scott model, will be thoroughly explained and the key findings will be shown. In Chapter 4 the second system, the complex Ginzburg-Landau equation, will be discussed along similar lines.

In Chapter 5 the method applied to the two systems to create novel patterns will be summarized and implications to other chaos producing systems will be discussed. Futures areas of potential research will be discussed in the context of localized perturbations.

Chapter 2

Numerical Methods and Models Used

2.1 Introduction

In this chapter the methods and techniques used within the works of chapters 3 and 4 will be explained in detail with emphasis on what is necessary to understand and explore the main results of those chapters. The Gray-Scott reaction-diffusion model will be used to explore and explain the different methods.

2.2 Discretization methods

The systems being dealt with are represented as nonlinear differential equations. A simple example, using one of the nonlinear systems being studied, gives an introduction to the methods. For the case of the Gray-Scott model finite-difference methods (FDM) can be employed to integrate the rate laws to find the concentration densities of u and v at later times. From equations 1.9 and 1.10 the one-dimensional case can be expressed as

$$\frac{\partial}{\partial t}u(x,t) = \mathrm{D}_u\nabla^2(x,t) - u(x,t)v(x,t)^2 + A[1-u(x,t)] \ , \tag{2.1}$$

$$\frac{\partial}{\partial t}v(x,t) = \mathrm{D}_v\nabla^2 v(x,t) + u(x,t)v(x,t)^2 - (A+B)v(x,t). \tag{2.2}$$

The system can be represented by using a low order finite-difference method. The one-dimensional case is fairly straightforward to discretize and appears as follows:

$$\frac{U_i^{t+1} - U_i^t}{h_t} = D_u\frac{U_{i+1}^t + U_{i-1}^t - 2U_i^t}{h_x^2} - (U_i^t)(V_i^t)^2 + A(1-U_i^t), \tag{2.3}$$

$$\frac{V_i^{t+1} - V_i^t}{h_t} = D_v \frac{V_{i+1}^t + V_{i-1}^t - 2V_i^t}{h_x^2} + (U_i^t)(V_i^t)^2 - (A+B)V_i^t). \tag{2.4}$$

To find the future time step the equation can be arranged in the following Euler's method form

$$U_i^{t+1} = U_i^t + h_t \left(D_u \frac{U_{i+1}^t + U_{i-1}^t - 2U_i^t}{h_x^2} - (U_i^t)(V_i^t)^2 + A(1 - U_i^t) \right), \tag{2.5}$$

$$V_i^{t+1} = V_i^t + h_t \left(D_v \frac{V_{i+1}^t + V_{i-1}^t - 2V_i^t}{h_x^2} + (U_i^t)(V_i^t)^2 - (A+B)V_i^t) \right). \tag{2.6}$$

In the above, h_t is equal to the time step size, with a lower value providing a more accurate estimation of the next step. h_x is the mesh step size. The temporal evolution of the system can be determined in this way. However, Euler's method has both large local and global error accumulation [38].

2.2.1 The Runge-Kutta method

The Runge-Kutta method is a standard method and numerical tool used by mathematicians and physicists, originally developed by German mathematicians Carl Runge and Wilhelm Kutta. In the forth order rendition of the method the next value is determined by the present value at a given time plus the weighted average of four increments, where each increment is the product of the size of the interval and an estimated step change value specified by the function representing the system [38].

$$\boxed{y_{n+1} = y_n + \frac{1}{6}(k_1 + 2k_2 + 2k_3 + k_4)}. \tag{2.7}$$

$$k_1 = hf(t_n, y_n), \tag{2.8}$$

$$k_2 = hf\left(t_n + \frac{h}{2}, y_n + \frac{k_1}{2}\right), \tag{2.9}$$

$$k_3 = hf\left(t_n + \frac{h}{2}, y_n + \frac{k_2}{2}\right), \tag{2.10}$$

$$k_4 = hf\left(t_n + h, y_n + k_3\right). \tag{2.11}$$

We can see in Figures 2.1 and 2.2 the drastic difference in error between the Euler and Runge-Kutta methods, with the Runge-Kutta method having several orders of magnitude less error than Euler's method [38].

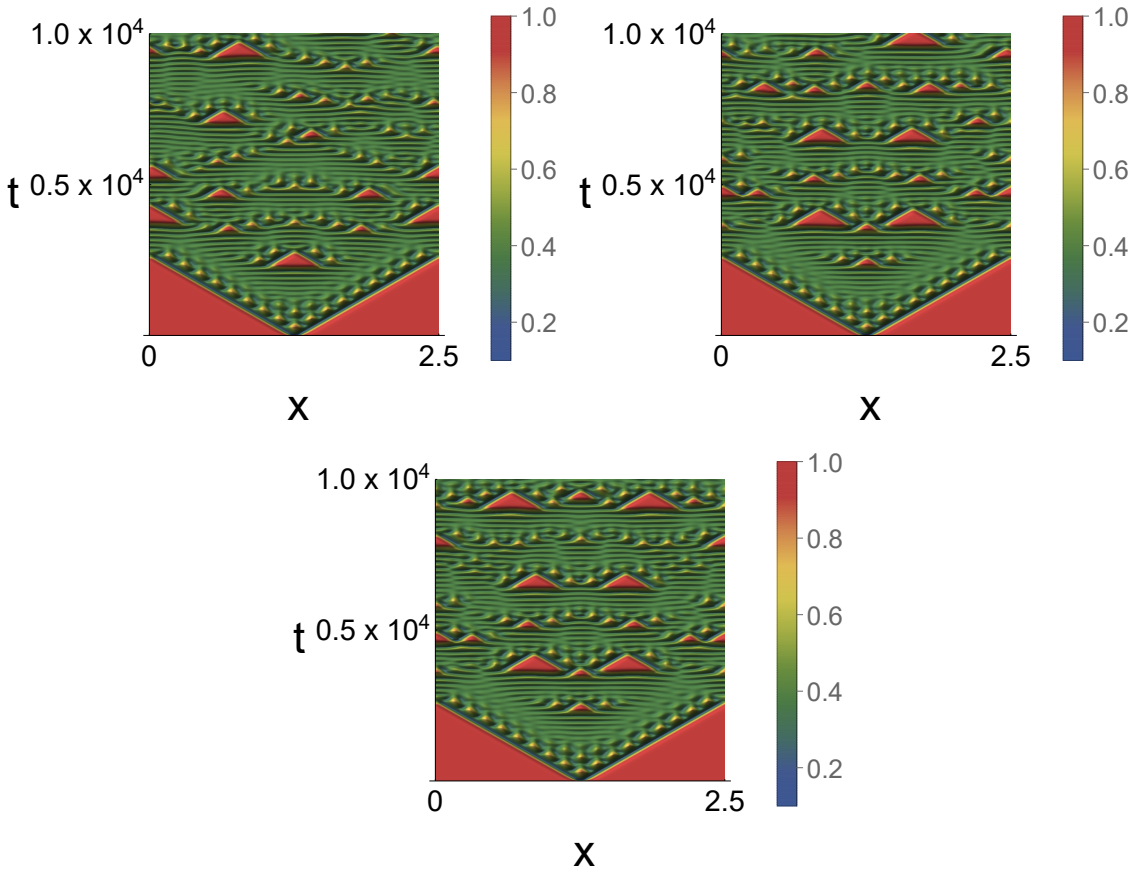

Figure 2.1: Space-time plot for the Gray-Scott model for $D_u/D_v = 2$, with $D_u = 2 \times 10^{-5}$, $A = 0.0234$, and $B = 0.05$. Upper left panel: Euler's method with $h_t = 0.05$, upper right panel: Euler's method with $h_t = 0.00005$. Bottom panel: Runge-Kutta method with $h_t = 0.05$. Due to the symmetric perturbation at $t = 0$, the space-time plot should be symmetric with respect to the middle of the system.

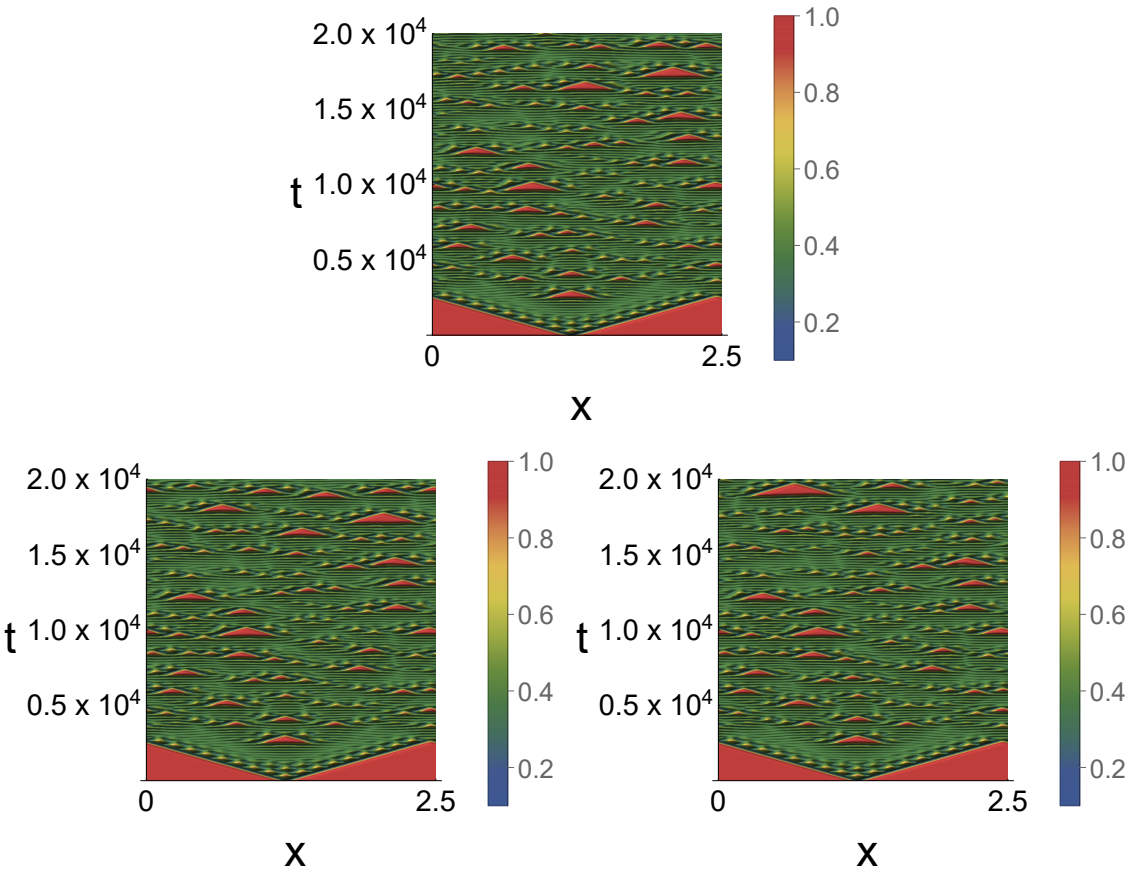

Figure 2.2: Space-time plot with asymmetric initial state for the Gray-Scott model for $D_u/D_v = 2$, with $D_u = 2 \times 10^{-5}$, $A = 0.0234$, and $B = 0.05$. The Runge-Kutta method is used for all these plots. Top: $h_t = 0.05$, bottom left: $h_t = 0.025$ bottom right: $h_t = 0.0125$. Using an asymmetric initial perturbation, the distinction between the different time steps in Runge-Kutta methods can be seen, and need for a careful discussion of the discretization of the diffusion term, see the next section, is apparent.

2.2.2 Discretization of the diffusion term

The process of diffusion is the way that substances move from one part of a system to another, often as a result of molecular motion [39]. When applying numerical integration techniques, the way the term is treated affects the dynamics of the system. The lower the number of sampling points the more inconsistent the motion will be. With an insufficient number of points the approximation of the diffusing behavior will be overestimated at the local steps. The goal is to work with a diffusion order that is computationally feasible and that doesn't overestimate the local calculation and maintains the integrity at the boundaries. Additionally the number of sampling points needs to be low enough so that values at and near the toroidal bounds will not over propagate asymmetries, due to low number difference errors [40]. The number of local points used for the discretization of the diffusion term gives the order of the term. Higher order finite difference terms are obtained through Taylor expansions. It should be noted that the technique outlined in this section is adapted only for a central sampling of points. We can Taylor expand about the points with a step size h as shown in table 2.1.

Table 2.1: Taylor series expansions

Point	
1	$f(x+h) = f(x) + hf'(x) + \frac{h^2}{2}f''(x) + \frac{h^3}{6}f'''(x) + \frac{h^4}{24}f^{iv}(x)$
-1	$f(x-h) = f(x) - hf'(x) + \frac{h^2}{2}f''(x) - \frac{h^3}{6}f'''(x) + \frac{h^4}{24}f^{iv}(x)$
2	$f(x+2h) = f(x) + 2hf'(x) + \frac{(2h)^2}{2}f''(x) + \frac{(2h)^3}{6}f'''(x) + 2^4\frac{h^4}{24}f^{iv}(x)$
-2	$f(x-2h) = f(x) - 2hf'(x) + \frac{(2h)^2}{2}f''(x) - \frac{(2h)^3}{6}f'''(x) + 2^4\frac{h^4}{24}f^{iv}(x)$

The three-point centered-difference formula [40] can be given as

$$f(x+h) + f(x-h) - 2f(x) = h^2 f''(x) + \frac{h^4}{12}f^{iv}(x). \tag{2.12}$$

We can rearrange to find the three-point centered-difference for the second derivative term

$$f''(x) = \frac{f(x+h) + f(x-h) - 2f(x)}{h^2} - \frac{h^2}{12}f^{iv}(x). \tag{2.13}$$

We see through equation 2.13 that the error term is $\frac{h^2}{12}f^{iv}(x)$ which is second order in h, therefore making this a second order correction. If we want the approximation to have less error we need to use more points. This will allow us to cancel terms to a higher order in h.

We can express the second derivative using a five-point centered-difference stencil as

$$f''(x) \approx c_2 f(x+2h) + c_1 f(x+h) + c_0 f(x) + c_{-1} f(x-h) + c_{-2} f(x-2h). \tag{2.14}$$

Using the Taylor expansion in equation 2.14 we can now write our five-point second derivative term in the form of the following matrix

$$\begin{pmatrix} 1 & 1 & 1 & 1 & 1 \\ 2 & 1 & 0 & -1 & -2 \\ \frac{4}{2} & \frac{1}{2} & 0 & \frac{1}{2} & \frac{4}{2} \\ \frac{8}{6} & \frac{1}{6} & 0 & -\frac{1}{6} & -\frac{8}{6} \\ \frac{16}{24} & \frac{1}{24} & 0 & \frac{1}{24} & \frac{16}{24} \end{pmatrix} \begin{pmatrix} c_2 \\ c_1 \\ c_0 \\ c_{-1} \\ c_{-2} \end{pmatrix} = \frac{1}{h^2} \begin{pmatrix} 0 \\ 0 \\ 1 \\ 0 \\ 0 \end{pmatrix}. \tag{2.15}$$

We can then solve the matrix equation 2.15 to find the coefficients. The larger the amount of stencil points the more terms cancel, giving us the error terms to a higher order in h. This method can be extended to any order correction. Below in the table 2.2 up to eighth order is shown for a central finite difference scheme. The step size used is h, and the orders are expanded about an arbitrary point x. The effects of accumulated errors due to approximation methods on smaller vs larger lattice sizes show that for smaller sized lattices the differences are more pronounced. The calculation differences between diffusion approximation orders are still apparent for larger lattice sizes. To ensure that results are consistent and without computational artifacts, results were systematically checked using different diffusion orders and models. For the vast majority of trajectory results the order of the diffusion will not have any noticeable effect, but in the chaotic regimes the small differences accumulate significantly, altering the resulting patterns.

Key features to notice within Fig. 2.3 are the differences in slope of the propagation edge of the growing pattern, and the center pattern at early times. For the results of 2nd and 4th order the early patterns and edge propagation speeds are noticeably different. The simulations for 6th and 8th order show the same propagation speed and early configurations center pattern. These results show a noticeable inconsistency between the two lower order models, which gives doubt to the accurate portrayal of observed chaotic patterns. One likely explanation is that the lower order models give a much higher step overemphasis between two neighboring points. The higher the order corrections the more there will be an overreach of sampling points at the boundaries. The larger number of sampling points at the boundaries tend to propagate the asymmetries associated with the periodic boundary conditions at a faster rate. Due to concerns dealing with boundary error propagation and computational complexity, the 8th order correction is the highest used for results presented in this dissertation. To mitigate any errors associated with the models used, the aforementioned systematic checks were used for the main results.

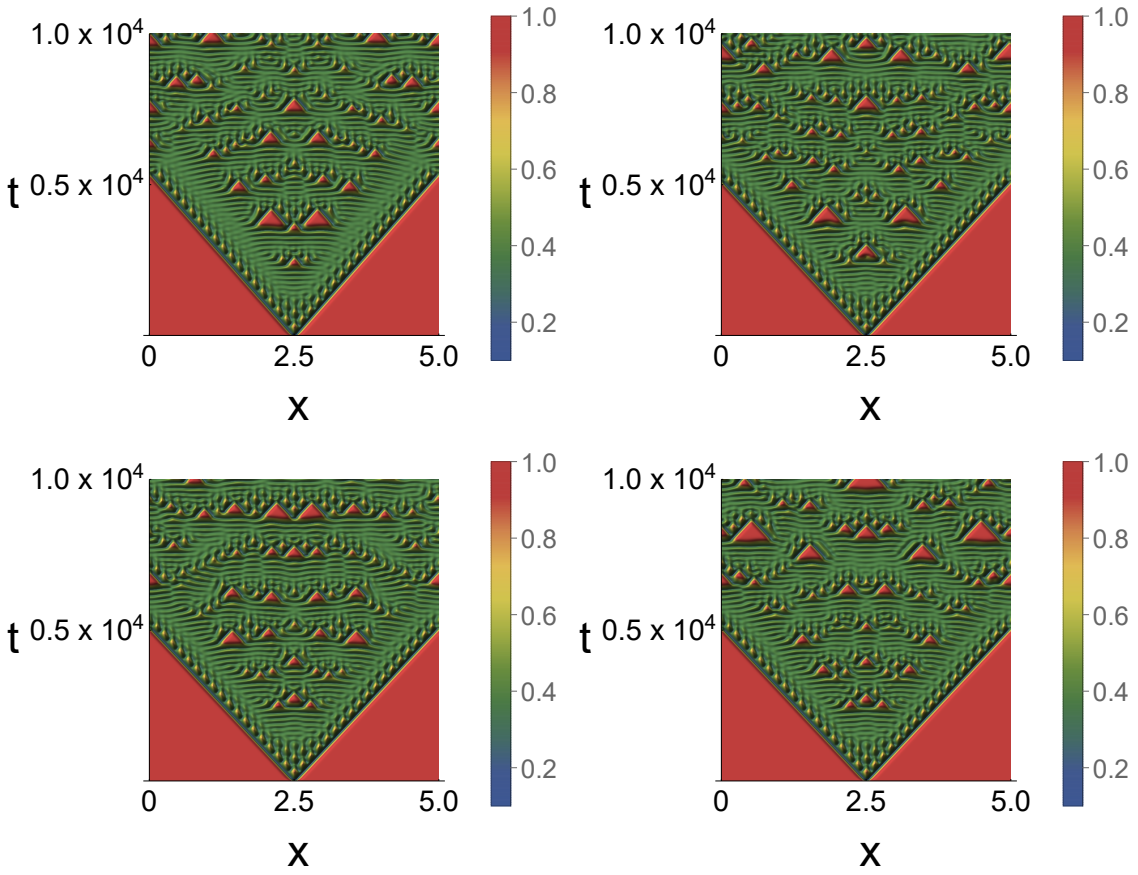

Figure 2.3: Results for the fourth order Runge-Kutta method with different diffusion correction orders and a lattice of 512 mesh points. Top left: 2nd order correction, top right: 4th order, bottom left: 6th order, bottom right: 8th order. The pattern changes between different orders of the discretization of the diffusion term. For the 6th and 8th order cases, the patterns are identical at earlier times, but there are still differences at later times.

Table 2.2: Diffusion higher order correction terms

Order	
2	$\frac{f(x-h)-2f(x)+f(x+h)}{h^2}$
4	$\frac{-f(x-2h)+16f(x-h)-30f(x)+16f(x+h)-f(x+h)}{12h^2}$
6	$\frac{2f(x-3h)-27f(x-2h)+270f(x-1h)-490f(x)+270f(x+1h)-27f(x+2h)+2f(x+3h)}{180h^2}$
8	$\frac{-9f(x-4h)+128f(x-3h)-1008f(x-2h)+8064f(x-1h)-14350f(x)+8064f(x+1h)-1008f(x+2h)+128f(x+3h)-9f(x+4h)}{5040h^2}$

2.3 Gray-Scott Model Parameter Space

The necessity to investigate the model parameter spaces will be outlined in this section. The scaling between the diffusion rates and reaction dynamics plays a significant role in the model dynamics. Specifically, variation in the length scale of diffusion noticeably impacts the features of the resulting parameter spaces. The results will be presented for a high diffusion and a low diffusion scenario. First, the effects of the adjustable parameters for a high diffusion scenario will be surveyed. The high diffusion results will focus on a regime where the model exhibits branching behavior. The remaining analysis will focus on the very low diffusion length scale, on the order of 10^{-5}. This length scale has been more thoroughly studied by other authors and exhibits a large observable chaotic regime. [12, 27, 41, 42].

2.3.1 Branching in a high diffusion case

The effects of the activator feed and inhibitor outflow can be understood by analyzing the system within a robust branching regime for $D_u/D_v = 100$, with $D_u = 1$, $h_x = 0.2$ and $h_t = 0.01$. Using the baseline parameter values from Parekh, Kumar, and Kulkarni [43] ($A = 0.03$ and $B = 0.059$), we can survey the effect of the two parameters by making changes in the values of A and B around this point. The system was subjected to initial conditions with an inhomogeneous initial state with $(u, v) = (0.5, 0.25)$ in a small central region and $(u, v) = (1, 0)$ otherwise. Based on our numerical investigations we find that the increase of the substrate inflow rate promotes pulse splitting. Increasing the conversion rate of the activator to an inert product causes the branching behavior to be suppressed. The results outlined in Figures 2.4, 2.5 and 2.6 show the importance of cataloging the effects of the system's adjustable parameters. For the two sets of A values shown in Figures 2.5 and 2.6, it is visible that the effect of B on the pulse splitting behavior is to delay the onset of branching behavior. The way that the overall branching behavior changes across different A and B values for the high diffusion parameter space hints at the existence of more types of patterns.

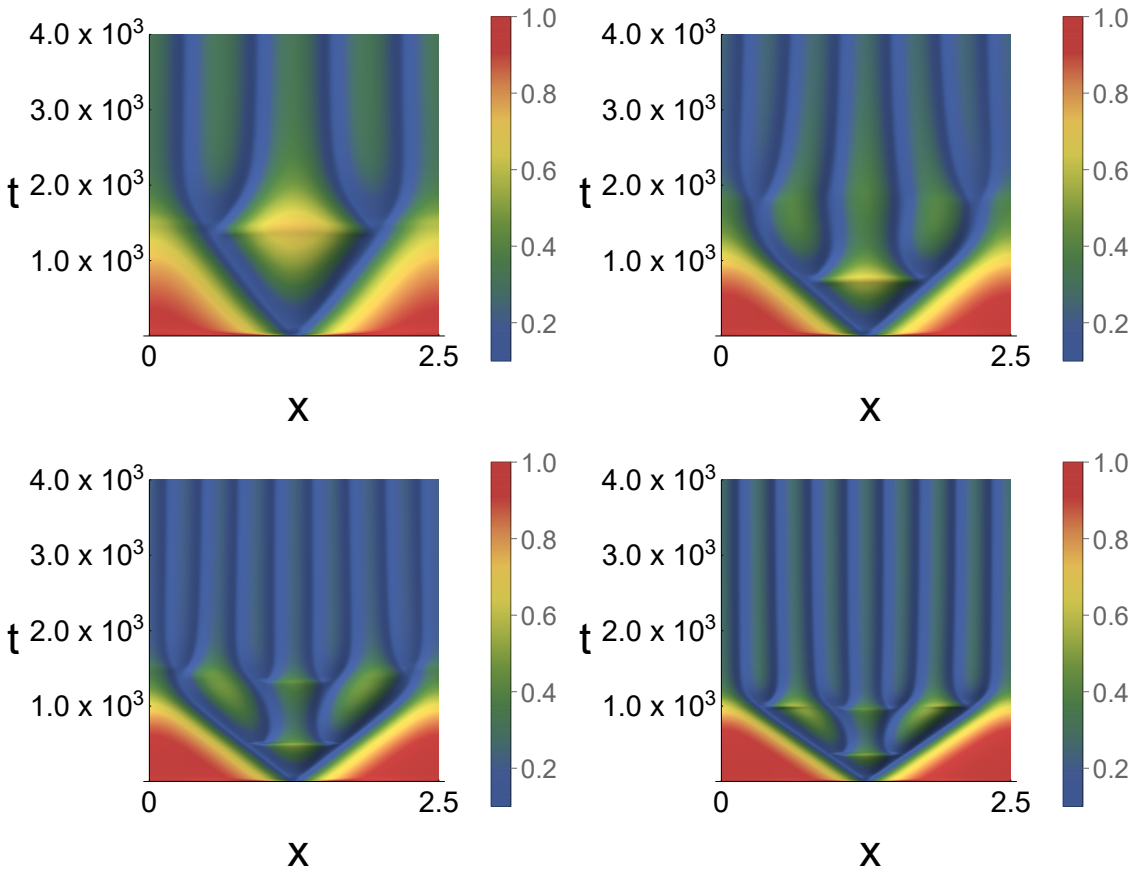

Figure 2.4: Systems with $B = 0.059$ and different values of A. The number of branches increases for increasing A. Top left: $A = 0.02$, top right: $A = 0.03$, bottom left: $A = 0.04$, bottom right: $A = 0.06$.

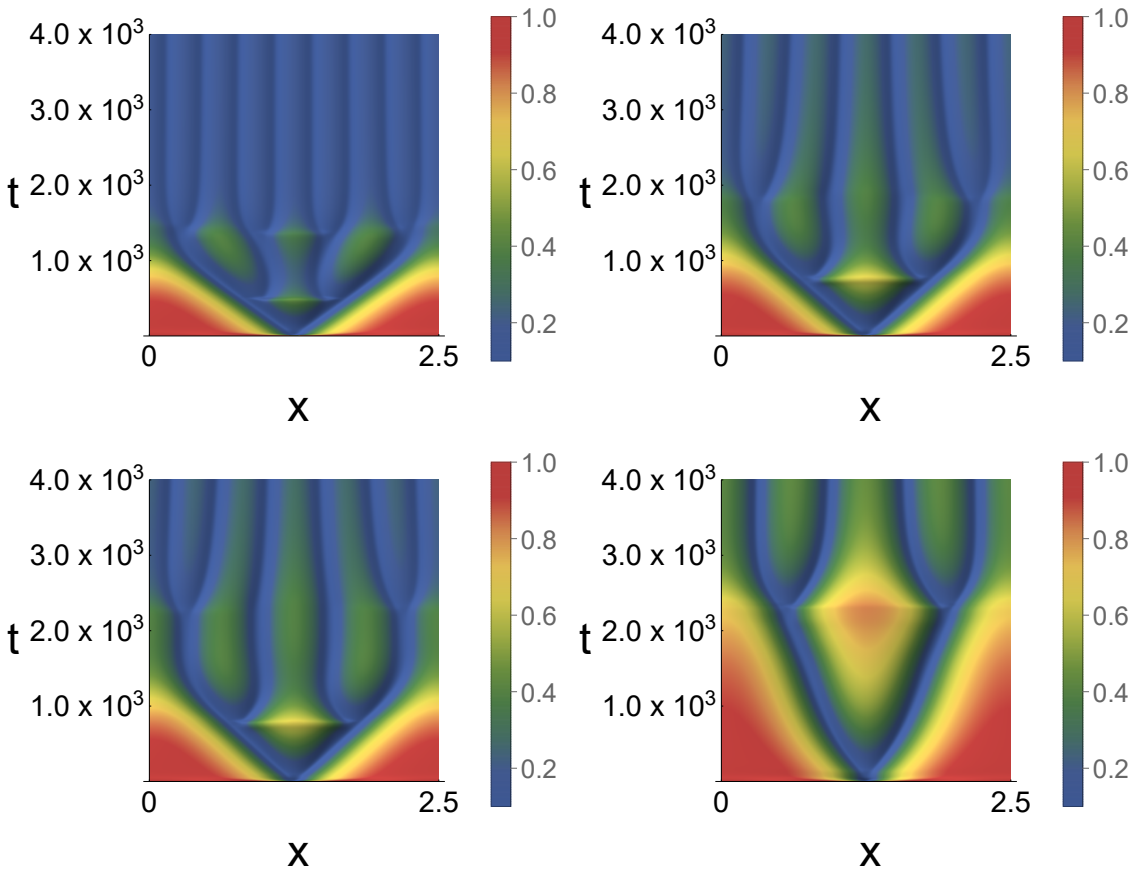

Figure 2.5: Systems with $A = 0.03$ and different values of B. The number of branches decreases for increasing B. Top left: $B = 0.05$, top right: $B = 0.059$, bottom left: $B = 0.06$, bottom right: $B = 0.08$. The number of branches decreases for higher values of B.

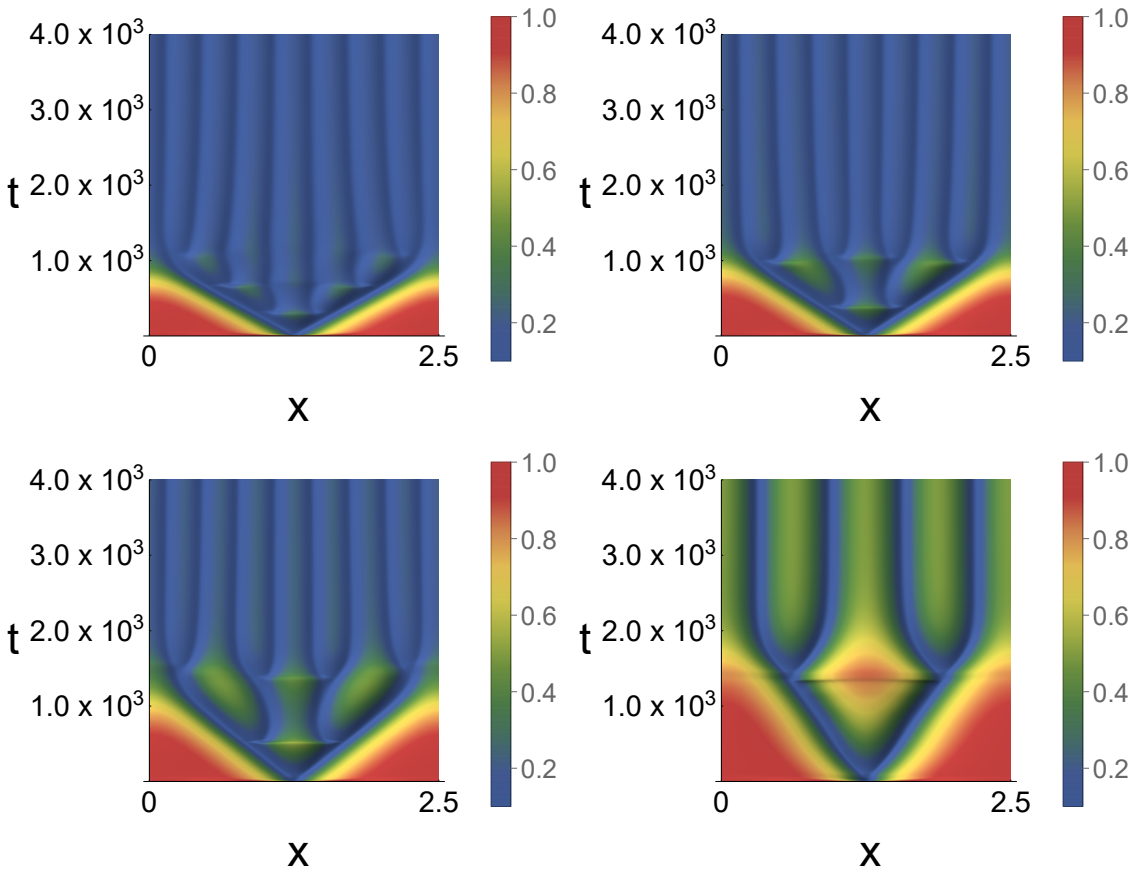

Figure 2.6: Systems with $A = 0.04$ and different values of B. The number of branches decreases for increasing B. Top left: $B = 0.05$, top right: $B = 0.059$, bottom left: $B = 0.06$, bottom right: $B = 0.08$. With a higher A value the effect of increasing B is diminished.

2.3.2 Parameter space survey for the low diffusion case

One of the first things to investigate for a chaos producing model is the parameter space. The system is surveyed using numerical results combined with theoretical curves obtained through linear analysis and bifurcation theory. There are two main adjustable parameters for the Gray-Scott model, the feed rate A and the activator conversion rate B. The total sum of the substrate feed rate and the activator conversion rate is the activator removal rate, $A + B$. The Gray-Scott model is of the activation-substrate depletion type. Therefore, the two concentrations u and v tend to vary opposite to one another.

The Gray-Scott model is well studied and has well known and defined chaotic regimes for particular diffusion value ranges and ratios that can be used as a baseline. A method to control the chaotic behavior requires a high level of precision in the computational results. The requirement of high precision results necessitates using the techniques discussed in Section 2.2. In this way, we build a thorough parameter space around the chaotic regime to ensure that the most subtle effect of perturbation routines can be detected.

In our work the system was first surveyed using an Euler integration scheme for $D_u/D_v = 2$, with $D_u = 2 \times 10^{-5}$ and $D_v = 10^{-5}$ with $h_x = \frac{2.5}{256}$ as previously investigated by Kyrychko et al. [12]. The spatial discretization was chosen to be consistent with previous works [12, 27, 41, 42]. The ratios between the reaction terms and the diffusion terms in the Gray-Scott model have a direct impact on which patterns are formed. The time scale for iterative steps needs to be below a certain threshold or the diffusion term will be grossly overestimated, giving unstable solutions. This condition for stability for the forward Euler's method [44, 45] is

$$h_t < \frac{h_x^2}{2D_v}. \tag{2.16}$$

The time step used, $h_t = 0.05$, yields a stable solution for both the Euler's and Runge-Kutta forth order methods. The stability index use by Mazin et al. [27] is equivalent to our equation 2.16.

In our study the system was numerically integrated using a Runge-Kutta fourth order method with an eighth order diffusion term on 256, 512 and 1024 sized lattices to ensure consistency of results. The system was subjected to initial conditions with an inhomogeneous initial state with $(u, v) = (0.5, 0.25)$ in a small central region and $(u, v) = (1, 0)$ otherwise. The central width was varied to ensure the observed regimes were not an artifact of the initial perturbation. For the results presented here a width of 0.625 is used. Other initial conditions were also surveyed to ensure that the parameter space found was consistent across different initial conditions. The initial conditions investigated included off symmetric inhomogeneous initial state regions, along with random initial configurations. The effects of the values of$A$ were investigated using values ranging from 0 to 0.05, in dividing units of 0.0002. Likewise the values of B where systematically investigated in a range from 0.035 to 0.055. The results were observed and placed into different behavior types using observed differences and existing literature in the field [12, 41, 42]. The parameter space regime zone edges were tabulated

for both the lower and upper threshold of each regime. The general behavior of the different parameter space regimes was consistent across lattice sizes greater than 256.

The Gray-Scott model exhibits a rich parameter space of various patterns. Surveying the Gray-Scott parameter space allows a proper distinction between different observed patterns and establishment of regime boundaries. This gives a benchmark to guide pattern creation by establishing what types of behavior belongs to different regimes. The application of perturbations will be used to mimic elements of behavior of one regime in a selected localized region to target a pattern formation type. The following overview of the four main groups of patterns surrounding transient chaos is done in preparation of that study.

2.3.3 Parameter space overview

The Gray-Scott model parameter space for low diffusion shown in Fig. 2.7 is focused on highlighting transient chaos and the surroundings regimes. Following the results of linear stability analysis conduced by Mazin et al. and Kyrychko et al. [12, 27] the lower limit of the Hopf bifurcation curve is given by

$$\mathrm{A}_{\mathrm{Hopf}} = \frac{1}{2}\left(\sqrt{B} - 2B - \sqrt{B(1-4\sqrt{B})}\right). \tag{2.17}$$

We can see within Fig. 2.7 that the boundary of the Hopf bifurcation serves, as expected from the results of Mazin et al. [27] as the upper limit of the chaotic regime. One main distinction to note of the parameter space obtained through our numerical simulations is that the boundary of chaotic behavior moves further from the Hopf bifurcation line for larger values of the system parameters A and B. This shows that the interplay between the reaction terms and diffusion rates shifts the behavior of the system for larger reaction parameters away from linearized predictions. Each of the regimes presented in Fig. 2.7 will be explained below.

2.3.4 Regime 1

As shown in the four panels of Fig. 2.8 the the system in this regime either undergoes a complete conversion to substrate, u, or forms a propagating pulse of substrate-activator propagation. The initial perturbation region slowly decays to a constant value. This value is dependent upon the concentrations of the activator inflow rate. For lower values of activator conversion rate, B, the larger values of substrate feed rate give a faster rate of propagation toward the edges. This is shown in Fig. 2.8 in the top two panels. As the substrate feed strength increases, the propagation speed of the lines increases, giving a scenario where the lines interact and reflect at the boundaries. When the activator conversion rate is sufficiently high, the effective spread of diffusion is suppressed, causing the traveling lines to propagate forward in parallel straight lines as shown in the bottom two panels of the space-time plots

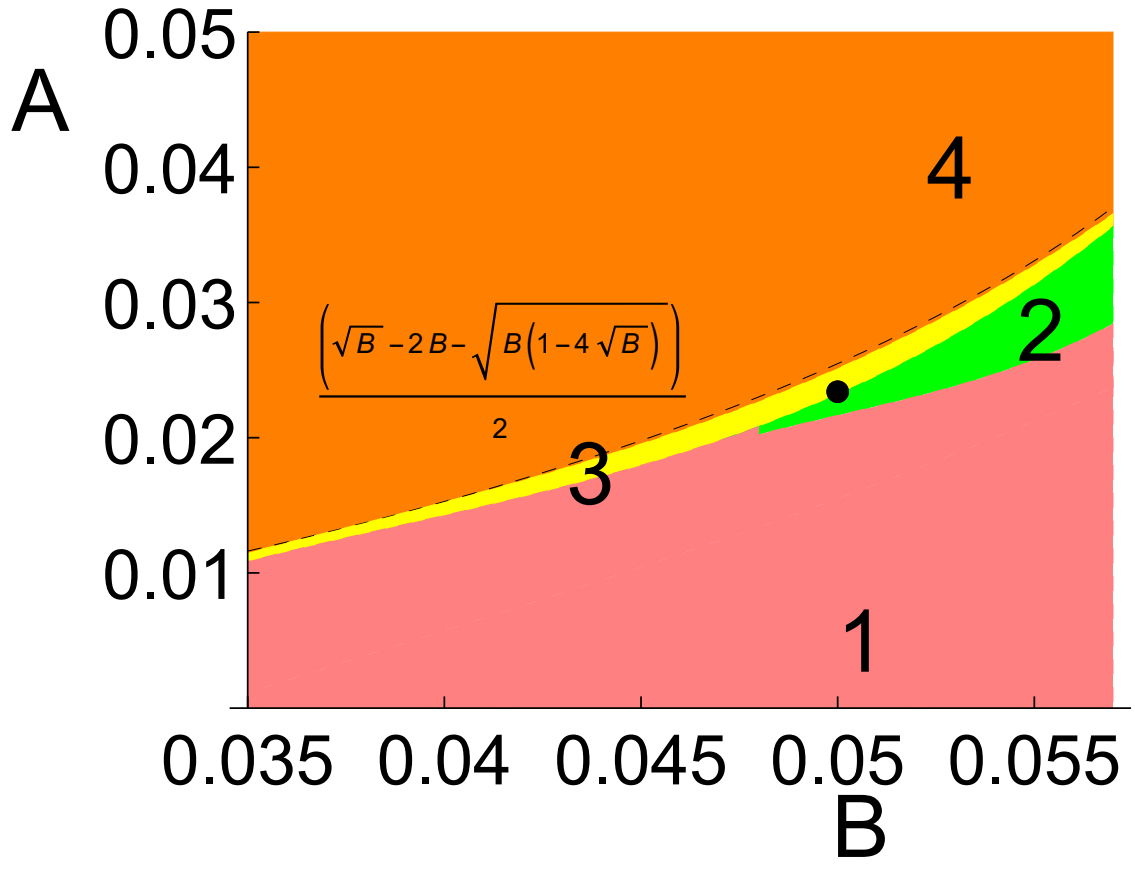

Figure 2.7: The different dynamic regimes encountered for $D_u/D_v = 2$, with $D_u = 2 \times 10^{-5}$ and $D_v = 10^{-5}$, and an inhomogeneous initial state with $(u, v) = (0.5, 0.25)$ in a small central region and $(u, v) = (1, 0)$ otherwise. The width of the system is $L = 10$, and 1024 grid points are used for the spatial discretization. The point (0.05, 0.0234), highlighted in the figure, is used for the majority of the main results in chapter 3. The dashed line is the lower range of the Hopf bifurcation, as given in equation 2.17.

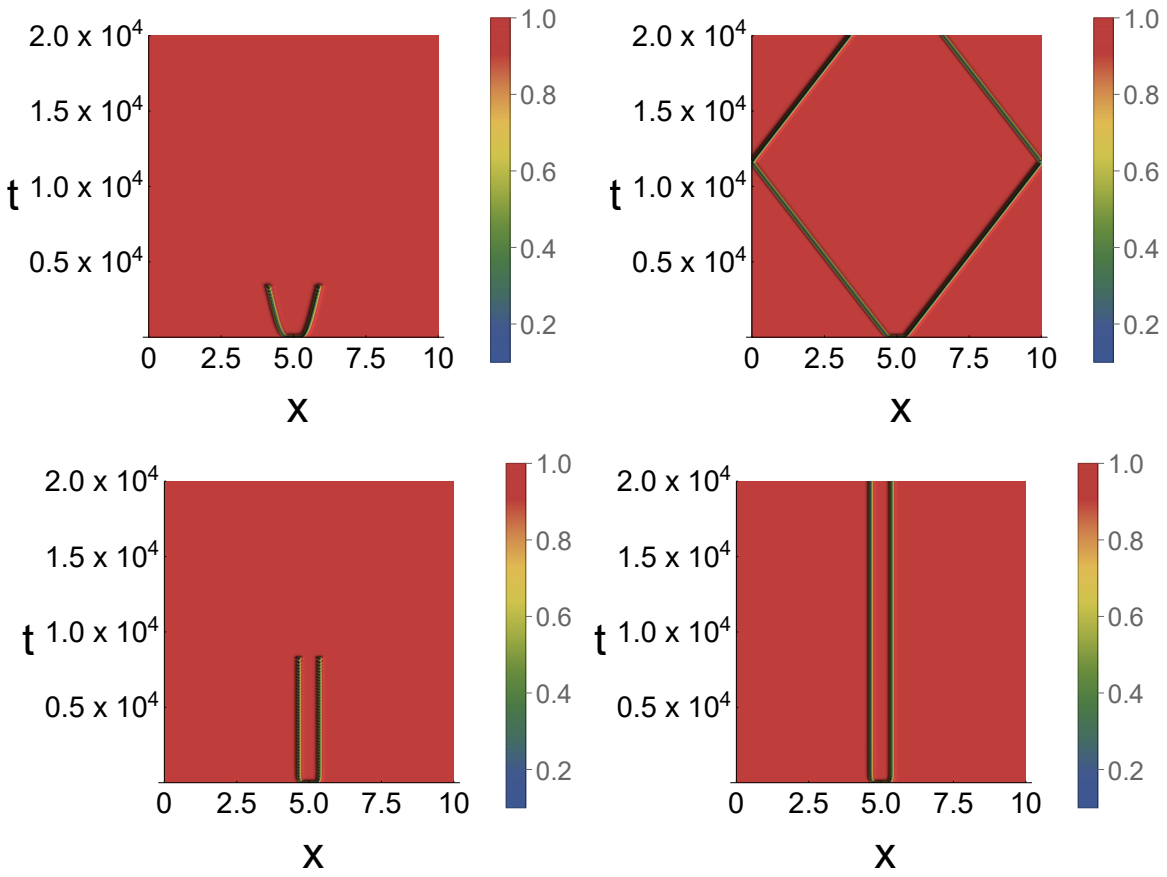

Figure 2.8: Space-time plot for the Gray-Scott model for $D_u/D_v = 2$, with $D_u = 2 \times 10^{-5}$, and $h_t = 0.05$. Top left: A $= 0.015$, $B = 0.05$, top right: A=0.017, B=0.05, bottom left: $A = 0.0222$, $B = 0.056$ bottom right: $A = 0.02282$, $B = 0.056$.

in Fig. 2.8. The general behavior of this regime is that the system fills with substrate, u, to a trivial steady steady state of $(u, v) = (1, 0)$, and is often associated with a saddle-node bifurcation [27].

2.3.5 Regime 2

In the regime designated by a 2 in Fig. 2.7, the system forms a series of traveling pulses. These traveling pulses evolve temporally to fill the entire lattice. As the substrate feed rate rises for a given activator conversion rate, these lines interact to form dense structures as shown in the behavior change between the top right and bottom left panels in Fig. 2.9. The regime boarders regime 1 and starts for higher substrate values above a threshold value of activator conversion rate. This transition is an indication of this regime consisting of Turing patterns [46]. When the activator conversion rate becomes high enough, the increase

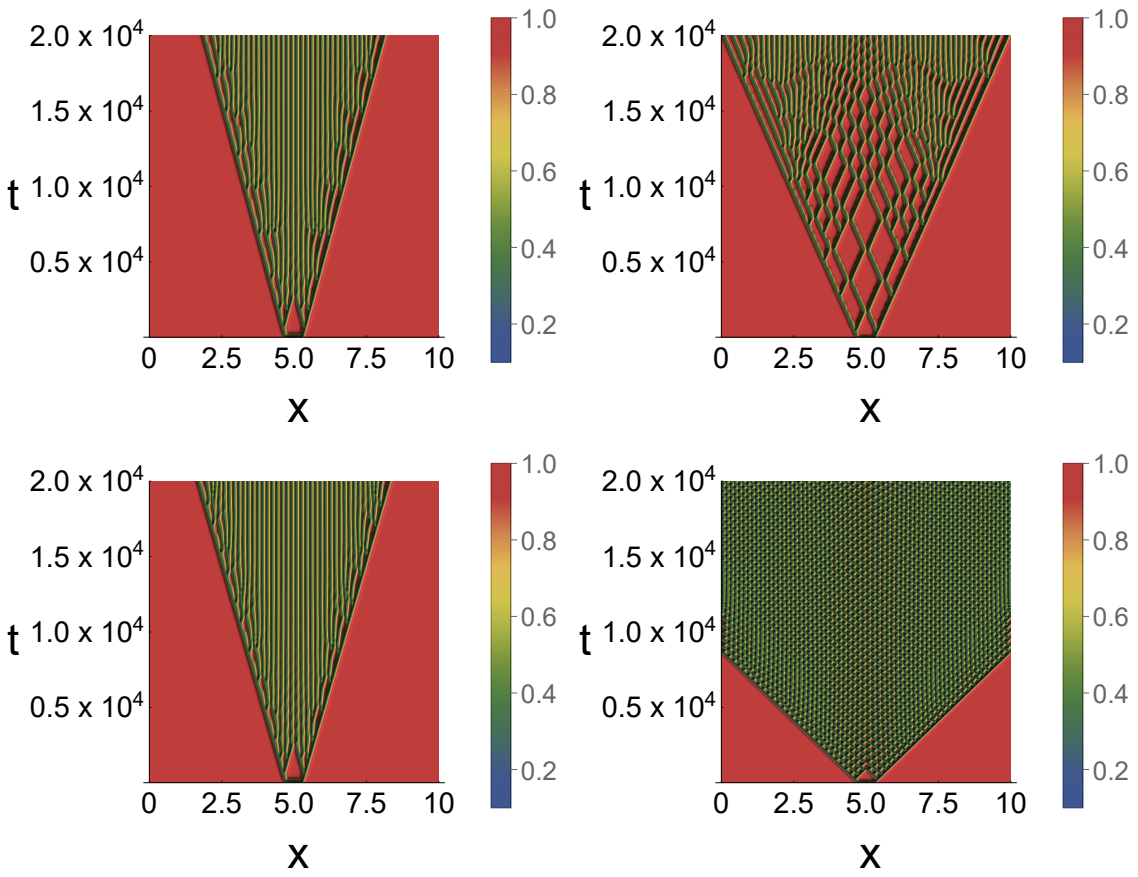

Figure 2.9: Space-time plot for the Gray-Scott model for $D_u/D_v = 2$, with $D_u = 2 \times 10^{-5}$, and $h_t = 0.05$. Top left: $A = 0.0268$, $B = 0.056$, top right: $A = 0.0269$, $B = 0.0555$, bottom left: $A = 0.0274$, $B = 0.0555$, bottom right: $A = 0.0234$, $B = 0.051$.

in substrate feed rate causes a situation where regions form with high values of substrate surrounded by high values of activator that cycle back and forth. An example of this is shown in the bottom right panel of Fig. 2.9.

2.3.6 Regime 3

The third regime is a spatio-temporal chaos regime that results from the interaction between a Hopf instability and a Turing instability [27, 41, 42]. This state is a transient chaotic regime. The chaotic behavior has a lifetime related to the square of the lattice size [34]. The general behavior sees the appearance and disappearance of small regions where the densities u and v take on values close to those of the trivial steady state. The chaos regime has a narrow crescent shaped band dictated by the interactions between stability curves [27, 41, 42]. The region defined by the results of numerical studies shows a consistent overlap with the

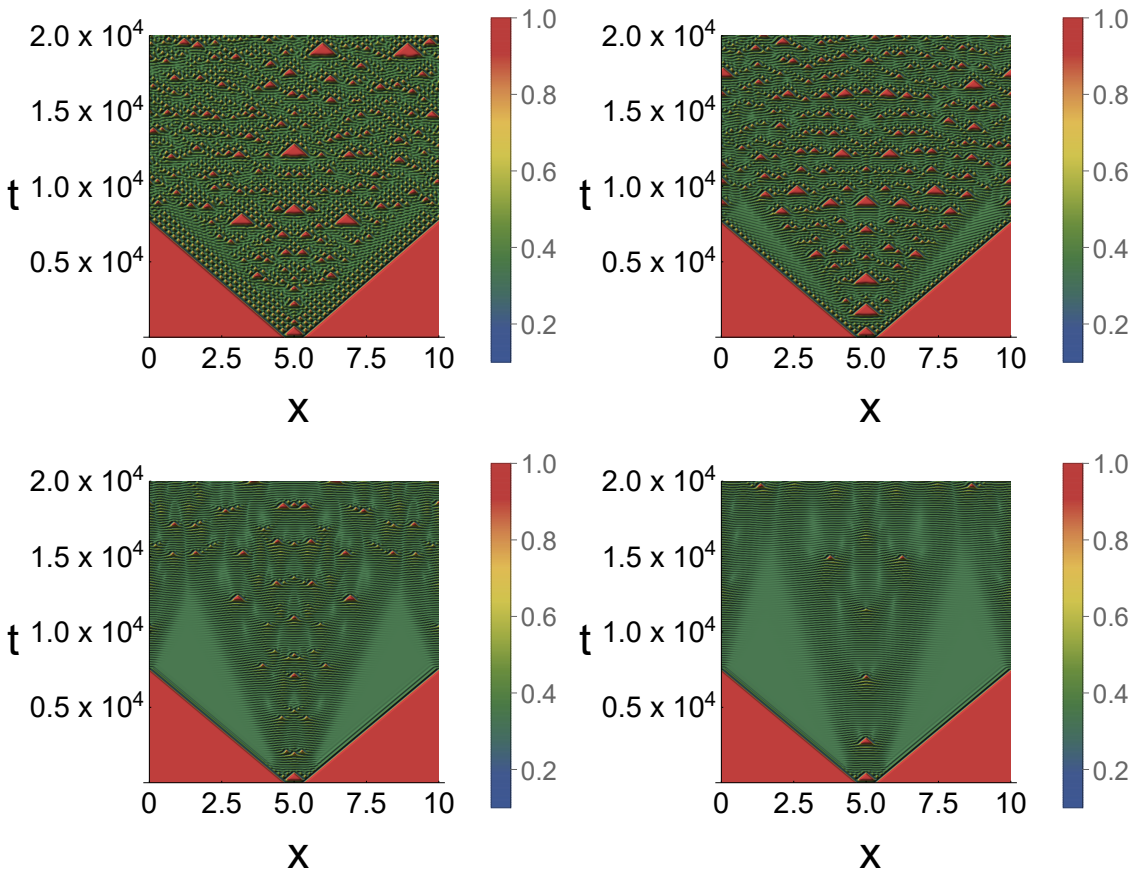

Figure 2.10: Space-time plot for the Gray-Scott model for $D_u/D_v = 2$, with $D_u = 2 \times 10^{-5}$, and $h_t = 0.05$. Top left: $A = 0.0234$, $B = 0.05$, top right: $A = 0.024$, $B = 0.05$. Bottom left: $A = 0.025$, $B = 0.05$, bottom right: $A = 0.0252$, $B = 0.05$.

predicted upper extent of chaos given by the Hopf bifurcation curve shown in Fig. 2.7. The behavior of the chaos depends on the values of the parameters. We can see this from the bottom two panels of Fig. 2.10, with a closer proximity to the steady state regime for the right panel.

2.3.7 Regime 4

The final regime shown in Fig. 2.11 is achieved when the activator flow stream is maintained above a certain value for a given outflow value. The system then reaches a steady state like solution of uniform constant value where both substrate and activator coexist in a nontrivial state. The coexisting condition has a significant effect when using a perturbation technique, perturbing a region of the system to this steady state can induce patterns in other regions. This state can be viewed as a mutual coexistence of co-propagating substrate and activator.

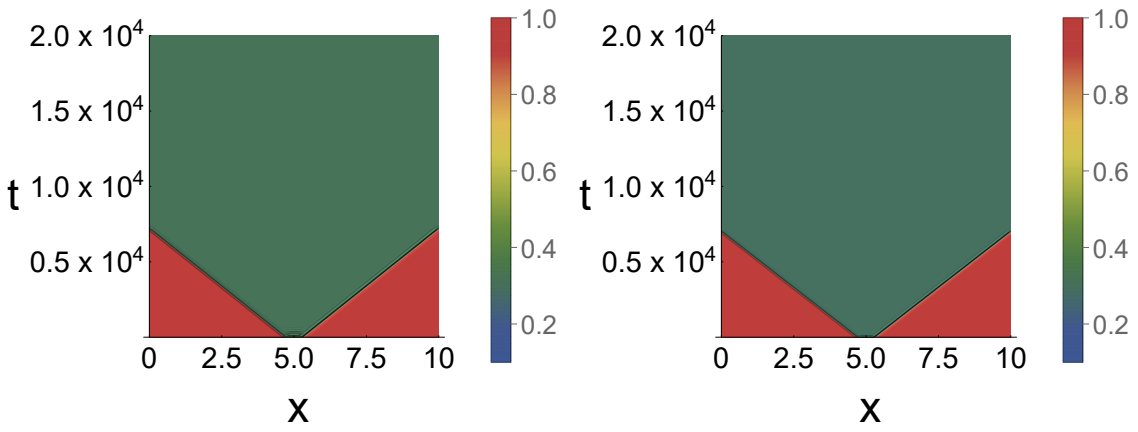

Figure 2.11: Space-time plot for the Gray-Scott model for $D_u/D_v = 2$, with $D_u = 2 \times 10^{-5}$, and $h_t = 0.05$. Left: $A = 0.029$, $B = 0.05$ right: $A = 0.034$, $B = 0.05$.

2.4 Time-delayed feedback scheme

Using the aforementioned Gray-Scott model we can express the reaction part as

$$f(u,v) = -uv^2 + A(1-u),$$

$$g(u,v) = uv^2 - (A+B)v.$$

We can write the differential equations with a control-type perturbation [12] incorporated as:

$$\frac{\partial}{\partial t}\begin{pmatrix} u \\ v \end{pmatrix} = \begin{pmatrix} f(u,v) \\ g(u,v) \end{pmatrix} + \begin{pmatrix} D_u & 0 \\ 0 & D_v \end{pmatrix} \nabla^2 \begin{pmatrix} u \\ v \end{pmatrix} + K \begin{pmatrix} u(t-\tau) - u(t) \\ 0 \end{pmatrix},$$

where we have K as the control strength which can be either positive or negative. The delay time is given as τ. Using the numerical solving techniques from the previous section the system history of the concentration density of $u(x,t)$ can be stored to apply a feedback to the current time iteration. Within the framework of the Runge-Kutta fourth order iteration scheme the control is applied after the sequence is completed.

$$u(t+1) = u(t) + \frac{1}{6}\left(u_1 + 2u_2 + 2u_3 + u_4\right) + K\left(u(t-\tau) - u(t)\right). \tag{2.18}$$

Here we have $\frac{1}{6}\left(u_1 + 2u_2 + 2u_3 + u_4\right)$ as the weighted average of four increments used in the Runge–Kutta method. To avoid confusion the value of u that is used for the perturbation is taken at the past time step, without any Runge–Kutta term influences. Taking the Runge-Kutta method corrected $u(x,t)$ would be using a value estimate as part of the perturbation routine. The effects on the time-delayed feedback perturbation for the Gray-Scott model is shown in Fig. 2.12 with $K > 0$, sending the system into the nontrivial steady state, and $K < 0$, taking the system into the mutual coexistence steady state.

2.4.1 Past time delay feedback scheme

Similar to the time-delayed feedback scheme a perturbation is applied after a certain number of time steps has taken place. For this perturbation the feedback value is fixed based upon a set time in the system's history, representative of a smaller reaction chamber coupled to a larger steady state bath held at a constant condition. Within the field of chemistry similar experimental setups have been used for systems of internally coupled chemical oscillators [47, 48]. The form of the perturbation equation is

$$\frac{\partial}{\partial t}\begin{pmatrix} u \\ v \end{pmatrix} = \begin{pmatrix} f(u,v) \\ g(u,v) \end{pmatrix} + \begin{pmatrix} D_u & 0 \\ 0 & D_v \end{pmatrix} \nabla^2 \begin{pmatrix} u \\ v \end{pmatrix} + K \begin{pmatrix} u(T) - u(t) \\ 0 \end{pmatrix}. \tag{2.19}$$

Like the preceding equation 2.18 we have K as the control strength which can be either positive or negative, whereas T is the time at which the system concentration is stored. For

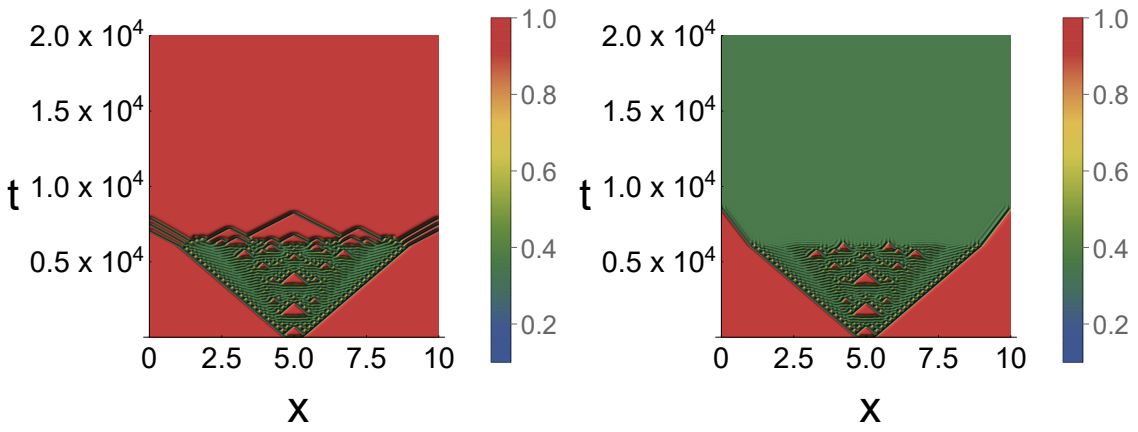

Figure 2.12: Space-time plot for the Gray-Scott model for $D_u/D_v = 2$, with $D_u = 2 \times 10^{-5}$ and $D_v = 10^{-5}$, $A = 0.024$, and $B = 0.05$. The system is perturbed starting at $6,000$, with the delay value $\tau = 0.5$, or ten iteration steps backward. Left: $K = 0.03$, right: $K = -0.03$. For a positive perturbation shown on the left the system enters the trivial state where $u = 1$. When the perturbation strength is negative, as shown on the right, the entire region enters a nontrivial state with $u \neq 0$ and $v \neq 0$, encompassing the behavior of the fourth parameter space regime.

the Gray-Scott model this type of perturbation has a direct effect on branching behavior. The changes for the branching behavior can be either suppressing or enhancing as shown in Figures 2.13 and 2.14 respectively. The effects of this technique on the chaotic regime will be shown in the Chapter 3.

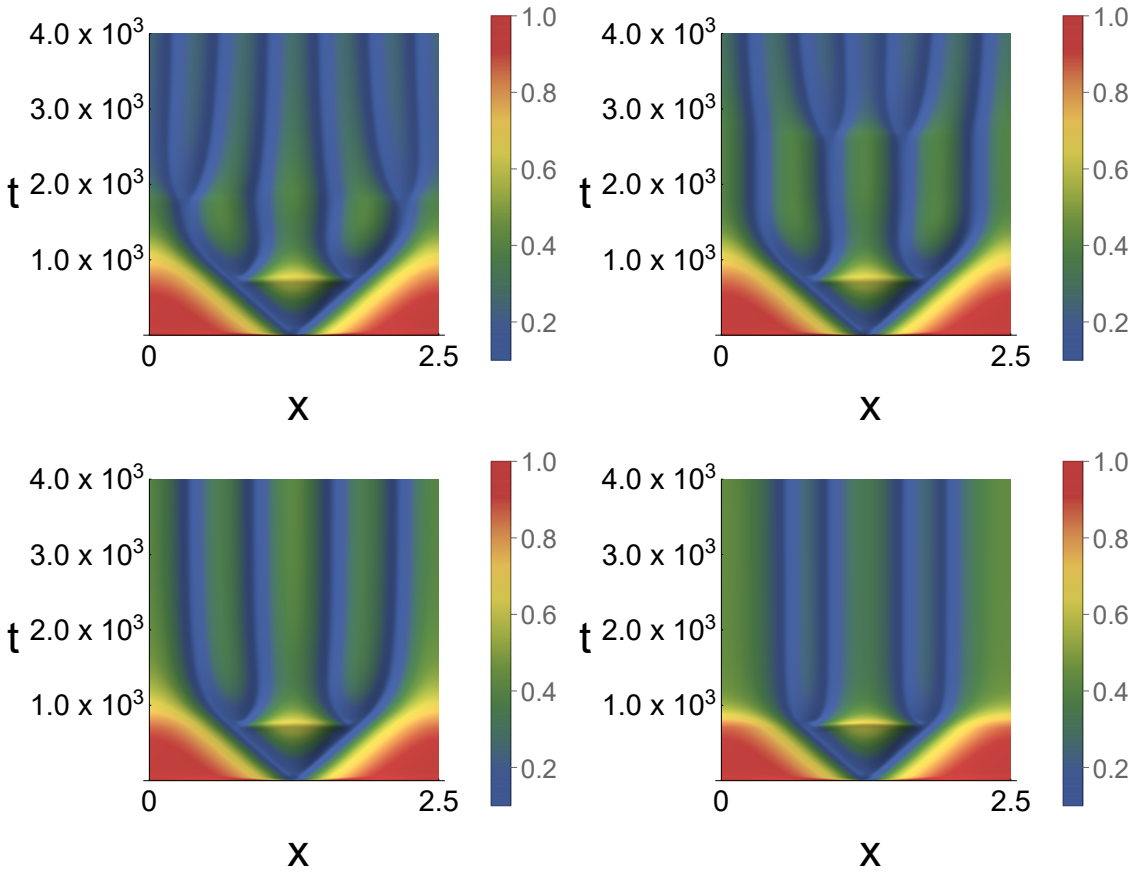

Figure 2.13: Space-time plot for the Gray-Scott model for $D_u/D_v = 100$, with $D_u = 1$, $A = 0.03$, and $B = 0.059$. The system is perturbed starting at $t = 700$. Top left: unperturbed system, top right: $K = -0.0001$, bottom left: $K = -0.0002$, bottom right: $K = -0.0003$. The substrate concentration density at $t = 700$ is used for the perturbation. For negative K, the effect is suppressing the branching behavior in an effect similar to that observed when increasing the activator reaction rate.

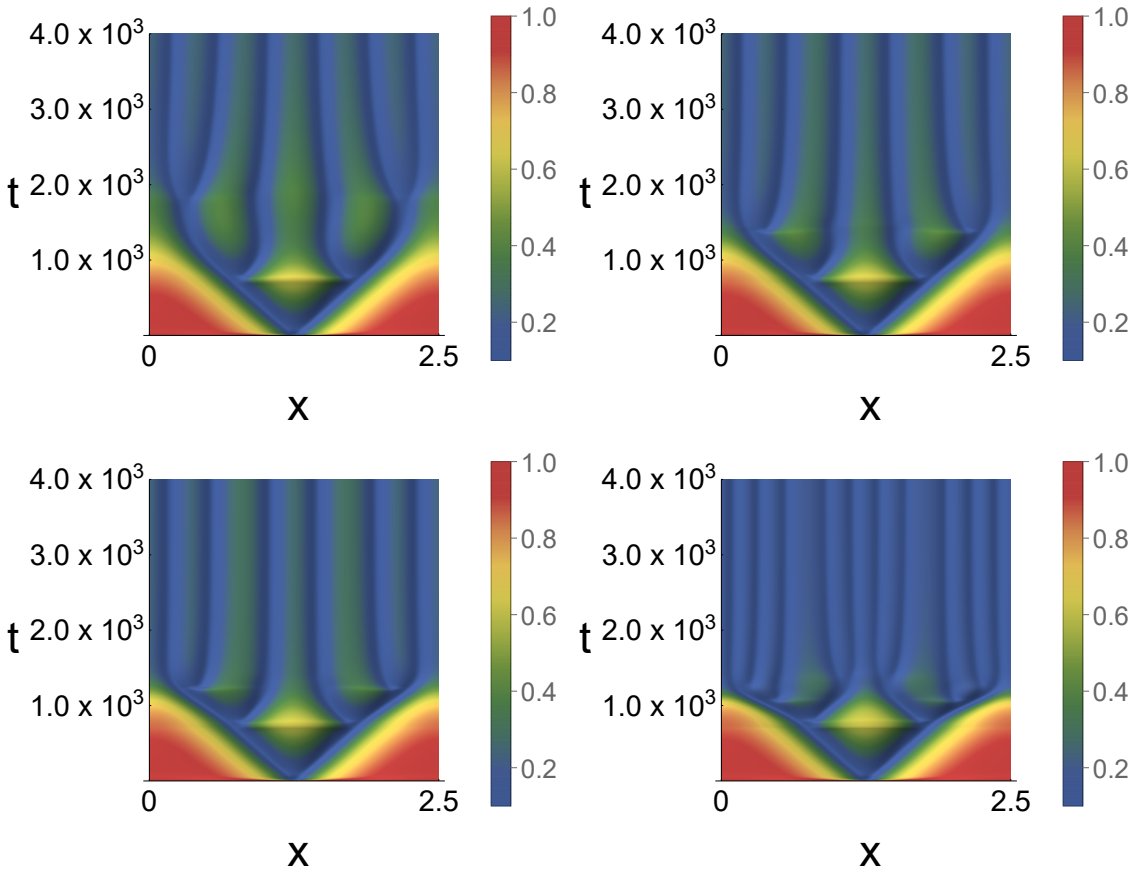

Figure 2.14: Space-time plot for the Gray-Scott model for $D_u/D_v = 100$, with $D_u = 1$, $A = 0.03$, and $B = 0.059$, the system is perturbed starting at $t = 700$. Top left: unperturbed system, top right: $K = 0.0001$, bottom left: $K = 0.0002$, bottom right: $K = 0.0005$. The substrate concentration density at $t = 700$ is used for the perturbation. For positive K, the effect is enhancing the branching behavior.

2.5 Data analysis techniques

To understand and manipulate a system, a method to quantitatively explain and characterize different behaviors is necessary. In this section we will outline some of the tools that are used to characterize the systems and quantify novel pattern behavior.

2.5.1 Fourier analysis

The definition of the Fourier transform is given as

$$f(\nu) = F_t[f(t)](\nu) = \int_{-\infty}^{\infty} f(t)e^{-2\pi i\nu t}dt \tag{2.20}$$

The discrete Fourier transform can be written as

$$F_n = \sum_{m=0}^{N-1} F_m e^{-2\pi im/N} \tag{2.21}$$

where N is the total number of discrete data points in the set. This is used within the framework of a Mathematica code to characterize the periodic patterns formed when applying time-delayed perturbations to the systems. The higher the number of data points the higher the resolution of the obtained Fourier peaks. The spectral resolution spacing is given by

$$\Delta\nu = \frac{1}{n_p(TStep)h_t} \tag{2.22}$$

A smaller interval between data output will be useful here, given that the minimal resolution depends on how small the data output step size is. h_t is the integration step size and n_p is the number of data points in the data set. The value $TStep$ is the number of iteration steps between recorded data values. For the case of the perturbed models, the time after periodic patterns are starting to form is the start time for calculating the Fourier transform. The results can be quickly analyzed indicating periodic behavior to undergo more thorough analysis. These automated methods can be used to quickly tabulate subtle perturbation effects.

2.5.2 Analysis of periodic patterns

Having multiple methods give the same quantitative features ensures and verifies that the results are consistent and their interpretation is logical. When working with a system in a way that is uncharted, often the unexpected occurs, and a good way to be able to progress is to find or create different modeling tools and methods. The first tool employed for dealing with periodic or periodic appearing patterns is the Fourier transform mentioned in section

2.5.1. The method is standard in the field and is a good first point of attack when dealing with structures that may have a degree of periodicity.

When dealing with chaos, messy and unexpected patterns require additional analytic techniques to be developed. One such method is through taking the peak to peak values by using a function that finds extrema as shown in Fig. 2.15 and the corresponding Table 2.3. The first point marked with a red dot in Figure 2.15 is the start for the data tabulation as shown in Table 2.3. The first column down is distance between the first marked point and the following marked points. The same structure follows for the second and onward points within the table. We see that after 9 points the pattern repeats which is the repeat period of the structure. The green points along the diagonal give the consistent impression that the entire structure has the same repeat period.

The Fourier data is shown in Fig. 2.16 for the same data used in Fig. 2.15. The highest Fourier peak is at 1380.6. The lowest frequency observable peak is at 2803, which would be nearest to the peak to peak patterns we are observing. This peak value is different from the value of 2767.5 obtained from analyzing the time series peak to peak separations. The combination of different modes creates the observed repeating periodic patterns. The effects of the subtle changes of the different Fourier peaks is difficult to understand for discrete data without observing the overall period of the pattern. The created patterns have main Fourier peaks that change inconsistently across different parameter values. The main Fourier peak may change abruptly, while the observed overall pattern has a subtle and consistent change across different parameter values. The peak to peak analysis technique gives a consistent benchmark to compare the periodic structures that are formed.

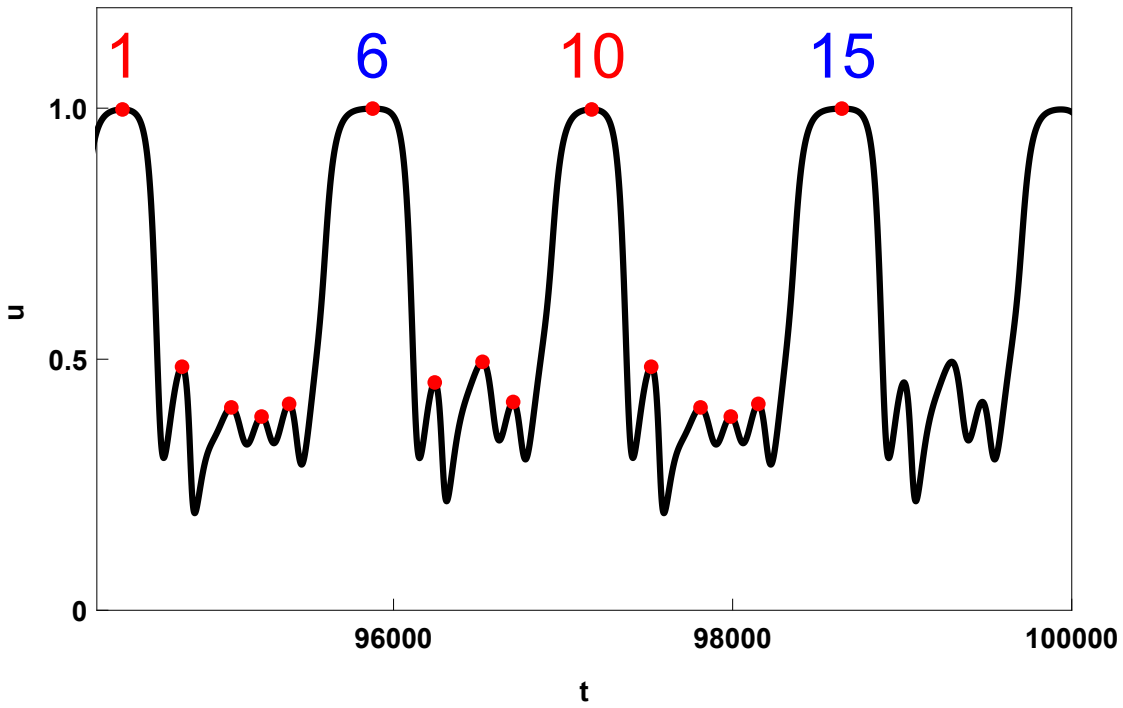

Figure 2.15: Time series plot for the Gray-Scott model for $D_u/D_v = 2$, with $D_u = 2 \times 10^{-5}$, and $h_t = 0.05$. The center point of a perturbation produced periodic pattern. The plot shows the maxima and minima of the time series of concentration u. The numbered plot points 1 and 6, and 10 and 15 form repeating pairs of patterns.

Table 2.3: From the markings in the Fig. 2.15, the first column is the separations from the first peak. We can see that the entries along the diagonal starting at the red point and ending at the blue point are equal to the repeat period.

	1	2	3	4	5	6
2	351.25	0				
3	641.75	290.5	0			
4	820.25	469	178.5	0		
5	982.75	631.5	341	162.5	0	
6	1475.5	1124.25	833.75	655.25	492.75	0
7	1841.75	1490.5	1200	1021.5	859	366.25
8	2123.75	1772.5	1482	1303.5	1141	648.25
9	2304.25	1953	1662.5	1484	1321.5	828.75
10	2767.5	2416.25	2125.75	1947.25	1784.75	1292
11	3118.75	2767.5	2477	2298.5	2136	1643.25
12	3409.25	3058	2767.5	2589	2426.5	1933.75
13	3587.75	3236.5	2946	2767.5	2605	2112.25
14	3750.25	3399	3108.5	2930	2767.5	2274.75
15	4242.75	3891.5	3601	3422.5	3260	2767.5

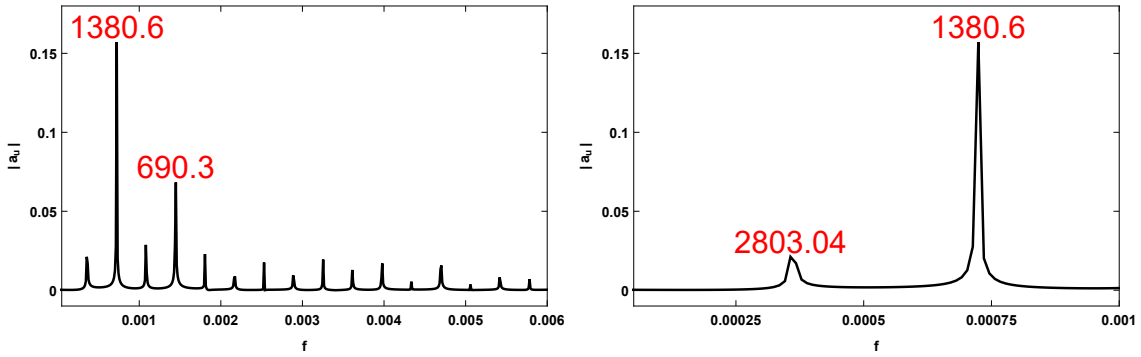

Figure 2.16: Fourier analysis plot for the Gray-Scott model for $D_u/D_v = 2$, with $D_u = 2 \times 10^{-5}$, and $h_t = 0.05$. For the right panel the x-axis shows the frequency domain with the two highest peaks shown with the corresponding periods. The period of the Fourier lowest frequency peak shown in the right panel is at 2803.04. This main peak is different from the value of 2767.5 obtained from analyzing the time series peak to peak separations.

The methods outlined in sections 2.5.1 and 2.5.2 together indicate that the perturbation induced patterns have characteristics showing that they are the result of several different interacting modes. Applying spatially localized perturbations to chaotic systems is uncharted territory and often gives intuitively unexpected results. The development and continual checking of analytic tools is required to explain and express observed results in a quantitative manner.

Chapter 3

Gray-Scott Reaction-Diffusion System

Parts of this chapter were adapted from our publication: Jason Czak and Michel Pleimling, "Spatiotemporal patterns emerging from a spatially localized time-delayed feedback scheme," Phys. Rev. E ***104****, 064213 (2021) [49]. "Copyright (2021) by the American Physical Society." We gratefully acknowledge funding from the Army Research Office through Grant No. W911NF-17-1-0156.* My contributions to this work are as follows: co-designing the research question, reviewing relevant literature, coding and implementing the time-delayed feedback schemes, generating all data, analyzing and interpreting the generated data, discussing the data in the context of earlier work, co-writing and editing the work.

3.1 Introduction

Spatio-temporal patterns [1, 2] are ubiquitous in nature and are found at scales ranging from the very small, bacterial colonies [50] and developmental biology [51], to the very large, as for example galaxy superclusters [4] or the Sloan Great Wall [5]. The spontaneous formation of patterns, a hallmark of systems far from equilibrium, has captivated the interest of researchers from a vast variety of disciplines. Common to many mechanisms yielding space-time patterns is the closeness to an instability (for example a chemical or hydrodynamics instability). Chemical reaction-diffusion systems [52] have been at the center of the investigations of pattern formation since Turing's seminal work [53], as they underpin many phenomena observed in nature and allow for both numerical and analytical approaches when cast in terms of coupled partial differential equations. Very rich space-time patterns, from chemical oscillations and Turing patterns [26] to spatio-temporal chaos [33], can be found in reaction-diffusion systems in open flow reactors that keep the systems far from equilibrium.

Controlling and designing space-time patterns has many potential applications. The goal is often either to design patterns and influence traveling waves [54, 55, 56, 57, 58] or to move

a chaotic system to a steady state or to an oscillatory behavior [7, 8, 9, 10, 11, 12, 13]. Experimentally, this control is achieved by exerting some external perturbation, involving for example photochemical energy transfer or temperature variations when dealing with chemical systems. Successful control protocols include the Ott-Grebogi-Yorke scheme [7] as well as time-delayed feedback control [8].

In this chapter we demonstrate that new space-time patterns can be generated in systems with (transient) chaos when using spatially localized invasive perturbations in the form of a time-delayed feedback scheme applied to a specified region of the system. We illustrate this through the creation in the one-dimensional Gray-Scott model of novel spatially localized time-dependent patterns. Our work differs both in the goals and in the scheme from other studies aiming at control of (transient) chaos in a spatially extended system. For example, in [12] time-delayed feedback control was used in order to control the transient chaos [33] regime and replace it in the whole system with other types of dynamic behavior, whereas for the pinning control of spatio-temporal chaos [59], a finite number of spatial pinning sites, arranged in optimal ways, are controlled in order to drive the whole system into a homogeneous steady state. Controlling the whole system or a finite number of specially arranged pinning sites does not result in the formation of new space-time patterns in a specified spatial region.

One remarkable finding of our work is that patterns can be stabilized locally that have periods orders of magnitude longer than the delay time used for the spatially localized perturbations. This is very different to reported [60, 61, 62] stabilizations of complex spatio-temporal dynamics near a subcritical Hopf bifurcation using global feedback control as for these systems the time delay is a multiple of the period of the newly stabilized periodic pattern. In our systems with spatially localized perturbations it is the interplay between time delay and spatial boundaries separating perturbed and unperturbed regions that generates the long-period patterns discussed in the following study.

The chapter is organized in the following way. In chapter 3.2 we briefly remind the reader about some relevant aspects of the Gray-Scott model before discussing the application of time-delayed feedback scheme to this type of reaction-diffusion systems. Chapter 3.3 presents the novel space-time patterns that emerge when applying in the chaotic regime the time-delayed feedback scheme to part of the system only. Two scenarios are discussed, leading in one case to perfect periodic patterns, whereas in the other case the pattern is impacted by noise generated from diffusion across the boundaries separating the perturbed and unperturbed regions. Chapter 3.4 presents the effects of noise on the system along with additional patterns that can be formed. In chapter 3.5 we conclude and provide an outlook on broader applications of the scheme discussed in this work.

3.2 Model and Method

The Gray-Scott model [25] is a reaction-diffusion system that displays very rich and complex space-time patterns in one [27, 41, 42, 63, 64, 65] and two [66, 67, 68] space dimensions. This cubic autocatalytic system in an open flow reactor is governed by the reactions

$$U + 2V \longrightarrow 3V \ , \qquad V \longrightarrow P \ , \tag{3.1}$$

where the substrate U is continuously supplied and the inert product P is removed. As outlined in chapter 2 the corresponding deterministic kinetic equations for the space- and time-dependent species concentrations $u(\mathbf{x}, t)$ and $v(\mathbf{x}, t)$ are often cast in the form

$$\frac{\partial u}{\partial t} = D_u \nabla^2 u - uv^2 + A(1-u) \tag{3.2}$$

$$\frac{\partial v}{\partial t} = D_v \nabla^2 v + uv^2 - (A+B)v \tag{3.3}$$

with the species-dependent diffusion rates D_u and D_v as well as the rate B of converting V into the inert product and the rate A of feeding U into the reactor and of removing the different species from the reactor. Whereas for $D_u \gg D_v$ propagating pulses and pulse splittings dominate, for $D_u \gtrsim D_v$ a variety of regimes, including traveling pulses, spatio-temporal chaos, and self-replicating patterns, are encountered, depending on the values of the rates A and B.

In this work we restrict ourselves to the ratio $D_u/D_v = 2$ which is known to yield (transient) chaotic space-time patterns as a result of an inhomogeneous initial state. We follow previously published work and select as initial state the state with $(u, v) = (0.5, 0.25)$ in a small central region and $(u, v) = (1, 0)$ everywhere else. The resulting dynamic phase diagram and the corresponding space-time plots for u are shown in Fig. 3.1. The regimes outlined in chapter two are briefly summarized. Regime 1 is characterized by individual traveling pulses that either die out quickly, yielding the trivial steady state $(u, v) = (1, 0)$, or continue to propagate. In regime 2, pulse splitting results in the generation of additional lines and the formation of domains that evolve temporally. Regime 3 is the transient chaotic regime that results from the interaction between a Hopf instability and a Turing instability [27, 41, 42]. This transient chaotic regime, which sees the appearance and disappearance of small regions where the densities u and v take on values close to those of the trivial steady state, is confined to a rather narrow region in parameter space. Finally, for large inflow rates A the system settles into a non-trivial steady state with $u \neq 0$ and $v \neq 0$ (regime 4).

The left panel in Fig. 3.2 shows more clearly the transient chaotic regime that emerges for $D_u/D_v = 2$, $A = 0.0234$, and $B = 0.05$. The controlled patterns obtained in [12], where time-delayed feedback control was applied to the system as a whole, included a non-trivial steady state with $u \neq 0$ and $v \neq 0$, shown in the right panel of Fig. 3.2 for the same parameter values as for the left panel, as well as coarsening patterns and traveling waves. As discussed in the following, when applying a time-delayed feedback scheme to only parts

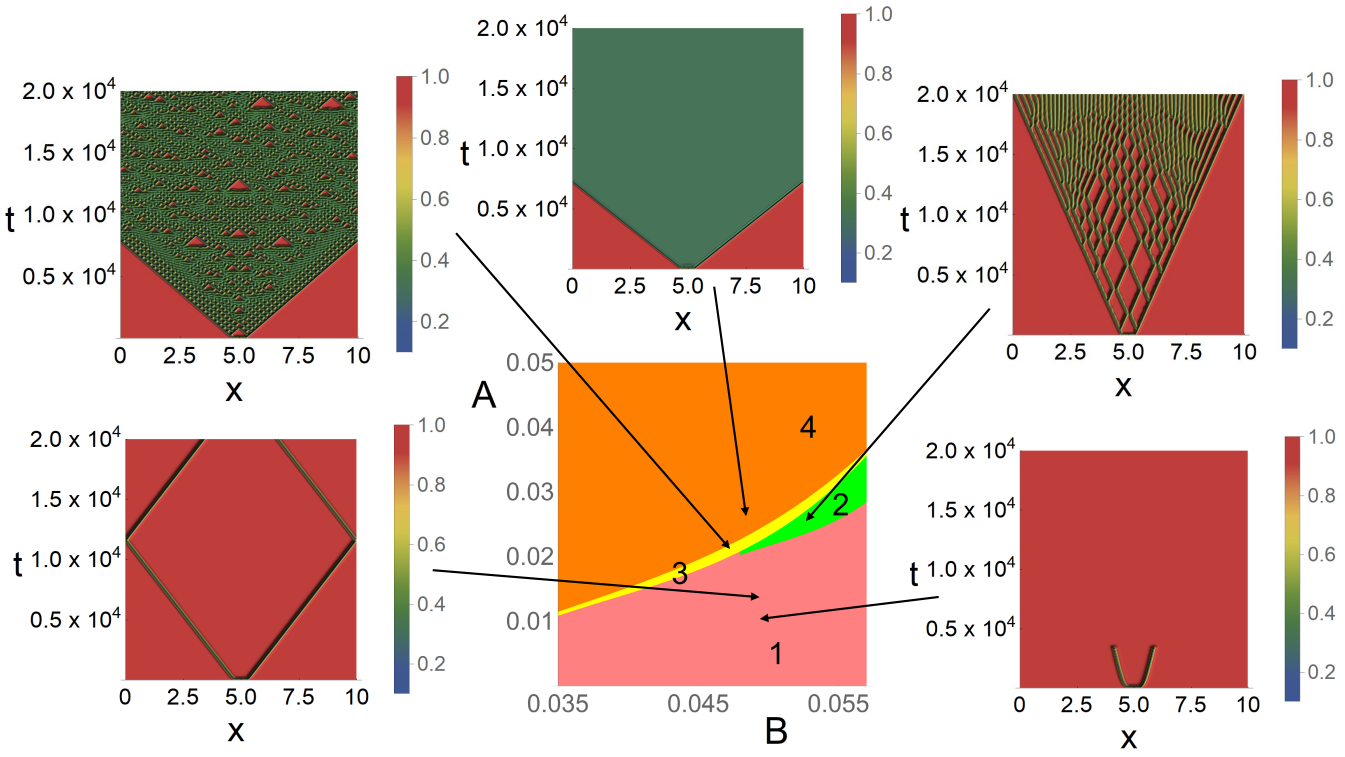

Figure 3.1: The different dynamic regimes encountered for $D_u/D_v = 2$, with $D_u = 2 \times 10^{-5}$ and $D_v = 10^{-5}$, and an inhomogeneous initial state with $(u, v) = (0.5, 0.25)$ in a small central region and $(u, v) = (1, 0)$ otherwise. Space-time plots for u are obtained through numerical integration of the discretized versions of Eqs. (3.2) and (3.3), using periodic boundary conditions. The time increment is chosen as $h_t = 0.05$. The width of the system is $L = 10$, and 1024 grid points are used for the spatial discretization.

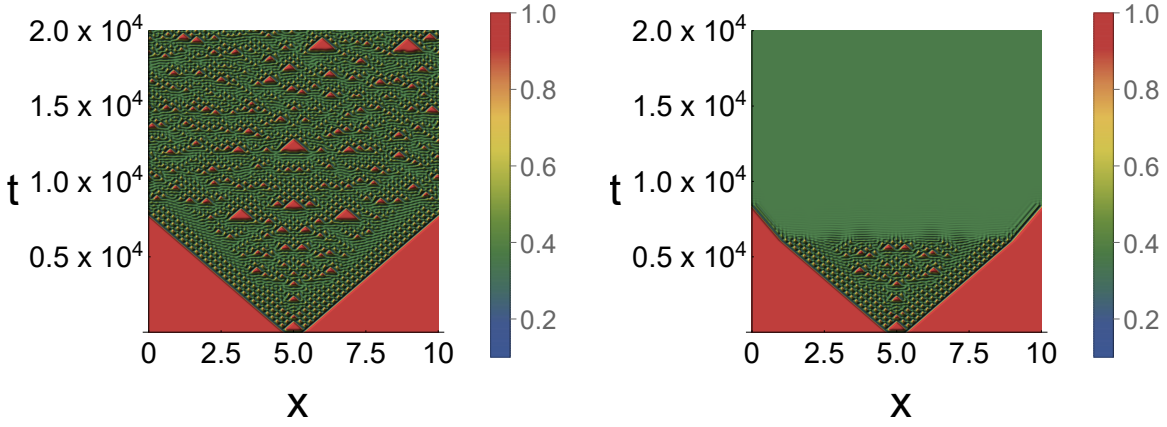

Figure 3.2: (Left) Spatio-temporal chaos in the one-dimensional Gray-Scott model that results from an inhomogeneous initial state. Shown is $u(x,t)$. The parameters are $D_u/D_v = 2$, $A = 0.0234$, and $B = 0.05$. The initial state is $(u,v) = (1,0)$, with the exception of the region in the middle where $(u,v) = (0.5, 0.25)$. (Right) When controlling the whole system using time-delayed feedback control, spatio-temporal chaos is suppressed and a non-trivial steady state with $u \neq 0$ and $v \neq 0$ can be stabilized [12]. The perturbation, which starts at $t = 6,000$, is characterized by the strength $K = -0.02$ and the delay time $\tau = 0.5$.

of the system, spatially localized ordered patterns can be stabilized. These patterns are not encountered when controlling the whole system [12].

In our protocol of perturbing the substrate in a spatially localized way, Eq. (2) is replaced in some region $\mathcal{C}$ with

$$\begin{aligned} \frac{\partial u(\mathbf{x},t)}{\partial t} &= D_u \nabla^2 u(\mathbf{x},t) - u(\mathbf{x},t)v(\mathbf{x},t)^2 + A(1-u(\mathbf{x},t)) \\ &\quad + K\left(u(\mathbf{x},t-\tau) - u(\mathbf{x},t)\right) \end{aligned} \tag{3.4}$$

with the perturbation strength K and the delay time τ. We present below numerical results for the value $\tau = 0.5$. When the region $\mathcal{C}$ is the whole system, we of course recover the situation studied in [12].

Kyrychko et al. [12] pointed out that the effective perturbation strength is $|K|\tau$ when this scheme is applied to the system as a whole. In our work we perturb the system only locally, and, while the effective control strength is still provided by $|K|\tau$, different local patterns are stabilized depending on the sign of K. As a result, additional constraints are imposed on the values of the delay time for which these patterns can be stabilized. For $K = -0.03$, which is the negative value we focus on in the following, periodic patterns are stabilized in the unperturbed region for $0.45 < \tau < 1.75$. For $K = 0.025$, the positive value explored later in this work, we observe the appearance of approximate periodic patterns for a very wide range of delay times, with $0.45 < \tau < 10$, where $\tau = 10$ is the longest delay time that we investigated.

Applying periodic boundary conditions, the discretized versions of the differential equations given above are integrated using the fourth order Runge-Kutta algorithm and an eighth order finite difference method for the diffusion terms. This results in a very stable integration scheme. Still, the symmetry imposed by the initial condition used for Fig. 3.2 is lost in the chaotic regime at very long times (for t of the order of 1.5×10^4 in the left panel of Fig. 3.2) due to the accumulation of numerical errors. We checked that the loss of right-left symmetry sets in much earlier when using a lower order discretization of the diffusion term.

3.3 Results

The two scenarios discussed in the following for the one-dimensional Gray-Scott model have in common that we let the system shown in the left panel of Fig. 3.2 evolve for some time and then perturb in a specified region the substrate using time-delayed feedback. For the first case discussed below, we show that applying a perturbation to a broad region the system with $K < 0$ may yield in the *unperturbed* region a perfectly periodic pattern. On the other hand, if the feedback strength parameter is positive, $K > 0$, then noisy repeating patterns can be stabilized in the *perturbed* region, where the noise results from diffusion across the boundary separating the perturbed from the unperturbed, and therefore chaotic, region.

3.3.1 $K < 0$

As shown in the right panel of Fig. 3.2, controlling the whole system with $K < 0$ results in the suppression of spatio-temporal chaos everywhere and in the global stabilization of the non-trivial steady state. This is the only non-chaotic regime that can be stabilized globally for negative K [12]. Restricting this protocol to a part of the system suppresses chaos only locally so that this non-trivial steady state is not established everywhere. Instead, as shown in the top left panel of Fig. 3.3, in the unperturbed region the system spontaneously organizes into a perfectly periodic structure, dominated by periodically appearing space-time regions, shown as red triangles, where the trivial steady state $(u, v) = (1, 0)$ is approximated. This periodic pattern has a remarkably long period $T \approx 2,700$, almost four orders of magnitude larger than the delay time $\tau = 0.5$ used in the feedback. Inspection of the time-dependent species concentration u in the middle of the unperturbed region, see Fig. 3.4, reveals that within one period the concentration u displays two pronounced maxima, corresponding to two red triangles in the space-time plot. As shown in Fig. 3.5 the amplitude $|a_u|$ of the Fourier transform of $u(t)$ in this part of the system also reveals this complex periodic pattern and exhibits as a function of the frequency f sharp peaks at the relevant frequencies.

The emergence of this periodic pattern is independent of the location of the unperturbed region. The top right panel in Fig. 3.3 shows that the same structure emerges when the unperturbed region is off-center. However, the time needed to establish the pattern can

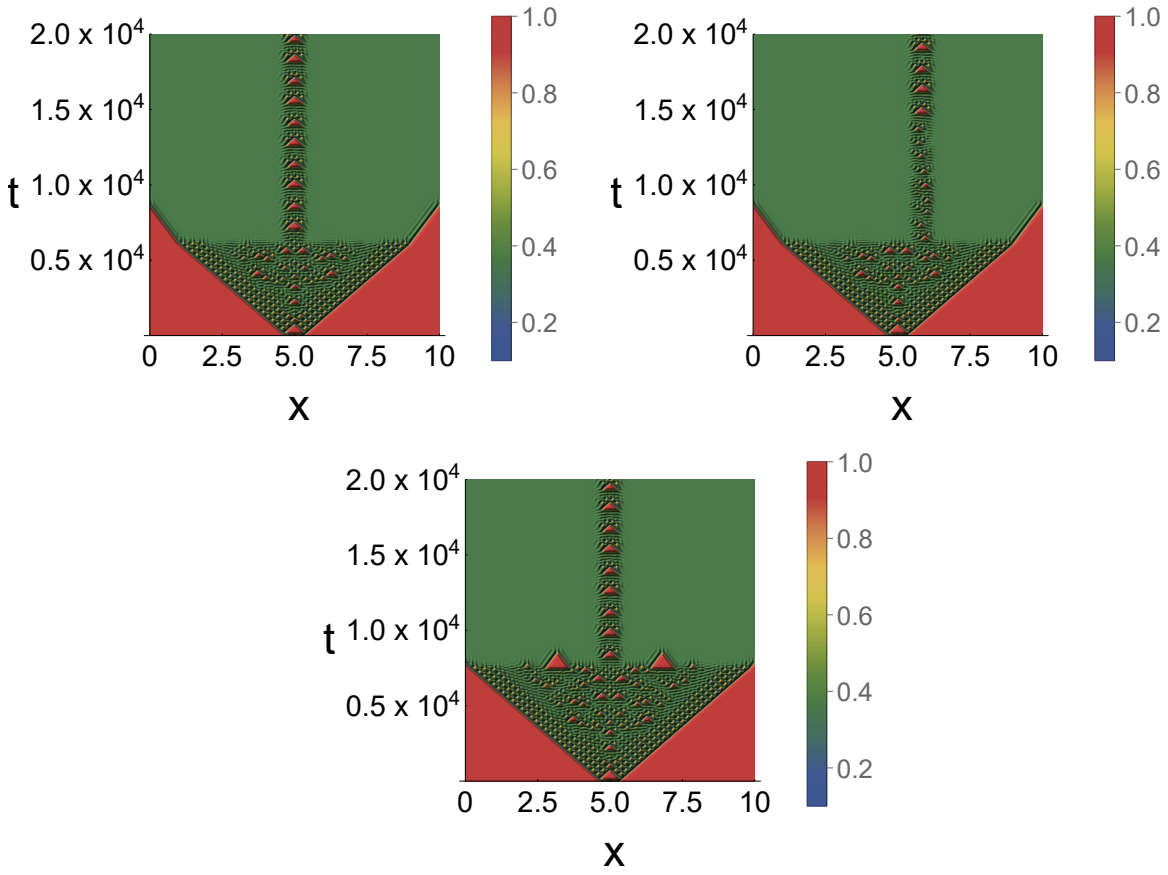

Figure 3.3: (Top left) Using time-delayed feedback for species U everywhere in the system with the exception of the central region of width $W_{un} = 0.625$ induces a periodic pattern in the *unperturbed* region. The period of the resulting oscillations in the unperturbed region is many orders of magnitude larger than the delay time $\tau = 0.5$. For this plot the strength $K = -0.03$ was used and the perturbation started at $t = 6,000$. (Top right) The same as in the top left panel, but now the unperturbed region has been shifted by 0.83 to the right when compared to the case on the left. The time needed to establish the periodic pattern depends on the state of the system at the location of the unperturbed region just before the localized time-delayed feedback scheme sets in. (Bottom) The same as in the top left panel, but now with the perturbation starting at $t = 7,500$. Even so the state at the onset of the perturbation differs from that at $t = 6,000$, the same periodic pattern is stabilized. For all figures the parameter values are $D_u/D_v = 2$, $A = 0.0234$, and $B = 0.05$.

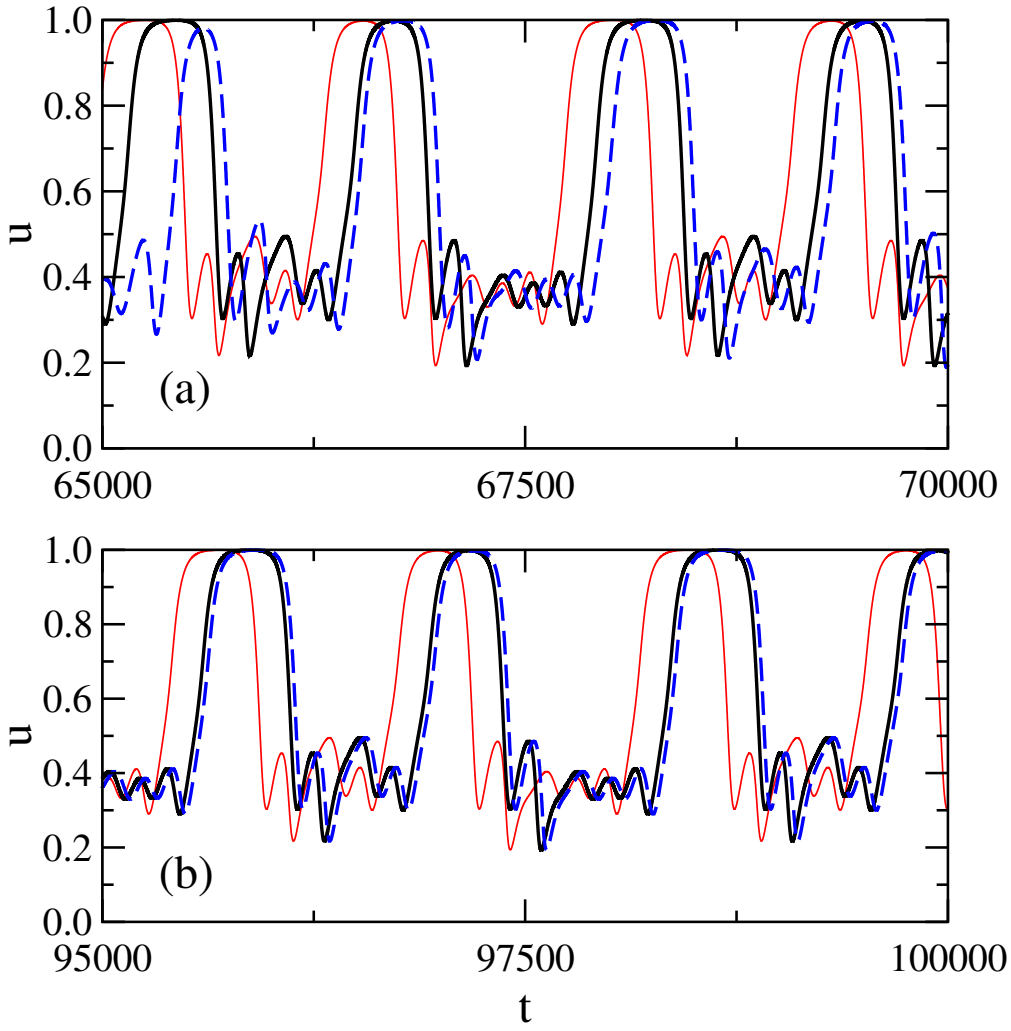

Figure 3.4: Time-dependent concentration u in the middle of the unperturbed region for the three perturbation times $t_p = 6,000$ (black lines), $t_p = 7,500$ (red lines), and $t_p = 60,000$ (dashed blue lines), see top left and bottom panels in Fig. 3.3 for the corresponding space-time plots: (a) t between 65,000 and 70,000; (b) t between 95,000 and 100,000. When applying the time-delayed feedback outside of the middle region, the species concentration after some transient behavior (visible for $t_p = 60,000$ in panel (a)) locks into a periodic pattern with a period $T \approx 2,700$. This periodic pattern, once established, is independent of the perturbation time, the only difference being an overall time shift as the periodic pattern sets in at different times for the different perturbation times. The parameters used in this figure are the same as in Fig. 3.3.

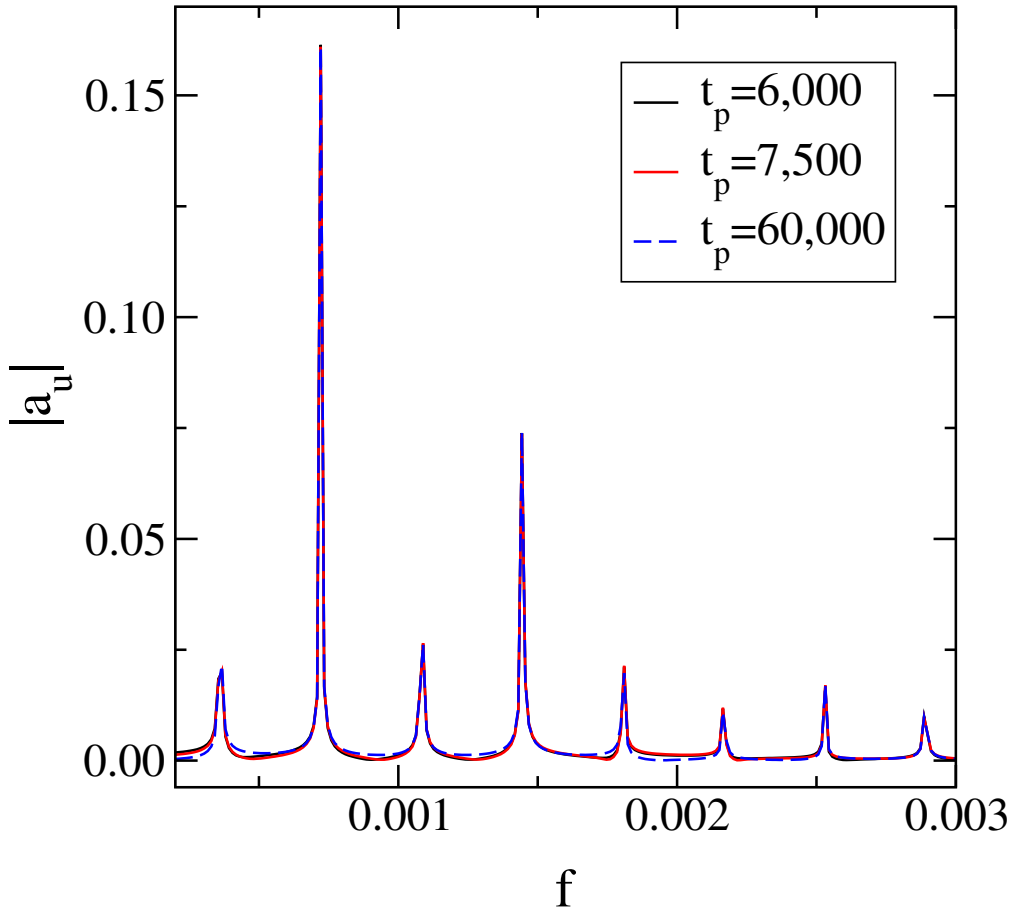

Figure 3.5: Frequency-dependent amplitude of the Fourier transform of the time-dependent concentration u in the middle of the unperturbed region of width $W_{un} = 0.625$, see Fig. 3.4 for the corresponding time series. The very sharp peaks in the Fourier transform indicate that within the unperturbed region the pattern is repeated perfectly. The shown data for three different perturbation times ($t_p = 6,000$, $t_p = 7,500$, and $t_p = 60,000$) exhibit the same prevailing frequencies, as revealed by the identical positions of the peaks. This indicates that the emerging periodic pattern is robust and independent of the perturbation time.

vary substantially, which reveals a dependence on the state of the unperturbed region at the moment the perturbation sets in. The width W_{un} of the unperturbed region is a relevant quantity, as the perfect periodic pattern is not observed for all widths of the unperturbed region. Indeed, for $W_{un} \gtrsim 1.1$, the unperturbed region maintains the chaotic property of the original system. On the other hand, if $W_{un} \lesssim 0.2$, spatial and temporal inhomogeneities die out in the unperturbed region and the system as a whole is pushed into the non-trivial steady state. The range of widths W_{un} of the unperturbed region for which periodic patterns can be induced is independent of the linear extent of the system.

We also remark, see the bottom panel in Fig. 3.3 as well as the corresponding time-dependent concentration in Fig. 3.4, that the emerging pattern is independent of the perturbation time itself (provided that chaotic behavior is present when the perturbation sets in). This is clearly visible in Fig. 3.4 when comparing the time-dependent concentrations for different perturbation times. The observed overall time shift is a consequence of the fact that the periodic patterns set in at different times for the different situations.

Fig. 3.6 explores how the period T of the repeating pattern changes when the system parameters are changed. In the main image we show the period as function of the feedback strength K, keeping the other parameters constant at the values used for Figures 3.3, 3.4, and 3.5. In the two insets, we show how the period changes when varying the flow rate A (lower left inset) or the rate B to produce the inert product (upper right inset), while keeping all other parameters constant. These plots also provide an indication of the extent to which the parameters can be varied around our standard set $K = -0.03$, $A = 0.0234$, and $B = 0.5$ while still generating a periodic pattern. Increasing the rate B yields a substantial increase of the period. On the other hand changing the flow rate A yields changes in the form of an approximate linear decrease for increasing A. Keeping A and B constant while merely changing the value of K means that any change to the period is exclusively due to the details of the feedback scheme. It is then interesting to note that an increase of the magnitude of K increases the time between successive repetitions of the pattern. We also remark that values $|K| < 0.028$ do not allow to stabilize the periodic pattern, but that instead chaotic patterns persist in the unperturbed region. On the flip side, large negative values, with $K < -0.042$, tend to destabilize the periodic pattern, once established, resulting in an intermittent behavior where time intervals with repeating patterns are interrupted by time intervals where the behavior is no longer fully periodic. Therefore outside of the interval $-0.042 < K < -0.028$ no period can be measured due to the absence of repeating patterns.

At first look it might seem that the periodic pattern emerging in the unperturbed region is mainly a consequence of exposing a region of the right size to a fixed boundary condition provided by the adjacent steady-state region. A closer inspection, however, reveals that the feedback scheme is the necessary ingredient to generate periodic patterns. This is illustrated in Fig. 3.7 for the system with our standard parameters. With the feedback scheme in place, the pattern remains perfectly periodic for as long as we follow the time evolution of the system (left panel). In the right panel, we remove the time-delayed feedback (by setting $K = 0$) at $t = 25,000$, indicated by the dashed horizontal line. Without the continuous application

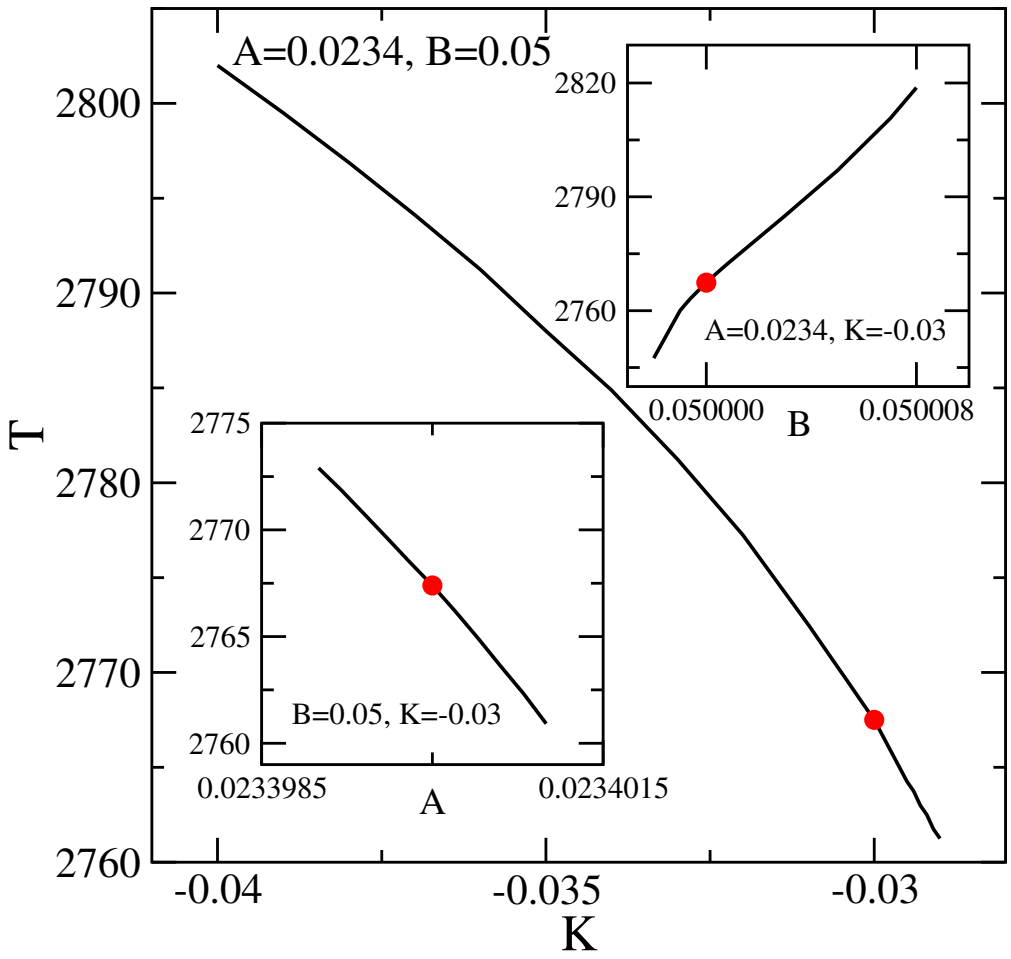

Figure 3.6: Dependence of the period T of the repeating pattern when changing the feedback strength K (main image), the flow rate A (lower left inset) or the rate B of converting V into an inert product (upper right inset). We explore the parameter range around the values $K = -0.03$, $A = 0.0234$, and $B = 0.5$, used in the Figures 3.3, 3.4, and 3.5, and indicated by the red dot in each panel. For each plot, two parameters are kept constant, as indicated in the panels, and the third is varied. As for the earlier figures, $D_u/D_v = 2$, whereas the width of the unperturbed region is $W_{un} = 0.625$.

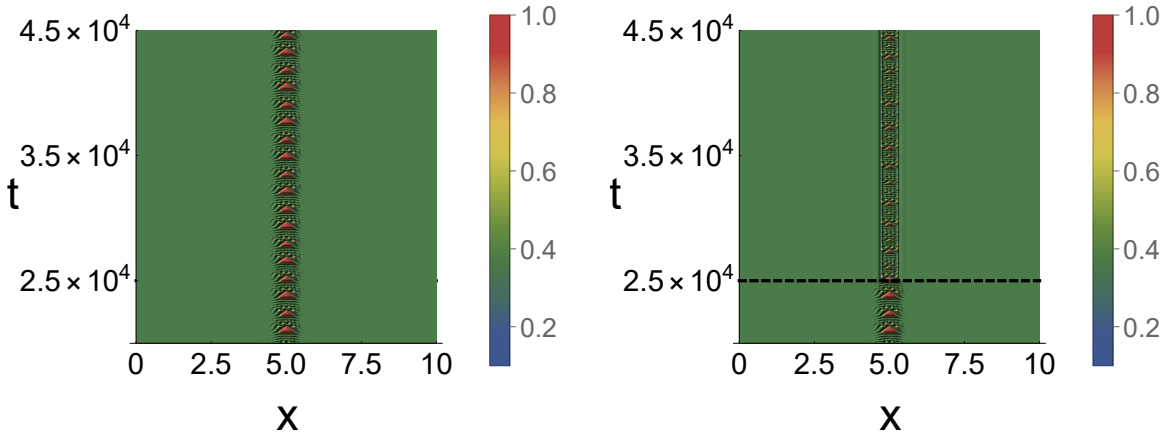

Figure 3.7: (Left) The same system as in the left panel of Fig. 3.2 in the time interval between $t = 20,000$ and $t = 45,000$. (Right) The same system, but now with the time-delayed feedback switched off at $t = 25,000$, indicated by the dashed line. This results in the loss of the periodic pattern in the unperturbed region.

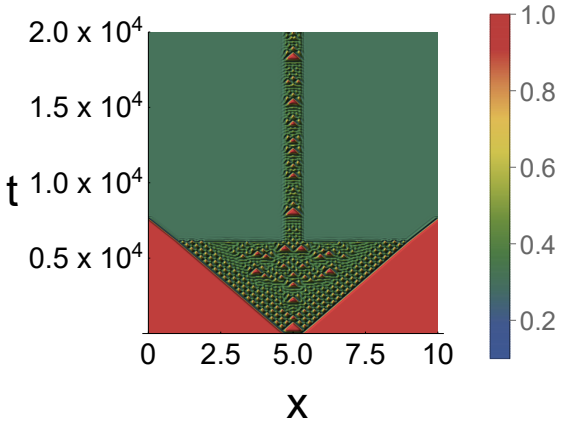

Figure 3.8: Space-time plot where at $t = 6,000$ we change in the 'perturbed' region the value of A from 0.0234 to 0.03, which drives that part of the system into the non-trivial steady state. This protocol, however, does not yield a periodic pattern in the 'unperturbed' region.

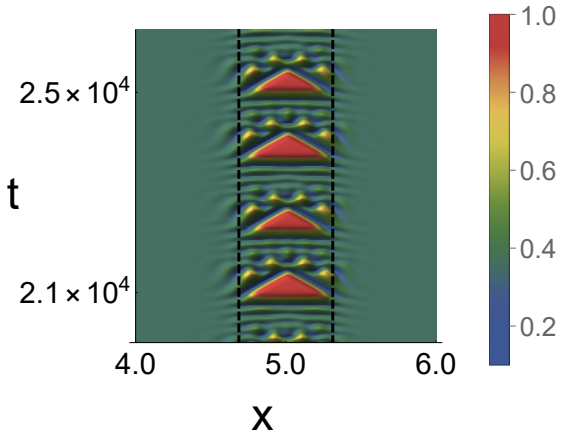

Figure 3.9: A zoom into the periodic pattern from the left panel of Fig. 3.7 that reveals complex pattern in the perturbed part of the system close to the boundaries (indicated by the vertical dashed lines) with the unperturbed part. Without these features extending into the perturbed part, periodic pattern can not be established in the unperturbed region.

of the time-delayed feedback, the periodic pattern is immediately lost and replaced by the random appearance of small red triangles in the space-time plot. The absence of periodic pattern is also noted in Fig. 3.8 where instead of switching on the time-delayed feedback scheme at $t = 6,000$ we make in the same region an instantaneous change of A from 0.0234 to 0.03, a value for which an unperturbed system settles into the global non-trivial steady state, see Fig. 3.1. Clearly, periodic patterns are not emerging when patching together a chaotic region with a region that displays a steady state, i.e. when imposing on the chaotic region fixed boundary conditions that result from the adjacent steady-state region.

A zoom of the space-time pattern that results from using locally the time-delayed feedback scheme, see Fig. 3.9, reveals the formation of a transition region that straddles the boundary separating the perturbed and unperturbed regions. These features die out further away from the boundary which results in the local establishment of the homogeneous steady state. It is the presence of the diffusion term that, in conjunction with the time-delayed feedback, generates the formation of this transition region necessary for the emergence of periodic patterns with periods orders of magnitude larger than the delay time.

3.3.2 $K > 0$

A second protocol for perturbing only part of the system is explored in Figures 3.10 and 3.11. We choose the same parameter values as for the results presented above, with the one change that the strength $K = 0.025$ is now positive. Using these parameter values for a time-delayed feedback control of the whole system, one observes that the system is pushed into the trivial steady state with $(u, v) = (1, 0)$. However, applying this scheme to only

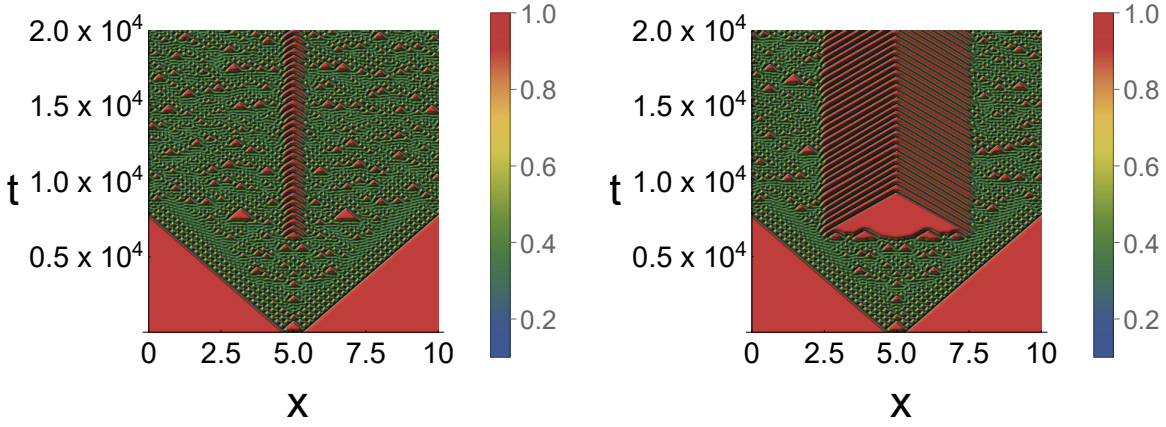

Figure 3.10: Time-delayed feedback applied to only a part of the system with $K > 0$ yields non-trivial patterns in the perturbed region, while spatio-temporal chaos persists in the unperturbed region. The values of the rates and of the delay time used for these panels are the same as for the panels in Fig. 3.2, with the exception of the strength which is $K = 0.025$. The width W of the perturbed region is $W = 0.625$ in the left panel, while in the right panel half of the system is subjected to time-delayed feedback scheme.

part of the system yields a very different behavior, as shown in Fig. 3.10. Whereas in the unperturbed region spatio-temporal chaos persists, in the *perturbed* region an approximate periodic pattern is established where successive maxima are separated by a time interval $T \approx 440$, which is three orders of magnitude larger than the delay time. One way to look at this pattern is a succession of pulses that are generated at both interfaces with the chaotic regime, which acts as provider of a temporally fluctuating boundary condition. These pulses, after progressing through the perturbed region, undergo pair annihilation upon encounter. Inspection of the Fourier transform, see Fig. 3.11, reveals the imperfect oscillations in the form of a wide noisy peak at a frequency close to $f = 0.0023$, but the imperfect nature of the repeating pattern is also readily seen from the time-dependent species concentration shown in the inset.

The two panels in Fig. 3.10 differ by the width of the perturbed region. In fact, the approximate periodic pattern is observed for most widths, with the exception of very small regions ($W \lesssim 0.3$), for which no persisting regular pattern can be established, and very large regions ($L - W \lesssim 0.3$) which end up in the trivial steady state, similar to the fully controlled system. It follows that for this case the range of widths for which approximate periodic pattern emerge in the perturbed region scales linearly with the system size. The formation of this pattern needs a strength $K > 0.015$, as for very small K a regular pattern can not be stabilized and the system remains in the chaotic regime. For cases that result in the imperfect oscillations, the average time elapsed between successive maxima depends slightly on the value of K.

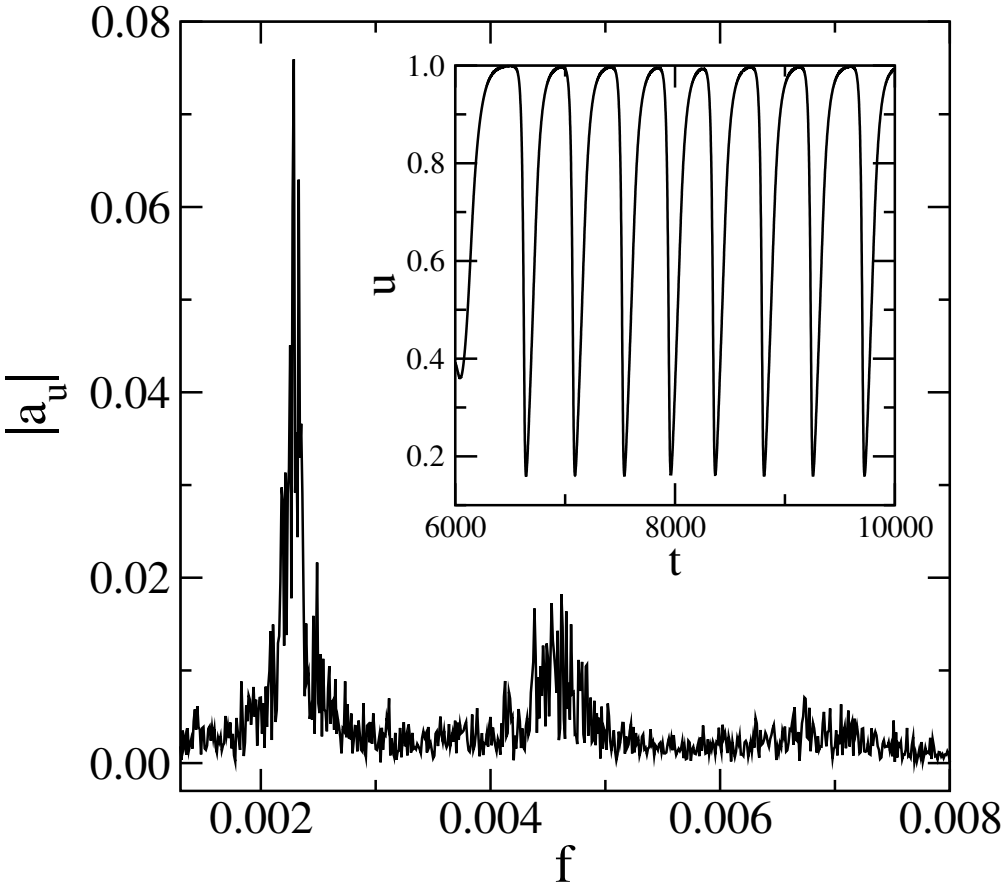

Figure 3.11: Frequency-dependent amplitude of the Fourier transform of the time-dependent concentration u in the middle of the perturbed region, see the left panel in Fig. 3.10 for the corresponding space-time plot. The time series $u(t)$ shown in the inset reveals an imperfect repeating pattern with successive maxima separated by a time interval $T \approx 440$.

3.4 Additional pattern formations

The results obtained for this section will use the following parameters: $D_u/D_v = 2$, $A = 0.0234$, and $B = 0.05$, unless otherwise stated. The initial state chosen has $(u, v) = (0.5, 0.25)$ in a small central region and $(u, v) = (1, 0)$ everywhere else.

3.4.1 Noise effects

In our protocol of perturbing the substrate in a spatially localized way, Equation 3.4 is replaced in some region $\mathcal{C}$ with

$$\begin{aligned} \frac{\partial u(\mathbf{x},t)}{\partial t} &= D_u \nabla^2 u(\mathbf{x},t) - u(\mathbf{x},t)v(\mathbf{x},t)^2 + A(1-u(\mathbf{x},t)) \\ &\quad + K\left(u(\mathbf{x},t-\tau) - u(\mathbf{x},t)\right) + N_s\eta(\mathbf{x},t), \end{aligned} \tag{3.5}$$

where $\eta(x,t)$ is noise from a square distribution $[-0.25, 0.25]$ with strength N_s [69, 70, 71, 72, 73].

The noise shown in Equation 3.5, which acts as perturbation, is applied to the chaotic state of the Gray-Scott model system. The effect of noise applied to the system is shown in Figures 3.12, 3.13, 3.14 and 3.15. The general behavior of the system with noise is the formation of larger domains of substrate and activator regions, shown in Figures 3.12 and 3.13. The effect applied to a local region as shown in Fig. 3.13 does not extend beyond the boundary region. These regions abruptly stop at the zone boundaries due to concentrations greater than unity being quickly washed out by the substrate feed A. The observed effects quickly dissipate once the application of the noise perturbation is ceased, as shown in Fig. 3.14. With the additional application of the time-delayed feedback the noise initially hinders the formation of periodic patterns as shown in Fig. 3.15. The system needs a longer time to form periodic structures once the noise is ceased. The period and structure of the periodic pattern are unaffected by the application of noise.

3.4.2 Two separate perturbation regions

As we have seen in the earlier sections a localized perturbation in the form of a time-delayed feedback can form periodic structures. In this section we investigate the effect of having two spatially separated regions or wells with perturbations applied in each. The parameter W_s is the separation between the center of the two wells. The well separations needs to be above a certain value as otherwise the regions will interact and just form one large region. The effect of varying the separation between two unperturbed regions gives different initial configurations for the separate wells. As shown in Fig. 3.16 the individual wells have distinct pattern onset times related to their initial state. The periodic patterns formed over

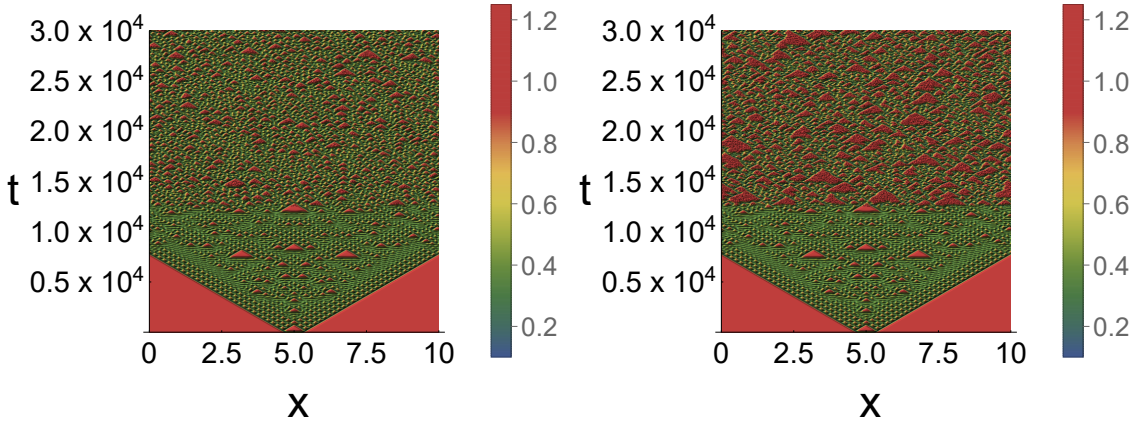

Figure 3.12: The effect of rectangular noise on the system starting at a set time t =12,500 and continuing onward. Left: $N_s = 0.5$, right: $N_s = 1$. We see a general trend for a large noise strength that the substrate domains become larger and form rougher edges.

long times shown in Fig. 3.17 are identical for wells with the same surrounding perturbation strength. Individual wells have periodic patterns related to their surrounding perturbation regions, shown in Figures 3.18 and 3.19. The periodic patterns formed have distinct peak to peak pattern while maintaining nearly indistinguishable Fourier peaks as shown in the bottom panels of Fig. 3.19. The results for the two well system further strengthen that the periodic patterns depend upon the K values used as discussed in Section 3.3.1. Even in cases with a very limited perturbation region as shown in Fig. 3.20 periodic patterns will be formed. The patterns will be formed so long as the width is above a certain threshold otherwise the regions will interact. The same general results hold true for positive K values as shown in Fig. 3.21, where we see that the different wells have structures depending upon the perturbation strength applied.

3.4.3 Past time delay feedback

The methods outlined in Section 2.4.1 can be applied to the Gray-Scott chaotic regime. For positive values of feedback as shown in Fig. 3.22 the set time feedback shows the formation of periodic structures. As the run time increases the periodic structures formed break down as shown in Fig. 3.23.

3.5 Conclusions and outlook

Systems with transient chaos can be forced into different dynamic regimes through an external intervention. Protocols proposed for this include spatially arranged pinning sides as well

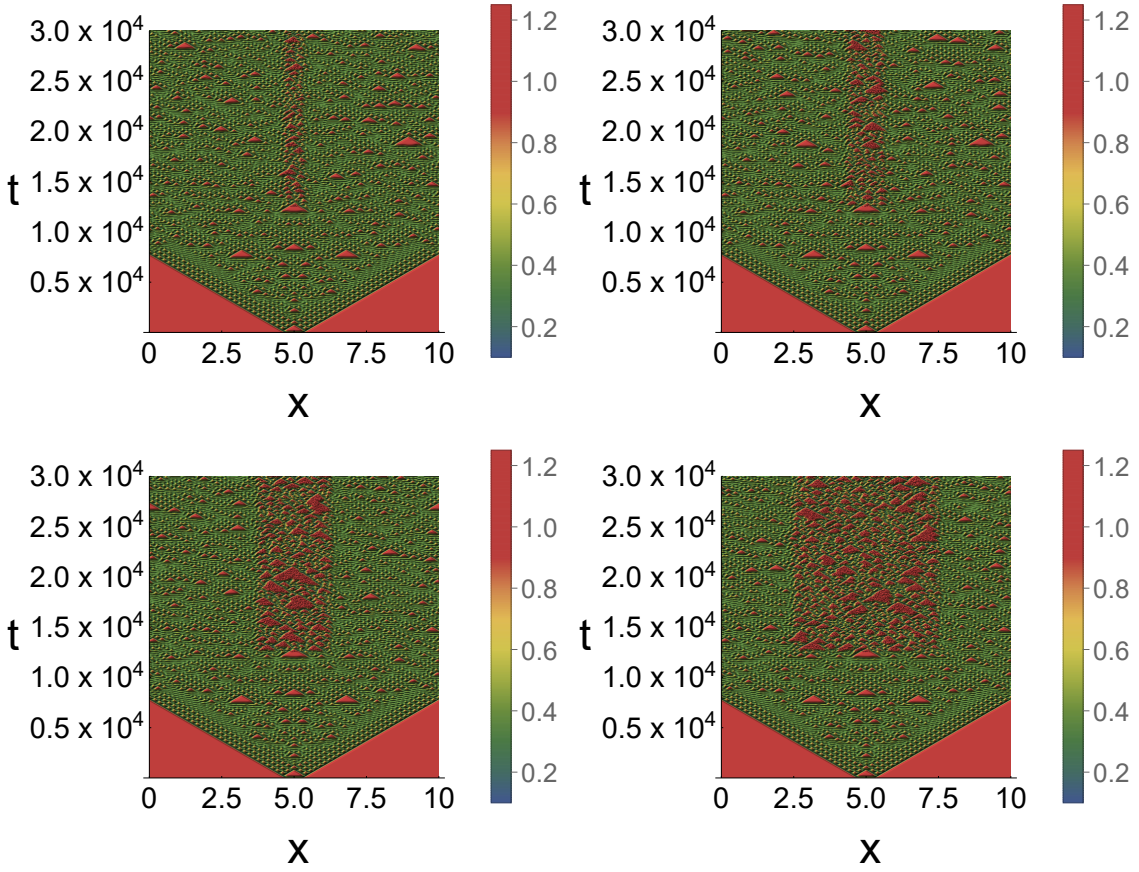

Figure 3.13: The effect of noise, applied locally to a region with width W, starting at a set time $t = 12,500$ and continuing onward. The noise strength value is $N_s = 1$ for all the results. Top Left: $W = 0.625$, top right: $W = 1.25$, bottom left: $W = 2.5$, bottom right: $W = 5$. The main effect here is that for larger regions with noise the merging structure size increases.

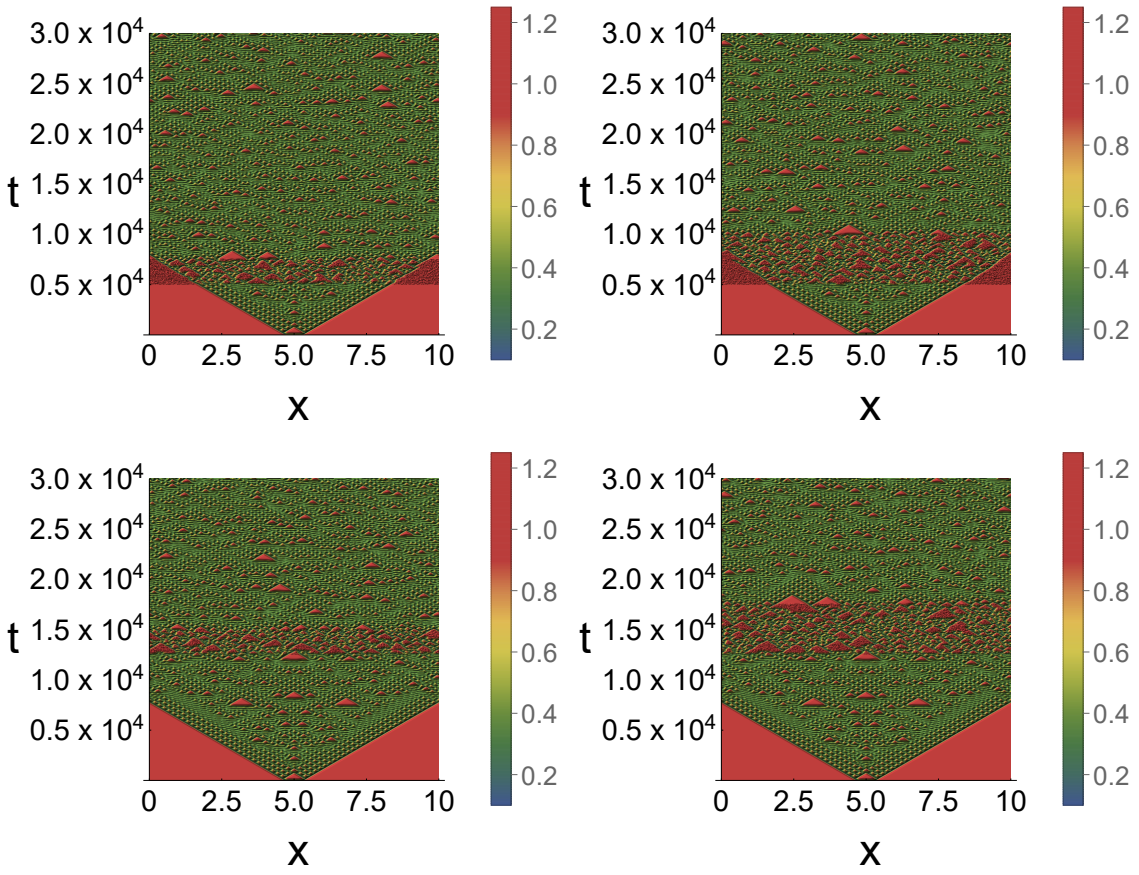

Figure 3.14: The effect of noise on the system starting at a different times and continuing for varying amounts of time. The noise strength value is $N_s = 1$ for all the results. Top left: starting time $t = 5,000$, ending time $t = 7,500$. Top right: starting time $t = 5,000$, ending time $t = 10,000$. Bottom left: starting time $t = 12,500$, ending time $t = 15,000$. Bottom right: starting time $t = 12,500$, ending time $t = 17,500$. The results consistently show that once the application of noise is stopped the system returns to the same behavior as before the noise was applied.

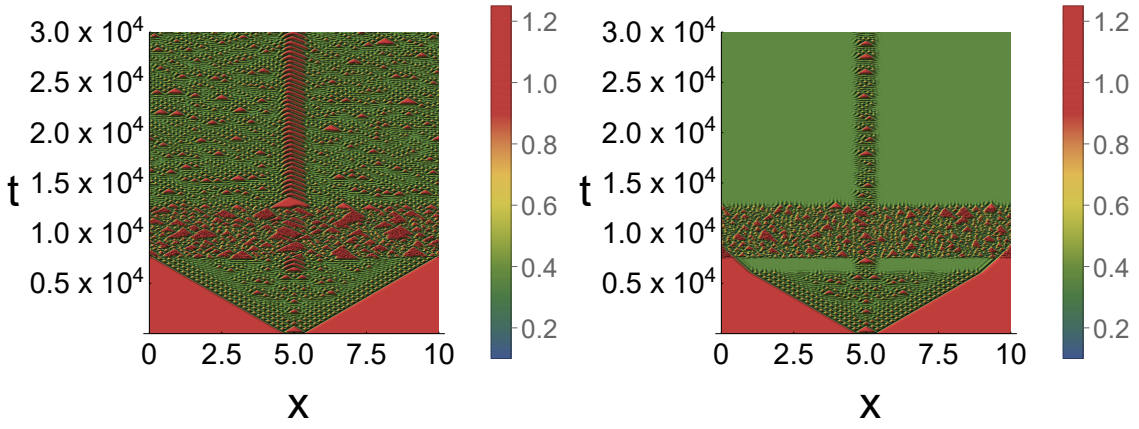

Figure 3.15: Effect of noise in systems with time-delayed feedback applied at $t = 6,000$ time steps for the inside region for the left panel and outside region for the right panel. Left: $K = 0.025$, noise starting time $t = 7,500$, ending time $t = 12,500$. Right: $K = -0.03$, noise starting time $t = 7,500$, ending time $t = 12,500$. The noise acts as an new initial condition for the chaotic behavior and the same resulting periodic patterns are formed after long enough time spans.

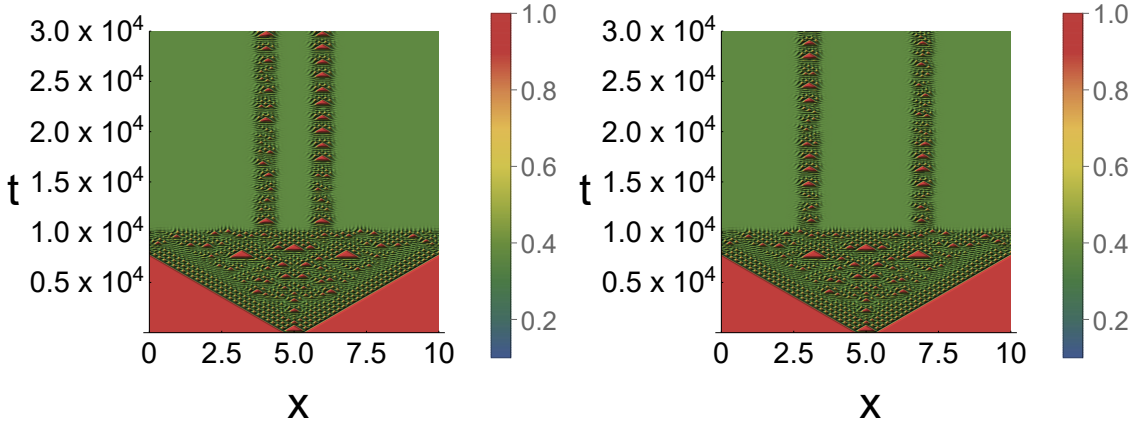

Figure 3.16: The effect of time delayed feedback on two spatially separated regions within the same system. A negative time delayed feedback perturbation of strength $K = -0.03$ is applied to the system at $t = 10,000$ for all regions excluding the two wells. The size of both unperturbed regions is equal at $W_u = 0.625$ with a varying separation between the two wells. Left $W_s = 1.953125$, right: $W_s = 3.90625$. The initial configurations at the start of the perturbation are different for the two wells yielding different times before periodic patterns are formed.

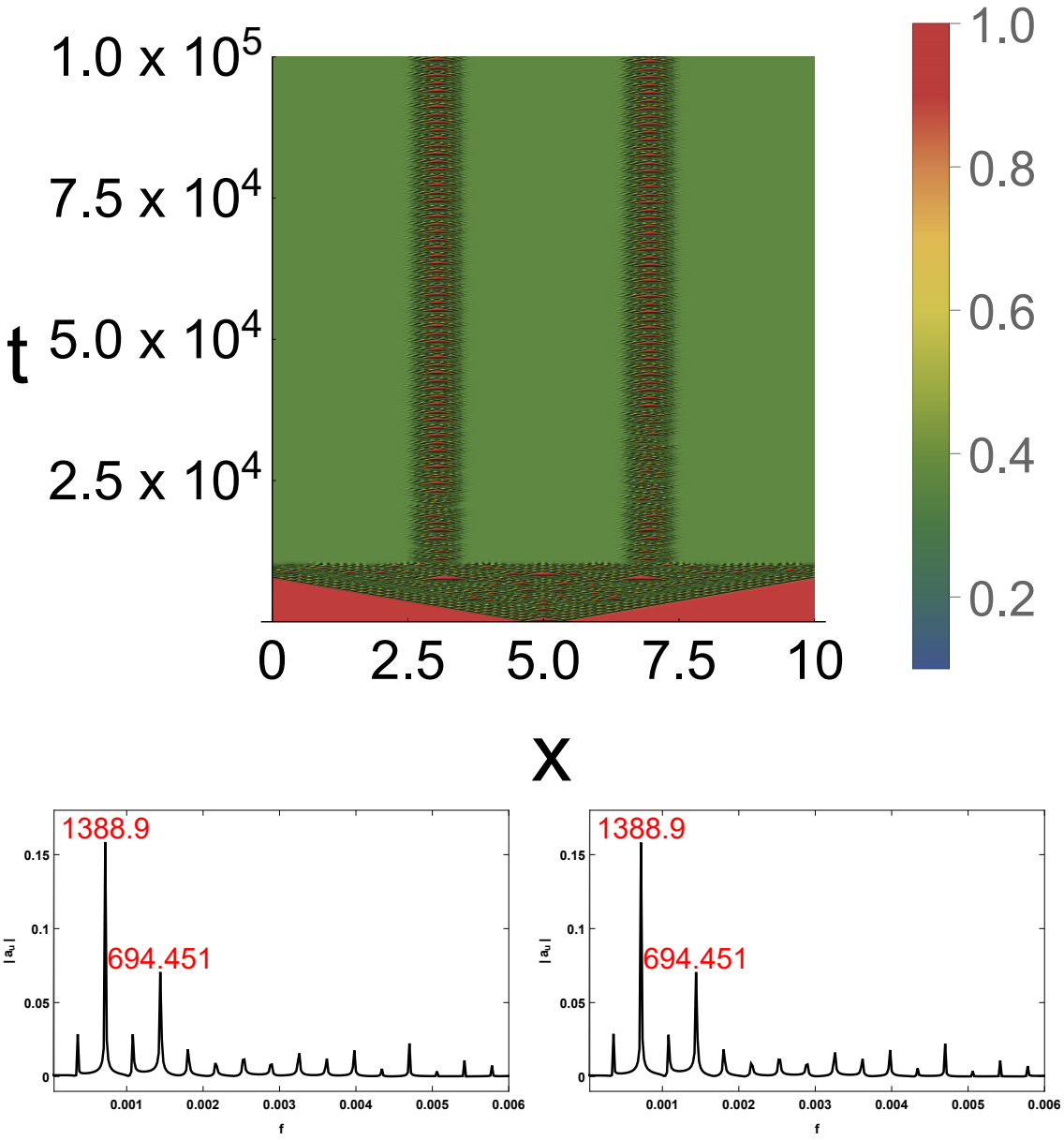

Figure 3.17: The right panel of Fig. 3.16 is explored for long times. A negative time-delayed feedback perturbation of strength $K = -0.03$ is applied to the system at $t = 10,000$ for all regions excluding the two wells. Bottom left: Fourier transform data for the left well for starting time $t = 50,000$, ending time $t = 100,000$. Bottom right: Fourier transform data for the right well for starting time $t = 50,000$, ending time $t = 100,000$. The periodic structures are formed at different times due to their the different local configurations at the onset of the perturbation. The resulting periodic pattern and Fourier peaks are the same.

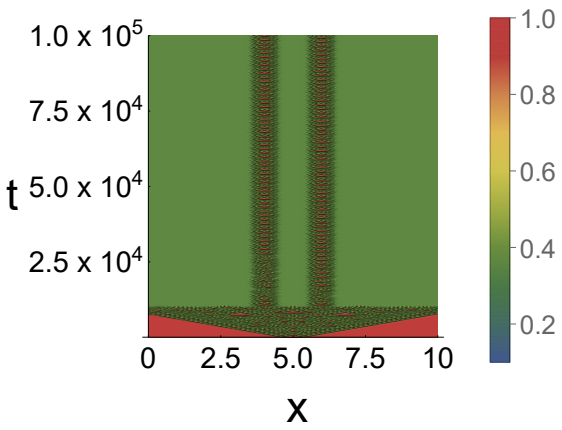

Figure 3.18: A negative time-delayed feedback perturbation is applied to the system at $t = 10,000$ for all regions excluding the two wells. The strength of the perturbation varies. The left half of the plot has $K = -0.029$, right half $K = -0.03$. Visually the results are difficult to distinguish from 3.17, so a more detailed analysis needs to be conducted, as shown in Fig. 3.19.

as time-delayed feedback control. The latter method has been applied in the past [12] to the one-dimensional Gray-Scott model as a whole in order to generate other global dynamics.

In this Chapter we have shown that applying time-delayed feedback to only part of the system may create novel spatially localized space-time pattern. We discussed two cases, one leading to perfect periodic pattern in the *unperturbed* part of the system, the other leading to imperfect oscillations in the perturbed region. The creation of these patterns turns out to be robust and is encountered for a broad range of system parameters. Our study reveals that the needed ingredient is the diffusion across the boundaries separating the perturbed and unperturbed regimes which yields a transition region, straddling the boundary, that is necessary to stabilize the spatially localized oscillations.

As shown in earlier work, in order to stabilize complex spatio-temporal dynamics near a subcritical Hopf bifurcation using time-delayed feedback control, the delay time τ has to be chosen as a multiple of the period of the periodic pattern to be stabilized [60, 61, 62]. This is very different from what we have discussed in this work as a local time-delayed perturbation stabilizes spatially localized patterns with periods orders of magnitude larger than the delay time. It is the interplay between time delay and boundaries separating perturbed and unperturbed regions that is the driving mechanism for the generation of these patterns with very long periods.

Our scheme is not restricted to the one-dimensional Gray-Scott model and similar results can be obtained in other situations as well as in other systems, including systems with truly chaotic behavior like the complex Ginzburg-Landau model [75] shown in chapter 4. Fig. 3.24 illustrates this for the two-dimensional Gray-Scott model where new patterns are

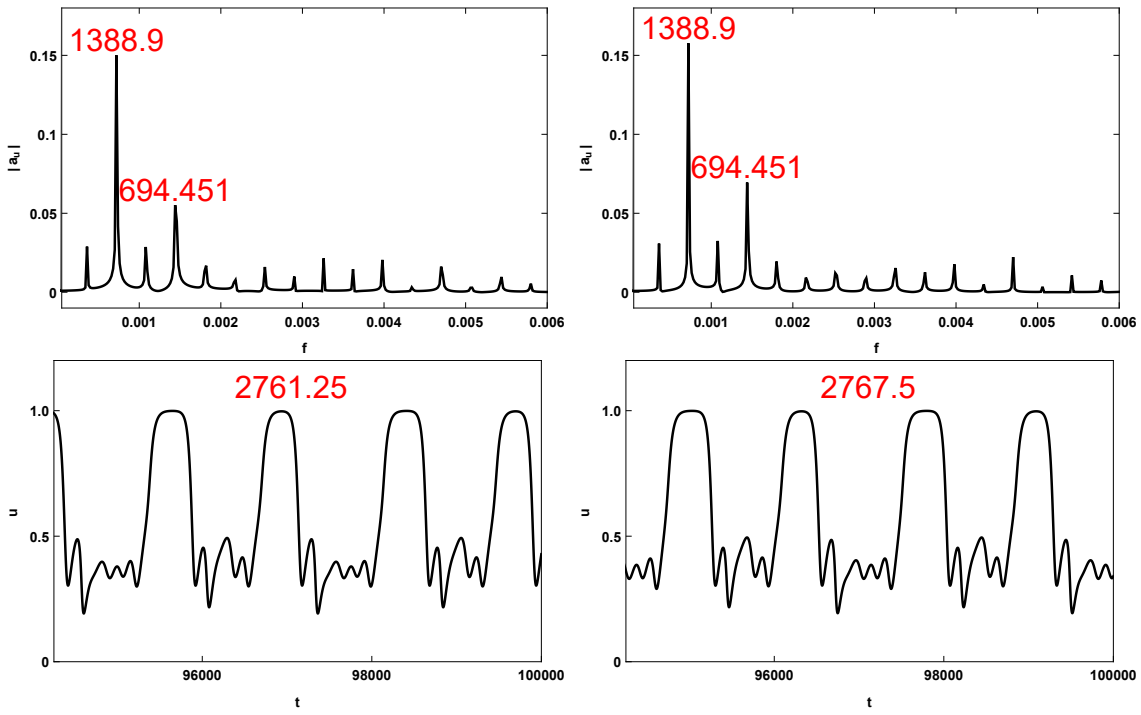

Figure 3.19: The top panel: Fourier transform data of the left and right well shown in Fig 3.18. In the top panels the two Fourier transforms are nearly identical. Some of the Fourier peaks are different which shifts the total period significantly. The bottom left panel shows the peak to peak separation at 2761.25. The bottom right panel shows the right well peak to peak separation at 2767.5. The right well shows the same peak to peak separation given for both identical wells in Fig. 3.17, clearly indicating that the peak to peak separation is tied to the control strength as shown in Fig. 3.6.

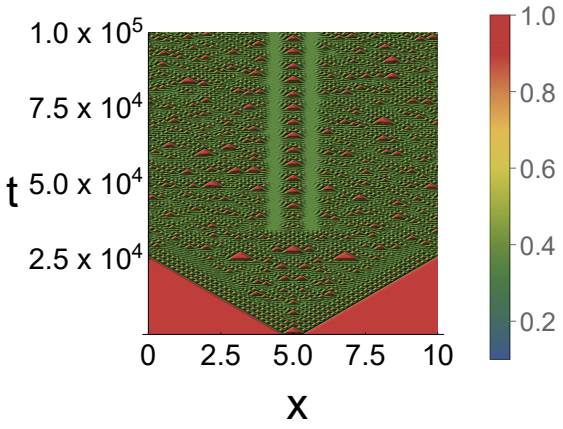

Figure 3.20: A negative time-delayed feedback perturbation is applied to the system at $t = 10,000$ for the two wells. The strength of the perturbation is $K = -0.03$. The center region has an induced periodic pattern formed with the same structure and period as Figures 3.3 and 3.17, having the same K value.

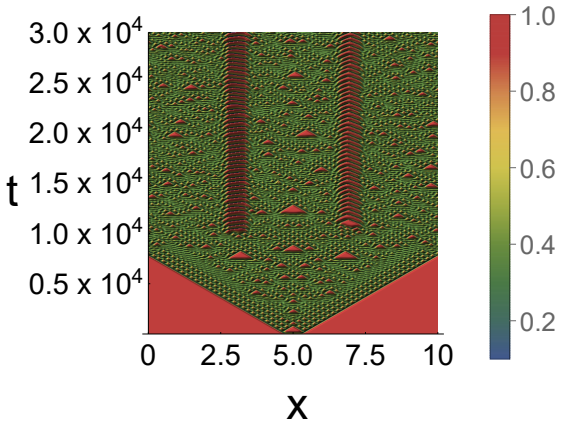

Figure 3.21: A positive time-delayed feedback perturbation is applied to the system at $t = 10,000$ for the two wells. The strength of the perturbation is different for the two regions. Left: $K = 0.05$, Right: $K = 0.025$.

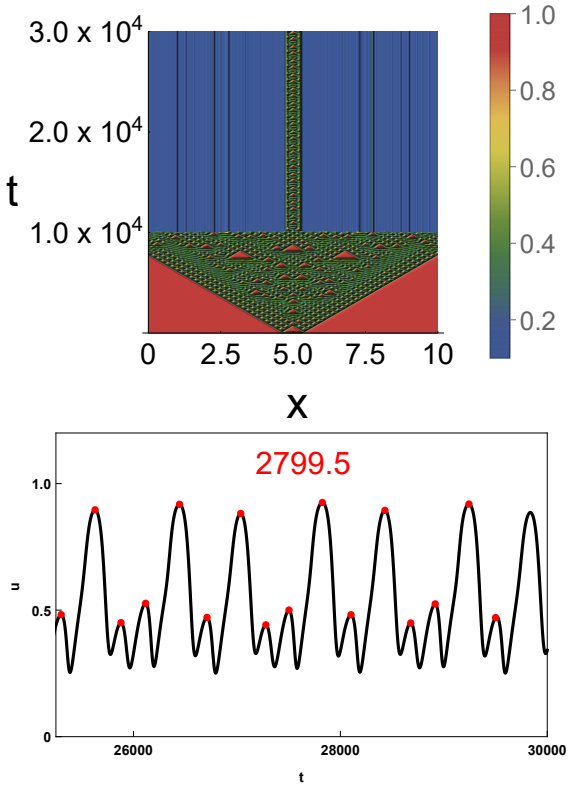

Figure 3.22: A positive past or set time feedback perturbation is applied to the system at $T = 10,000$. The strength of the perturbation is $K = 0.04$. Top: space-time plot, bottom: time series plot of center region. For up to $t = 30,000$ the system displays periodic-like patterns with a consistent period of $\sim 2,800$.

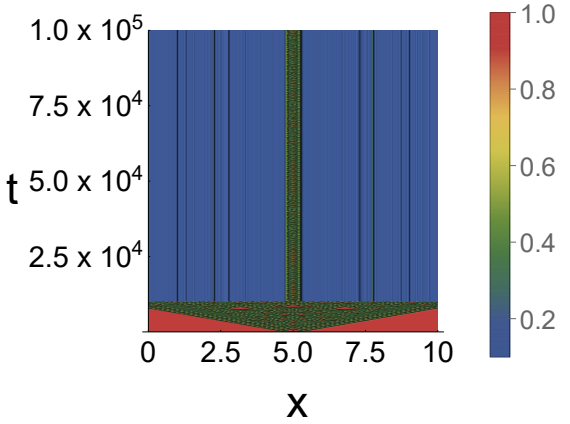

Figure 3.23: A positive past or set time feedback perturbation is applied to the system at $T = 10,000$. The strength of the perturbation $K = 0.04$. A long time plot of the same scenario as Fig. 3.22. The apparent perfect periodic pattern breaks down after long enough times.

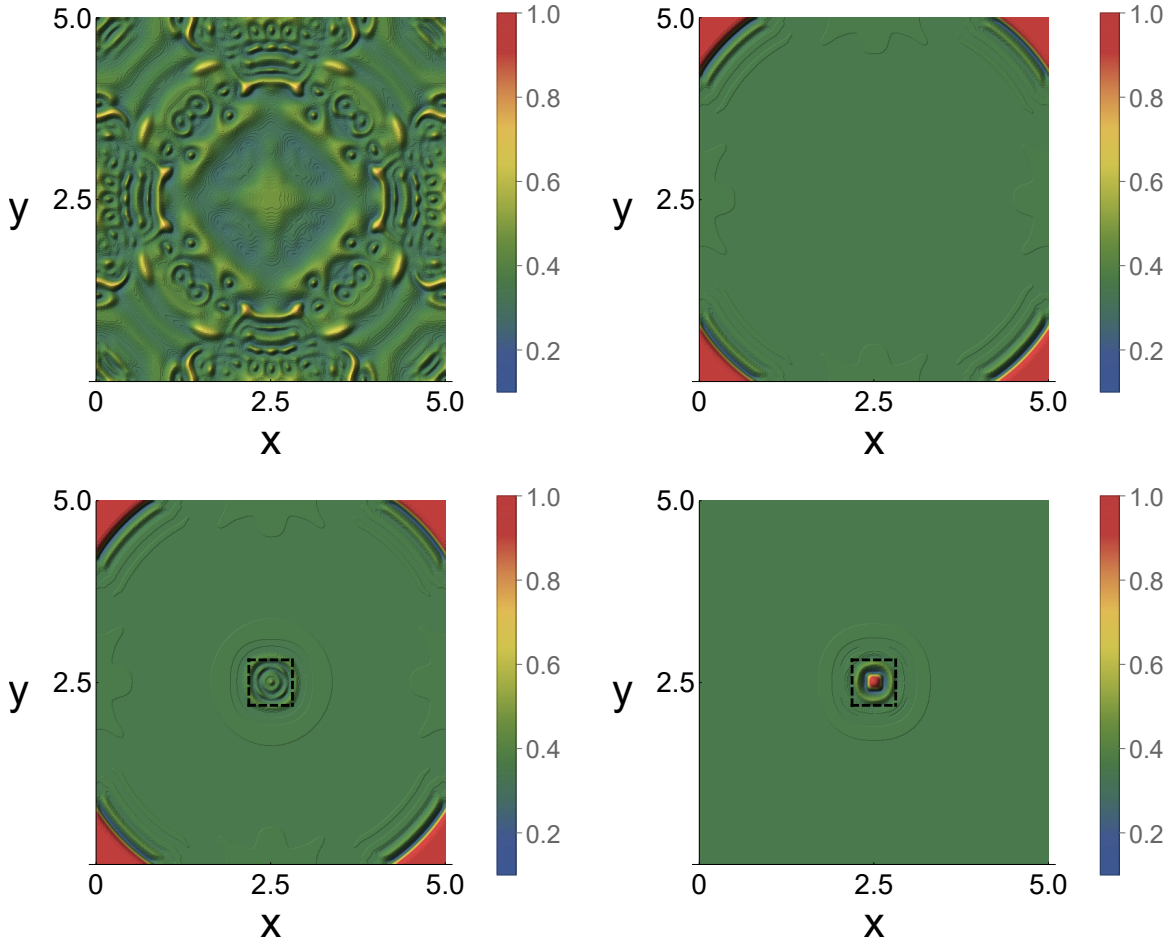

Figure 3.24: Some snapshots for the two-dimensional Gray-Scott model with periodic boundary conditions and an inhomogeneous initial state with $(u, v) = (0.5, 0.25)$ in a small square central region and $(u, v) = (1, 0)$ everywhere else. The common parameters are $A = 0.0238$ and $B = 0.05$, whereas the time increment is $h_t = 0.05$. (Top) The unperturbed system at $t = 5,000$ (left) and the system subjected to global control with $K = -0.25$ at $t = 5,000$ (right). (Bottom) The system at $t = 5,000$ (left) and at $t = 18,750$ (right) for the case where, with the exception of a small square region of size 0.3125×0.3125, indicated by dashed lines, the system is subjected to spatially localized perturbation with strength $K = -0.25$. Both for global and spatially localized perturbations, time-delayed feedback is switched on at $t = 250$.

locally created in the central region that is unperturbed.

Time-delayed feedback has been used experimentally to stabilize unstable periodic orbits of chaotic systems [76, 77, 78, 79, 80], but we are not aware of an attempt to do this in a spatially localized way as discussed in this work. As we have shown, new spatially localized pattern can be stabilized through spatially localized time-delayed feedback. We hope that our work paves the way for experimental implementations of this scheme and for the investigation of the resulting spatially localized patterns.

Chapter 4

Complex Ginzburg-Landau equation

4.1 Model and Method

The one-dimensional cubic complex Ginzburg-Landau equation (CGLe) is a nonlinear partial differential equation that reads as follows [29]:

$$\frac{\partial A_c}{\partial t} = A_c + (1 + i\alpha)\frac{\partial^2}{\partial x^2}A_c - (1 + i\beta)|A_c|^2 A_c, \tag{4.1}$$

where we have the complex field $A_c(x,t) = \rho(x,t)e^{i\phi(x,t)}$ with a modulus $\rho(x,t)$ and phase $\phi(x,t)$. We have α as the linear dispersion coefficient and β as the nonlinear dispersion coefficient.

All simulations presented in the following were performed with a Runge–Kutta 4th order scheme, with an 8th order diffusion term, with time step size $h_t = 0.01$, and the grid size $h_x = 0.25$. In order to apply integration schemes we can separate the complex field $A_c(x,t)$ into its real and imaginary components, $A_c(x,t) = A_r(x,t) + iA_i(x,t)$. We then can represent the equation as two coupled partial differential equations given as:

$$\frac{\partial}{\partial t}A_r = A_r + \frac{\partial^2}{\partial x^2}A_r - |A_c|^2 A_r - \alpha\frac{\partial^2}{\partial x^2}A_i + \beta|A_c|^2 A_i, \tag{4.2}$$

$$\frac{\partial}{\partial t}A_i = A_i + \frac{\partial^2}{\partial x^2}A_i - |A_c|^2 A_i + \alpha\frac{\partial^2}{\partial x^2}A_r - \beta|A_c|^2 A_r. \tag{4.3}$$

The system exhibits a variety of different dynamic regimes, but for this study we restrict our attention to regimes that exhibit spatio-temporal chaos. Throughout this article we will focus on defect turbulence, or amplitude turbulence (AT), phase turbulence (PT), and bi-chaos [30, 90]. One of the important features of this parameter space shown by Shraiman et al. and Boccaletti et al. is the Benjamin-Feir-Newel (BFN) line. This line gives a limit

for which stability of plane wave solutions can be analytically studied [30, 90]. Below this line the plane wave solutions admitted by Eq. 4.1 can be represented in the following form

$$A_q = \sqrt{1-q^2}e^{i(qx+\omega t)} \tag{4.4}$$

where q is the wave-number with bounds $-1 \leq q \leq 1$. The temporal frequency is given by $\omega = -\beta-(\alpha-\beta)q^2$. At the boundary of the Benjamin-Feir-Newel line, $\alpha\beta = -1$, the system transitions into phase turbulence. In our protocol of perturbing the system in a spatially localized way, the perturbation is applied to the real component of the system where Eq. 4.2 is replaced in some region $\mathcal{C}$ with the following form

$$\begin{aligned}\frac{\partial}{\partial t}A_r(\mathbf{x},t) &= A_r(\mathbf{x},t) + \frac{\partial^2}{\partial x^2}A_r(\mathbf{x},t) - |A_c|^2 A_r(\mathbf{x},t) - \alpha\frac{\partial^2}{\partial x^2}A_i(\mathbf{x},t) + \beta|A_c|^2 A_i(\mathbf{x},t) \\ &\quad + K\left(A_r(\mathbf{x},t-\tau) - A_r(\mathbf{x},t)\right).\end{aligned} \tag{4.5}$$

K is the perturbation strength which can be either positive or negative. τ is the time delay. Throughout this Chapter the numerical results presented use for the time delay $\tau = 0.25$. Several values of τ where investigated yielding the same resulting patterns.

The system has been subjected to different forms of control in previous works [29, 30]. These previous studies primarily dealt with determining the number of localized controllers needed for control. These controllers were found to be related to the number of independent spatial correlation lengths [30]. The majority of works on controlling the complex Ginzburg-Landau equation employ a form of control utilizing elements of plane wave solutions. The results from Chapter 3 on the Gray-Scott model show that simple global and localized feedback perturbations can form periodic structures. The methods and results in this Chapter will build upon the concept of spatially localized control.

4.2 Results

The three scenarios discussed in this chapter are for the one-dimensional complex Ginzburg-Landau equation (CGLe). They have in common that they evolve in time unperturbed until chaotic behavior is reached. Then a perturbation is applied in a specified region for the real component of the field in the form of time-delayed feedback, see Equation 4.5. For the general cases of having $K > 0$ the perturbed real component is able to effectively dictate the behavior of the system through the coupled nature of the real and imaginary components of the equation. Likewise, for the case with $K < 0$ the system responds to the perturbation along the real field component. It is noteworthy that the values of the real part of the amplitude and the amplitude magnitude increase greatly with increasing negative K values. The results presented in this chapter are for the $K > 0$ case. The perturbation onset time was systematically varied giving the same qualitative behavior of the generated patterns observed for all cases studied. The result robustness of the amplitude and phase turbulence regimes for vastly different onset times will be presented in their respective sections.

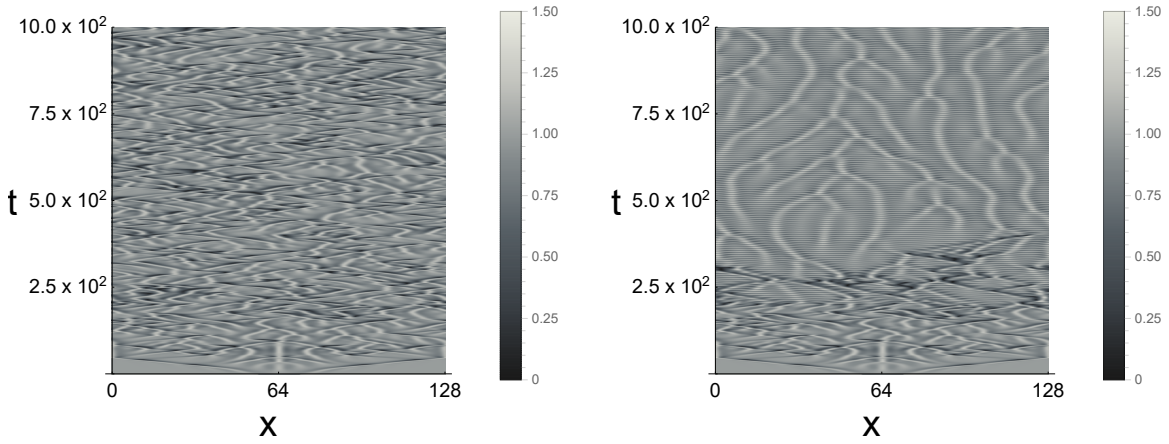

Figure 4.1: (Left) Amplitude turbulence (α=2.1, β=-1.2) with no control applied. (Right) Time-delayed feedback scheme applied globally across the whole system at $t = 200$ with the value of $K = 0.1$. The modulus $|A_c|$ is shown in the plot.

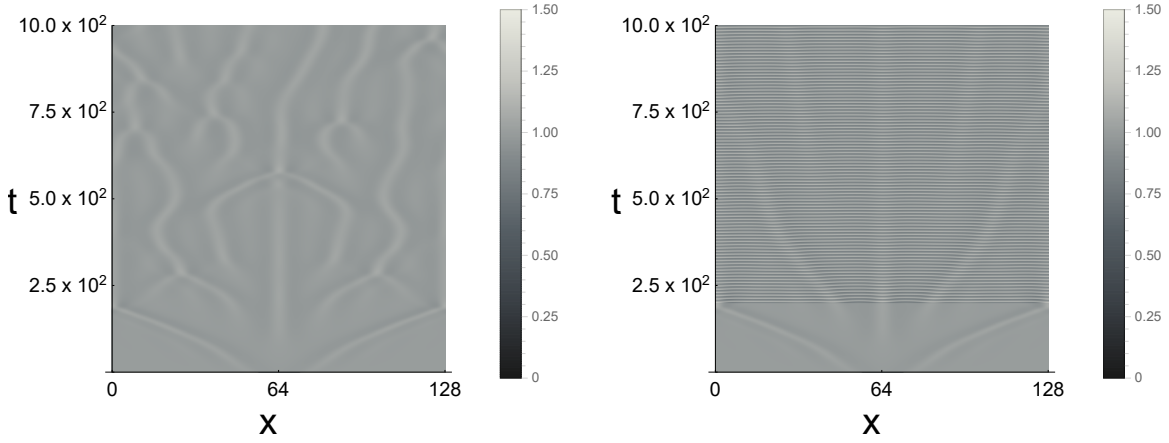

Figure 4.2: (Left) Phase Turbulence (α=2.1, β=-0.75) with no control applied. (Right) Time-delayed feedback scheme applied globally across the whole system at t=200 with the value of $K = 0.1$. The modulus $|A_c|$ is shown in the plot.

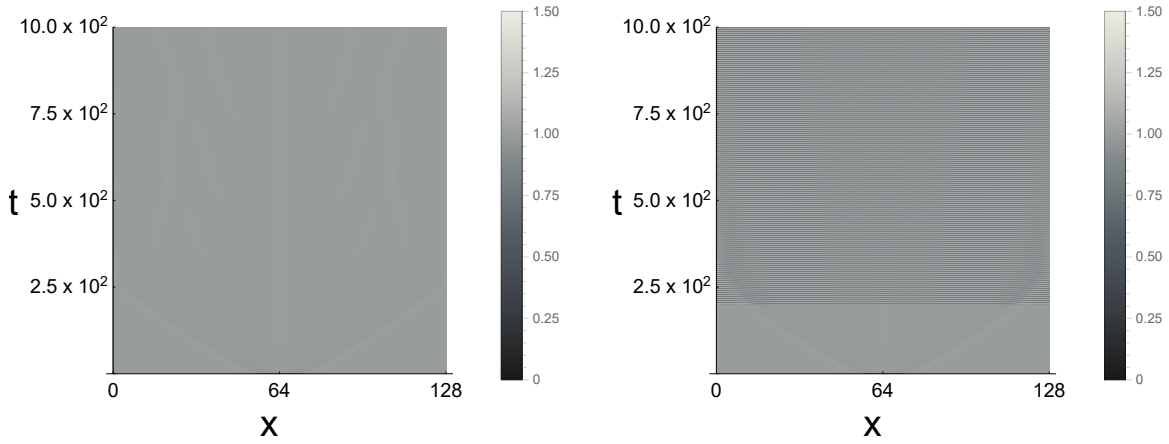

Figure 4.3: (Left) Bi-chaos (α=1, β=-1.2) form of chaos with no control applied. (Right) Time-delayed feedback scheme applied globally across the whole system at t=200 with the value of $K = 0.1$. The modulus $|A_c|$ is shown in the plot.

For a uniform global perturbation applied across the whole system we can see in Figs. 4.1, 4.2, and 4.3 that in all three regions the system will form repeating plane wave-like patterns. These patterns require appropriate choices of K and τ. Similar to the Gray-Scott model the general control strength applied is proportional to $K\tau$ within appropriate limits [12]. It is interesting and noteworthy to point out that, unlike for results obtained for uniformly placed local controllers, a globally applied spatially uniform time-delayed feedback perturbation shifts the systems into behaviors similar to that observed in regimes along the parameter space. This can be seen by comparing the right panel of Fig. 4.1 with the left panel of Fig. 4.2. The amplitude turbulence regime with a global perturbation has a plane wave-like result with elements of the wavy or branch like patterns of phase turbulence visible across the system. This result falls in line with the findings on the transitions between the chaotic regimes from other published works [74, 81]. The phase turbulence regime exhibits bands of unstable plane waves across the entire region space. The effects within bi-chaos form a series of uniform plane waves as shown in the right panel of Fig. 4.3.

4.2.1 Amplitude Turbulence

As shown in the right panel of Fig. 4.1, controlling defect chaos for the whole system results in plane wavelike patterns with irregular structures showing some resemblance of the patterns produced by unperturbed phase turbulence. The introduction of an unperturbed central region produces a directional stabilizing effect on the system which in turn produces regular periodic patterns in both the unperturbed center and perturbed outer region. Within the periodic pattern producing ranges of K we see that the peak-to-peak period increases for rising K values. We can see in Fig. 4.4 that the controlled region starts with an effect similar

to the global control with irregularly structured plane waves. The center unperturbed region interacts with the plane wave region at the boundary to produce regular periodic structures along space and time. The system experiences similar periodic patterns for certain continuous ranges of K and τ values shown in Figs. 4.4 and 4.5. The remarkable feature is that for different perturbation onset times and system run times, the system with identical K values forms similar periodic structures that have the same period. This feature is shown in Figs. 4.4, 4.5, 4.6, 4.7 and quantified in Figs. 4.8, 4.9 through the peak to peak pattern similarity and the same Fourier peaks across drastically different time scales. The Fourier analysis and time series results focus on the values of the real components at the center points, while noting that the same quantitative behavior is displayed for imaginary component, phase, and amplitude values as well. The slight differences between the periodic structures across different times scales indicate that there is a minor dependency on the perturbation onset time. These structures maintain the same period while having slight differences in the peak to peak patterns. These differences are due to the initial values of the real and imaginary part values at the onset of the perturbation. One way to interpret these results is that the perturbed region pushes the system to a plane wave producing regime. The system's chaotic nature is partially suppressed and the interaction between the perturbed and unperturbed regions creates a stabilizing effect on both regions. The time-delayed feedback then propagates this stabilizing effect across the entire system.

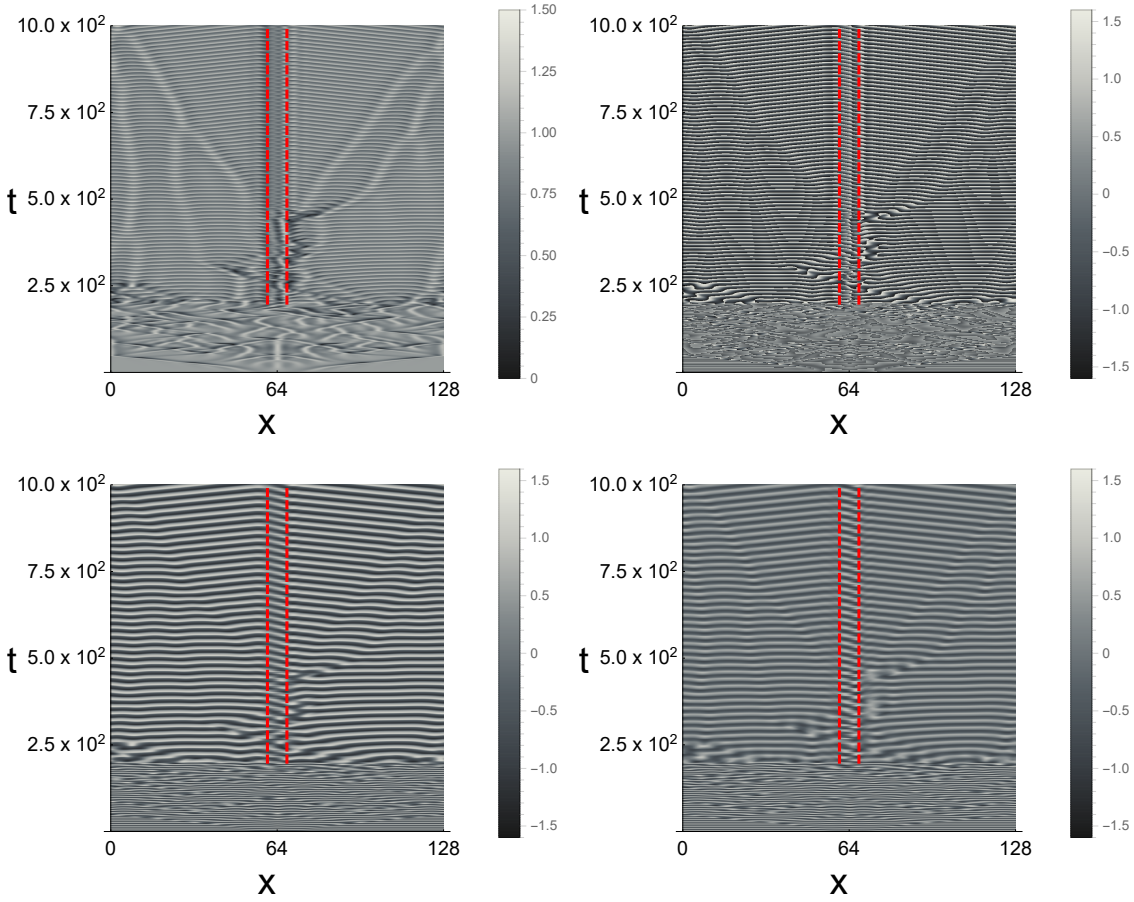

Figure 4.4: Using time-delayed feedback for the real component of the complex amplitude A_c everywhere in the system with the exception of the central region of width $W_{un} = 7.5$ for amplitude turbulence (α=2.1, β=-1.2). For this plot the strength $K = 0.25$ and delay time $\tau = 0.25$ were used and the perturbation started at $t = 200$. Top left: amplitude, top right: phase, bottom left: imaginary part, bottom right: real part.

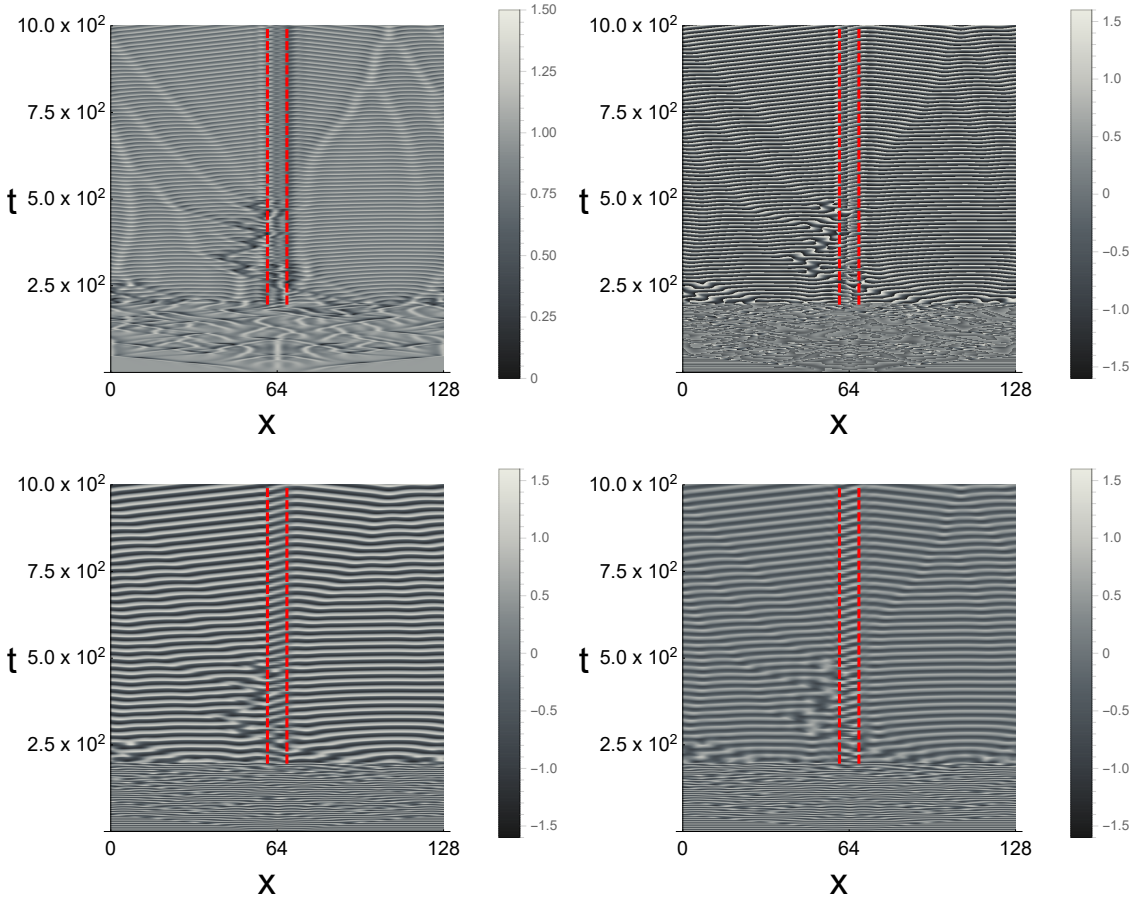

Figure 4.5: Using time-delayed feedback for the real component of the complex amplitude A_c everywhere in the system with the exception of the central region of width $W_{un} = 7.5$ for amplitude turbulence (α=2.1, β=-1.2). For this plot the strength $K = 0.27$ and delay time $\tau = 0.25$ were used and the perturbation started at $t = 200$. Top left: amplitude, top right: phase, bottom left: imaginary part, bottom right: real part.

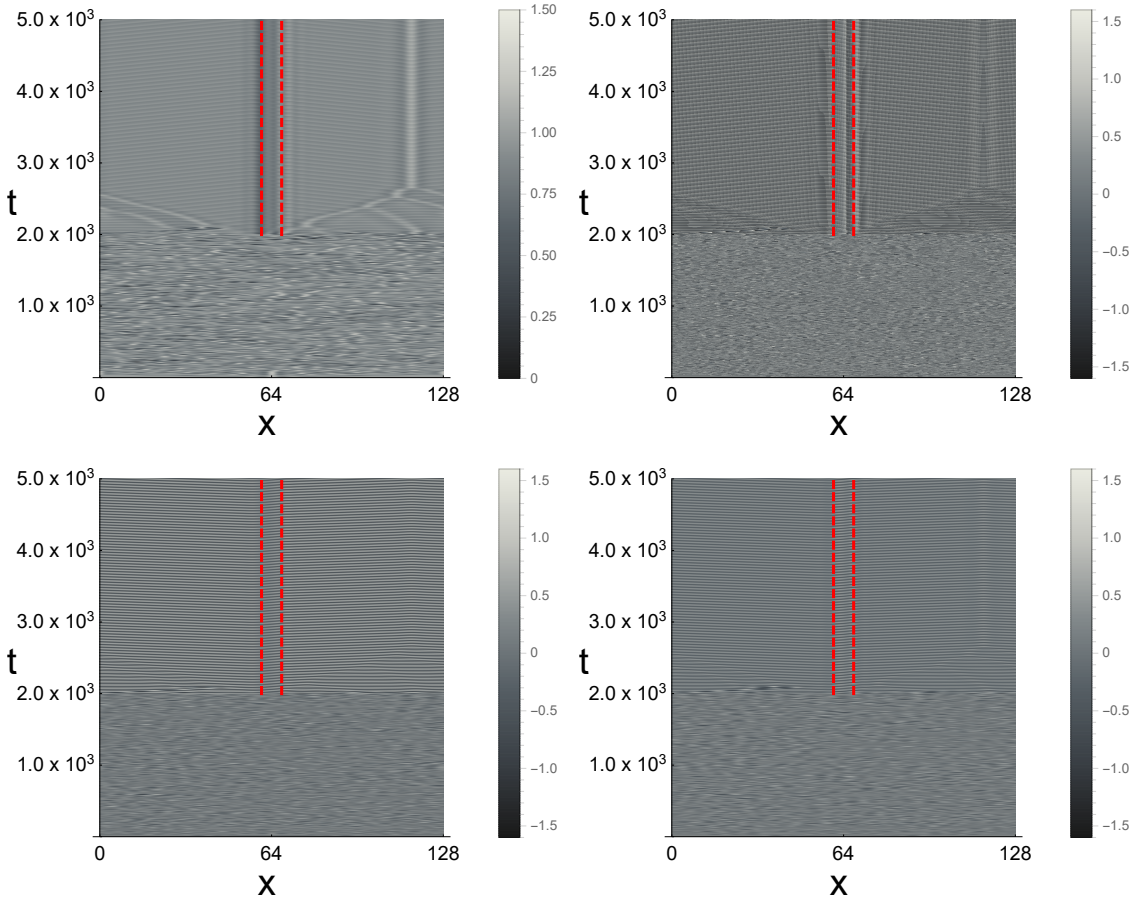

Figure 4.6: Using time-delayed feedback for the real component of the complex amplitude A_c everywhere in the system with the exception of the central region of width $W_{un} = 7.5$ for amplitude turbulence (α=2.1, β=-1.2). For this plot the strength $K = 0.25$ and delay time $\tau = 0.25$ were used and the perturbation started at $t = 2,000$. Top left: amplitude, top right: phase, bottom left: imaginary part, bottom right: real part.

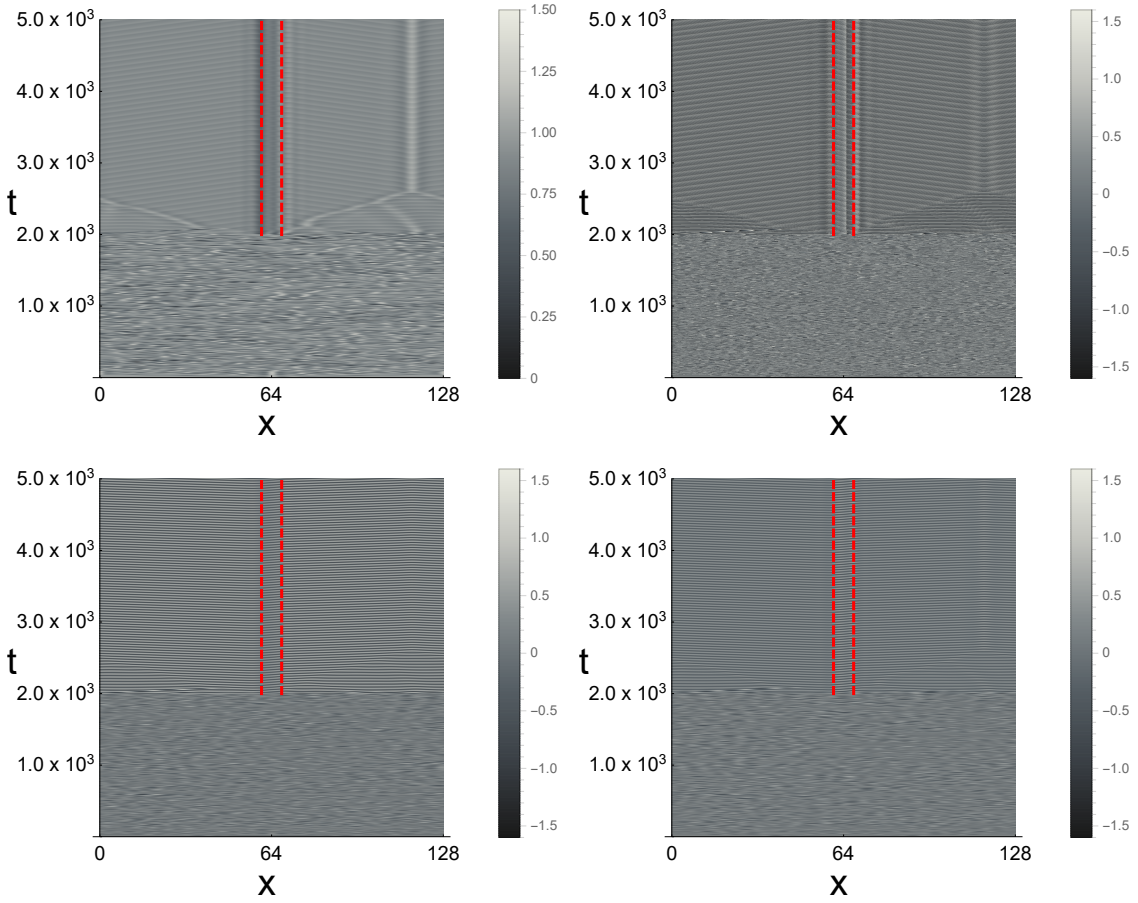

Figure 4.7: Using time-delayed feedback for the the real component of the complex amplitude A_c everywhere in the system with the exception of the central region of width $W_{un} = 7.5$ for amplitude turbulence (α=2.1, β=-1.2). For this plot the strength $K = 0.27$ and delay time $\tau = 0.25$ were used and the perturbation started at $t = 200$. Top left: amplitude, top right: phase, bottom left: imaginary part, bottom right: real part.

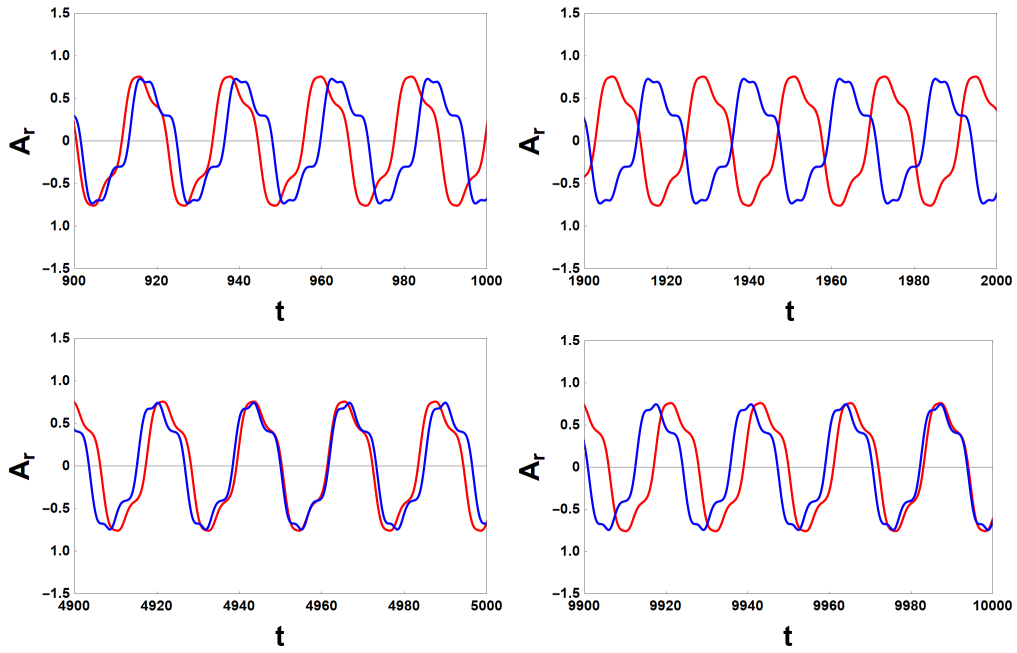

Figure 4.8: Time-dependent real component of the complex amplitude A_c in the middle of the unperturbed region for amplitude turbulence (α=2.1, β=-1.2) with $K = 0.25$ (red lines), $K = 0.27$ (blue lines), with the unperturbed region width $W_{un} = 7.5$. The top and bottom represent significantly different perturbation onset times. Top: $t = 200$, bottom: $t = 2,000$, see figures 4.4, 4.5 and figures 4.6, 4.7, respectively. For both values of K two different time intervals are shown, illustrating the consistency of the periodic patterns over time. When applying the time-delayed feedback outside of the middle region, the system maintains similar periodic pattern for continuous ranges of K values.

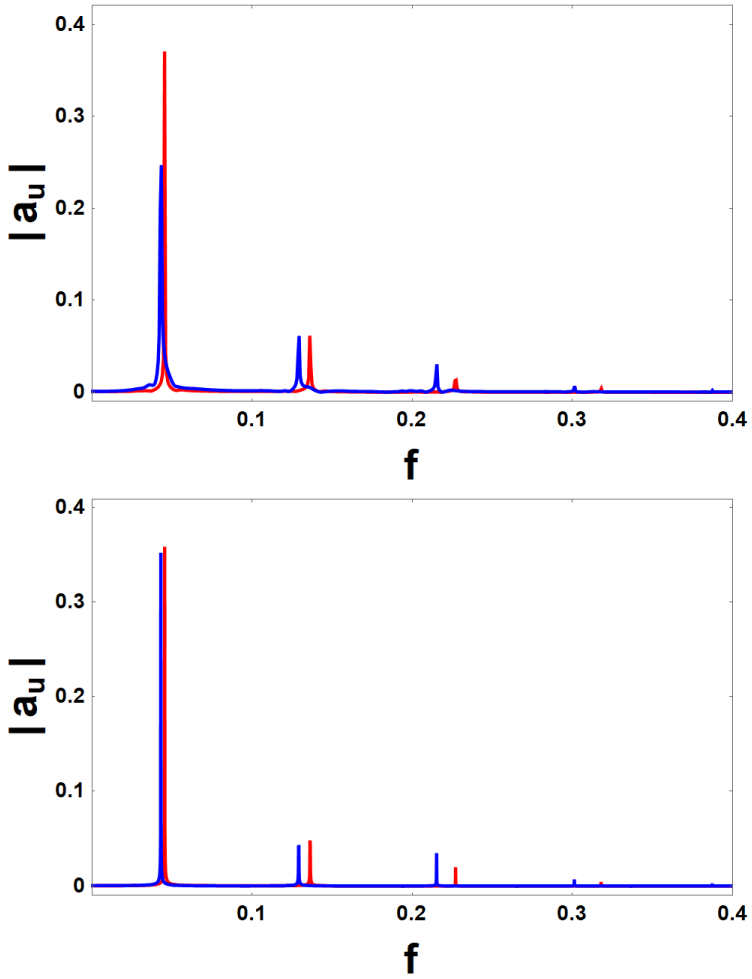

Figure 4.9: Frequency-dependent amplitude of the Fourier transform of the time-dependent real component of the complex amplitude A_c for $K = 0.25$ (red) and $K = 0.27$ (blue) for amplitude turbulence (α=2.1, β=-1.2) with unperturbed region width $W_{un} = 7.5$. Top: perturbation applied at $t = 200$, bottom: perturbation applied at $t = 2,000$. The system period depends on the strength K of the perturbation.

4.2.2 Phase Turbulence

As shown in the right panel of Fig. 4.2, controlling phase turbulence with time-delayed feedback across the whole system results in plane wave patterns. The introduction of unperturbed regions produces a robust stabilizing effect on the system which in turn produces regular periodic patterns. These patterns form in both the unperturbed center and perturbed outer region. The patterns produced by localized perturbation are shown in Fig. 4.10. Unlike amplitude turbulence, phase turbulence exhibits pattern formation across broader ranges of K values and window widths with up to over half of the total lattice size. The larger the uncontrolled region is, the higher the control strength must be for the surrounding controlled region. The transition to periodic patterns occurs much earlier after perturbation onset than within the amplitude turbulence regime. This is shown in Figs. 4.10, 4.11, 4.12, 4.13. The periods of the repeat structures formed within the center region increases for increasing value of K, as shown in Figs. 4.14 and 4.15. Much like for the amplitude turbulence with different perturbation onset times and system run times, the systems in the phase turbulence regime with identical K values and different onset times forms similar periodic structures with the exact same period. This feature is quantified in Figs. 4.14, 4.15 through the peak to peak pattern similarity and the same Fourier peaks. This further indicates that periodic pattern formation from spatially localized time delay is a consistent method when appropriately applied to chaotic systems.

4.2.3 Bi-chaos

As shown in the right panel of Fig. 4.3, controlling bi-chaos for the whole system results in the formation of plane waves much like for the phase turbulence regime. The system with a unperturbed region exhibits a few behaviors similar to those in other regimes. Like amplitude turbulence, bi-chaos has a limited range of perturbation region widths that produce regular periodic patterns. After the application of time-delayed perturbations short lived plane wave pattern form along the outer edges. These plane wave patterns interact with the center region over larger time scales changing the periodic patterns observed within the center. We see a stark change in the center pattern at $t > 3,000$ shown in Figs. 4.18 and 4.19. Shown in Figs. 4.16, 4.17, 4.18 and 4.19, the system undergoes this transition across longer times. The top panels in Figs. 4.20 and 4.21 show well defined periodic structures for low perturbation onset times, with limited duration. The bottom panels in Figs. 4.20 and 4.21 show that the periodic behavior changes to imperfect repeating patterns. When comparing Figs. 4.16 and 4.17 with Figs. 4.18 and 4.19, we see a clear transition within the unperturbed center for large times. This shows an interesting feature of bi-chaos, namely that the perturbation induced early time repeating patterns are not consistent for long times. It additionally shows that the time for the long term repeat behavior to form can vary depending on the perturbation onset times.

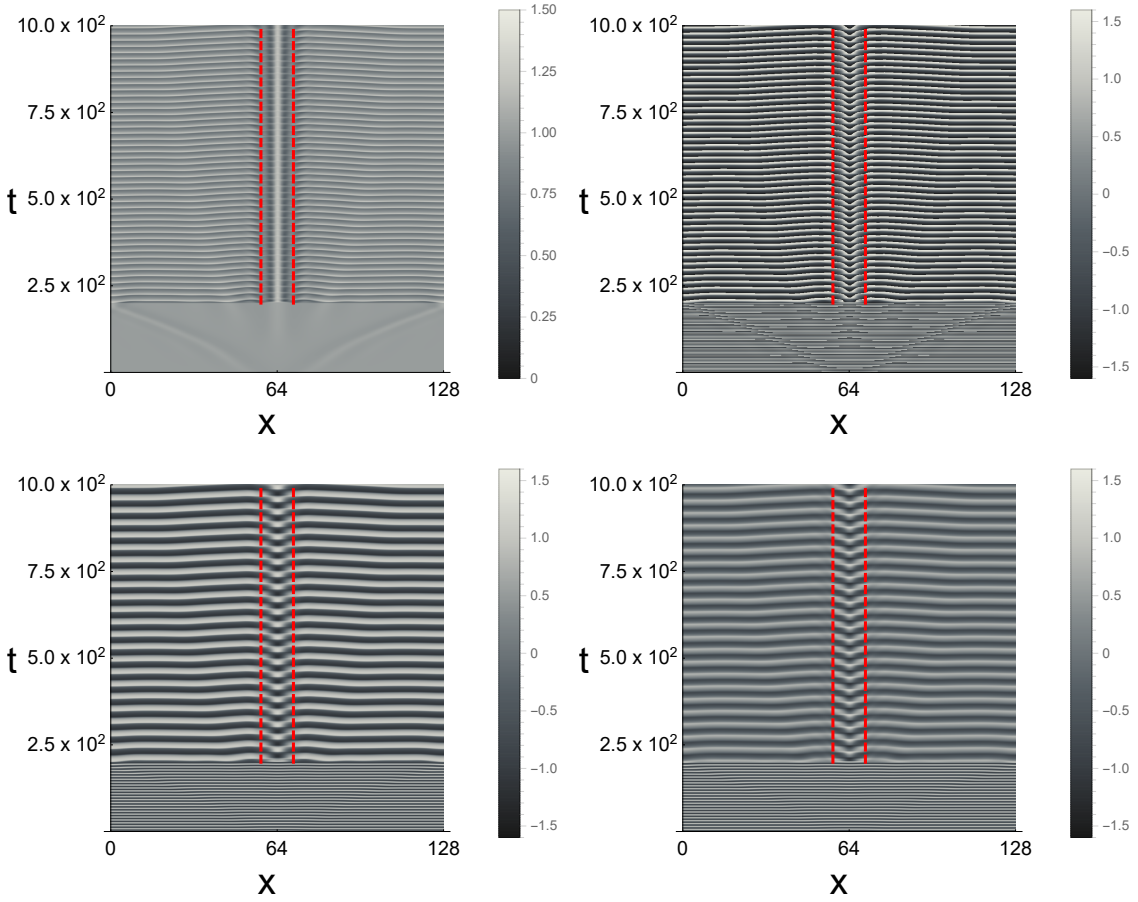

Figure 4.10: Using time-delayed feedback for the real component of the complex amplitude A_c everywhere in the system with the exception of the central region of width $W_{un} = 12.5$ for phase turbulence (α=2.1, β=-0.75). For this plot the strength $K = 0.3$ and delay time $\tau = 0.25$ were used and the perturbation started at $t = 200$. Top left: amplitude, top right: phase, bottom left: imaginary part, bottom right: real part.

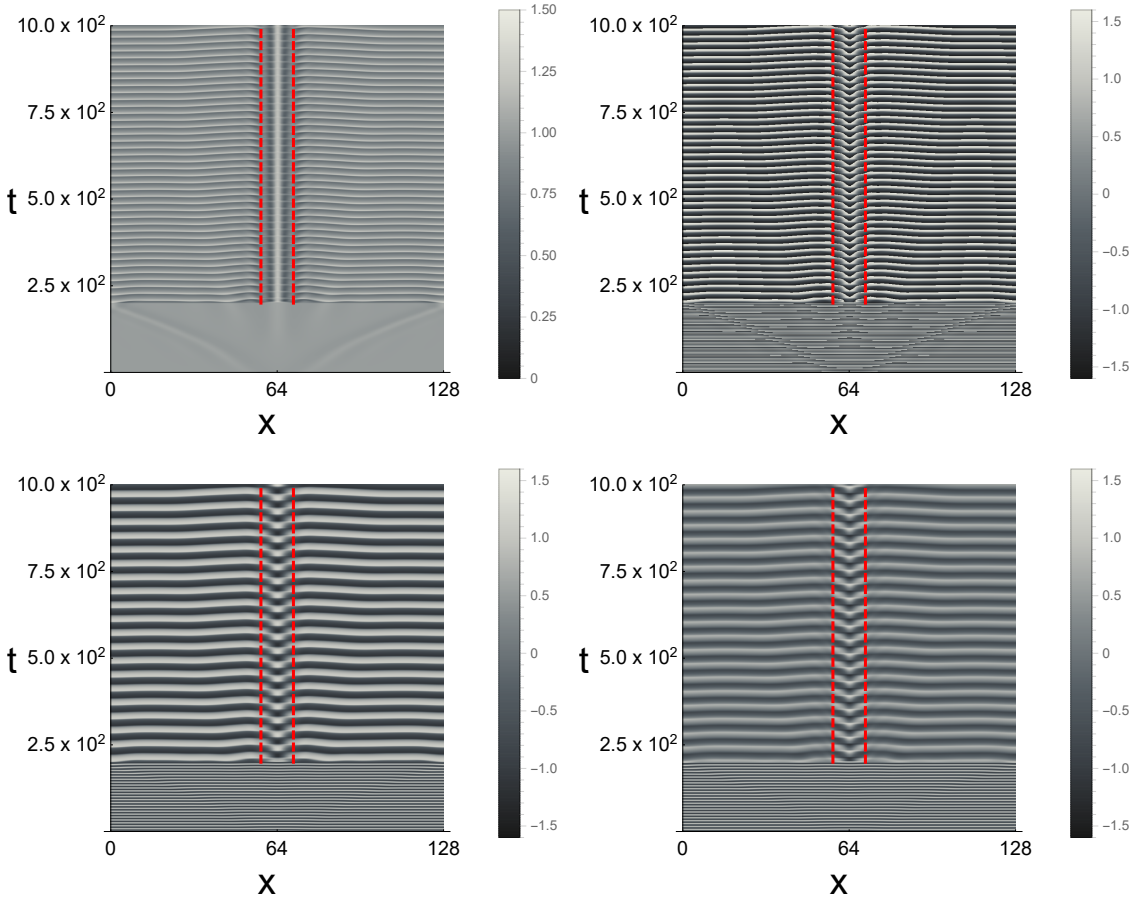

Figure 4.11: Using time-delayed feedback for the real component of the complex amplitude A_c everywhere in the system with the exception of the central region of width $W_{un} = 12.5$ for phase turbulence (α=2.1, β=-0.75). For this plot the strength $K = 0.35$ and delay time $\tau = 0.25$ were used and the perturbation started at $t = 200$. Top left: amplitude, top right: phase, bottom left: imaginary part, bottom right: real part.

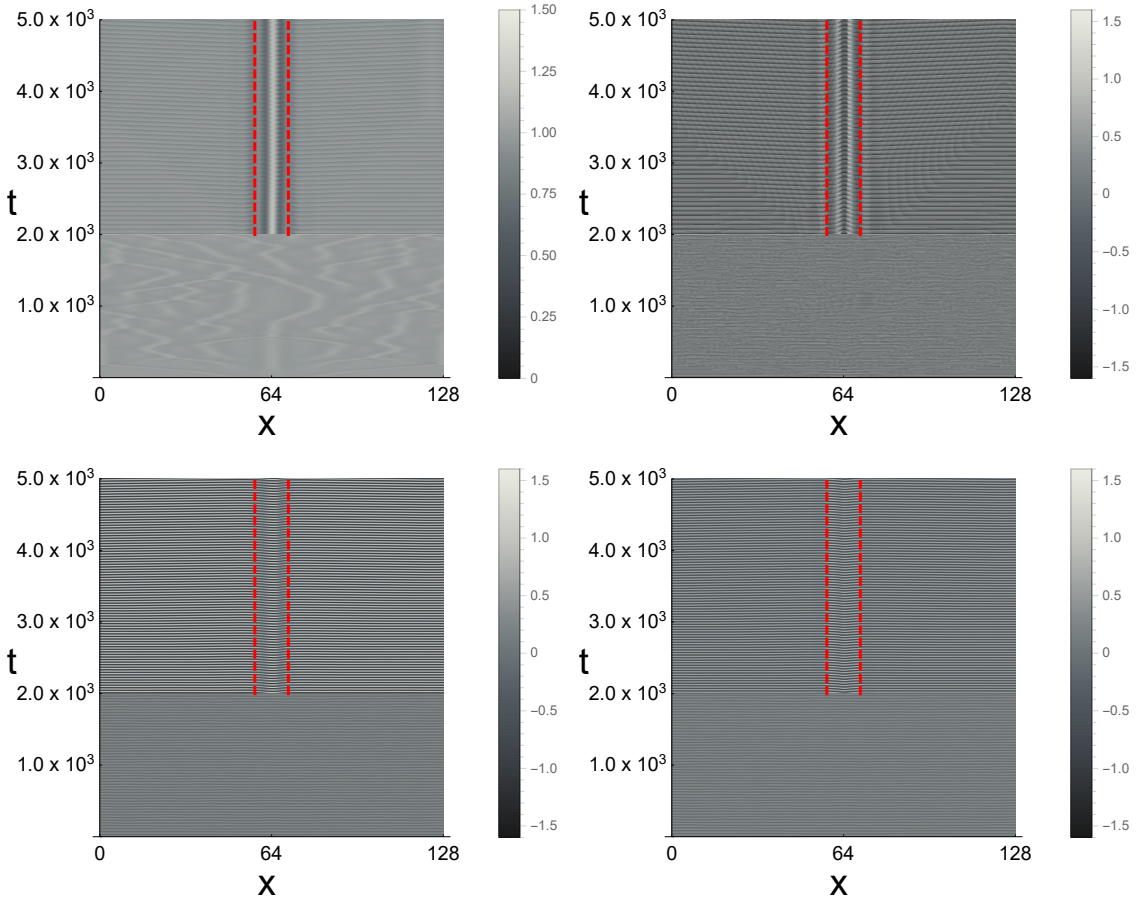

Figure 4.12: Using time-delayed feedback for the real component of the complex amplitude A_c everywhere in the system with the exception of the central region of width $W_{un} = 12.5$ for phase turbulence (α=2.1,β=-0.75). For this plot the strength $K = 0.3$ and delay time $\tau = 0.25$ were used and the perturbation started at $t = 2,000$. Top left: amplitude, top right: phase, bottom left: imaginary part, bottom right: real part.

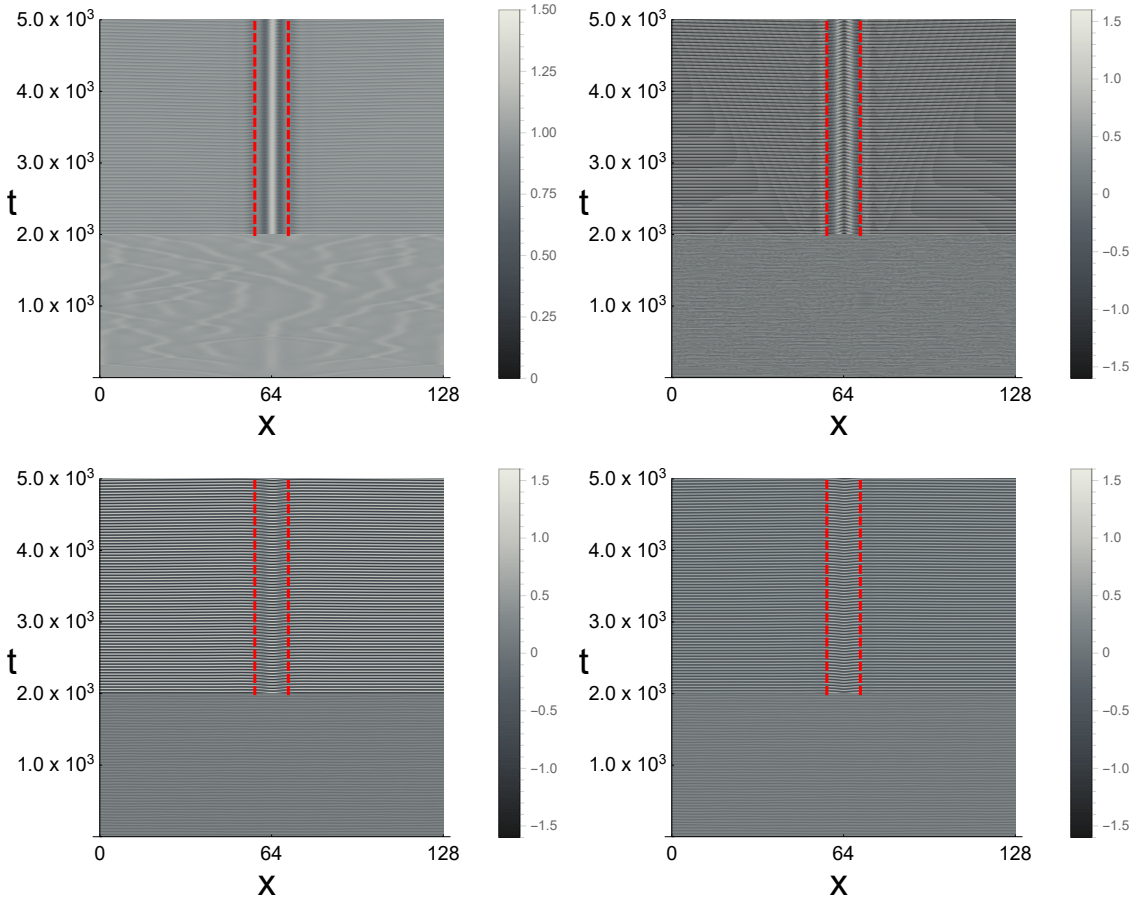

Figure 4.13: Using time-delayed feedback for the real component of the complex amplitude A_c everywhere in the system with the exception of the central region of width $W_{un} = 12.5$ for phase turbulence (α=2.1, β=-0.75). For this plot the strength $K = 0.35$ and delay time $\tau = 0.25$ were used and the perturbation started at $t = 2,000$. Top left: amplitude, top right: phase, bottom left: imaginary part, bottom right: real part.

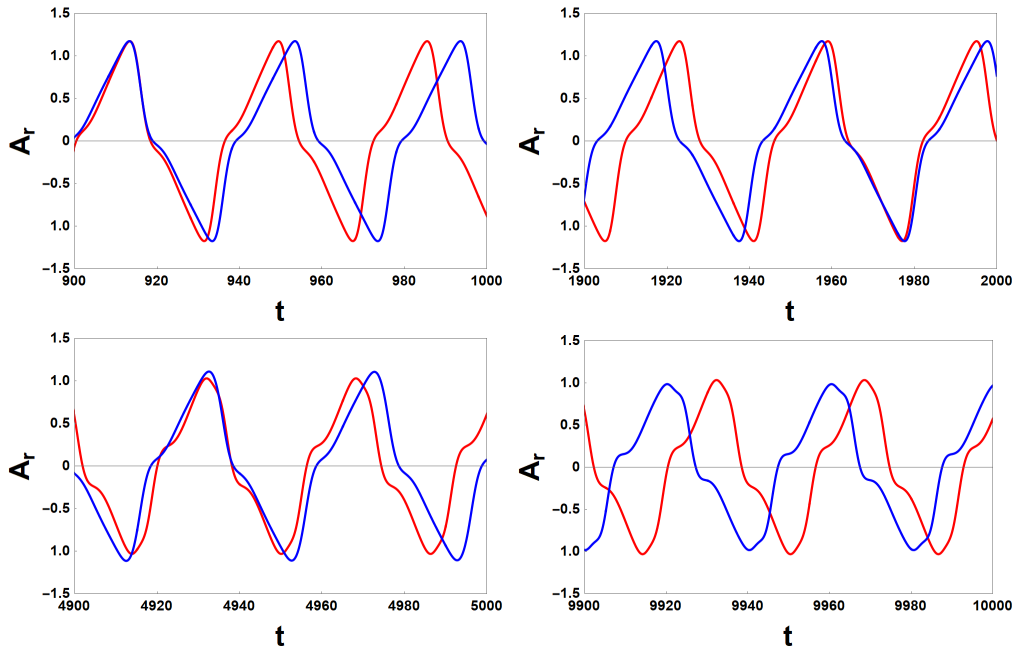

Figure 4.14: Time-dependent real component of the complex amplitude A_c in the middle of the unperturbed region for phase turbulence (α=2.1, β=-0.75) with $K = 0.3$ (red lines), $K = 0.35$ (blue lines), with the unperturbed region width $W_{un} = 12.5$. The top and bottom represent significantly different perturbation onset times. Top: $t = 200$, bottom: $t = 2,000$, see figures 4.10, 4.11 and figures 4.12, 4.13, respectively. For both values of K two different time intervals are shown, illustrating the consistency of the periodic patterns over time. When applying the time-delayed feedback outside of the middle region, the system maintains similar periodic pattern for continuous ranges of K values.

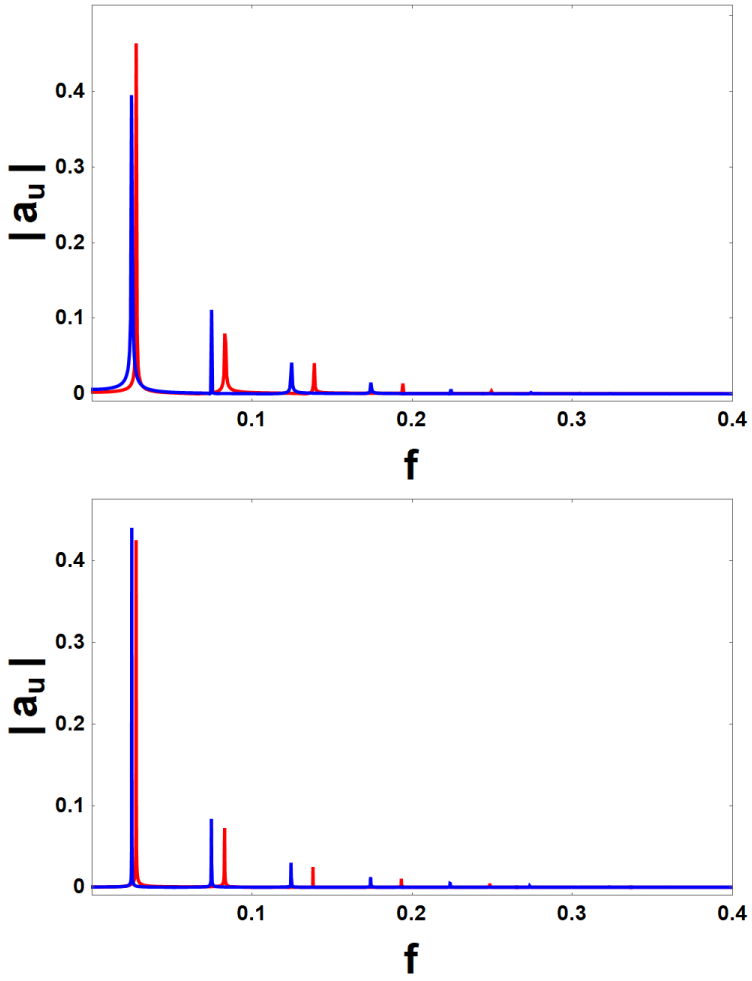

Figure 4.15: Frequency-dependent amplitude of the Fourier transform of the time-dependent real component of the complex amplitude A_c for $K = 0.3$ (red) and $K = 0.35$ (blue) for phase turbulence (α=2.1, β=-0.75) with unperturbed region width $W_{un} = 12.5$. Top: perturbation applied at $t = 200$, bottom: perturbation applied at $t = 2,000$. The system period depends on the strength K of the perturbation.

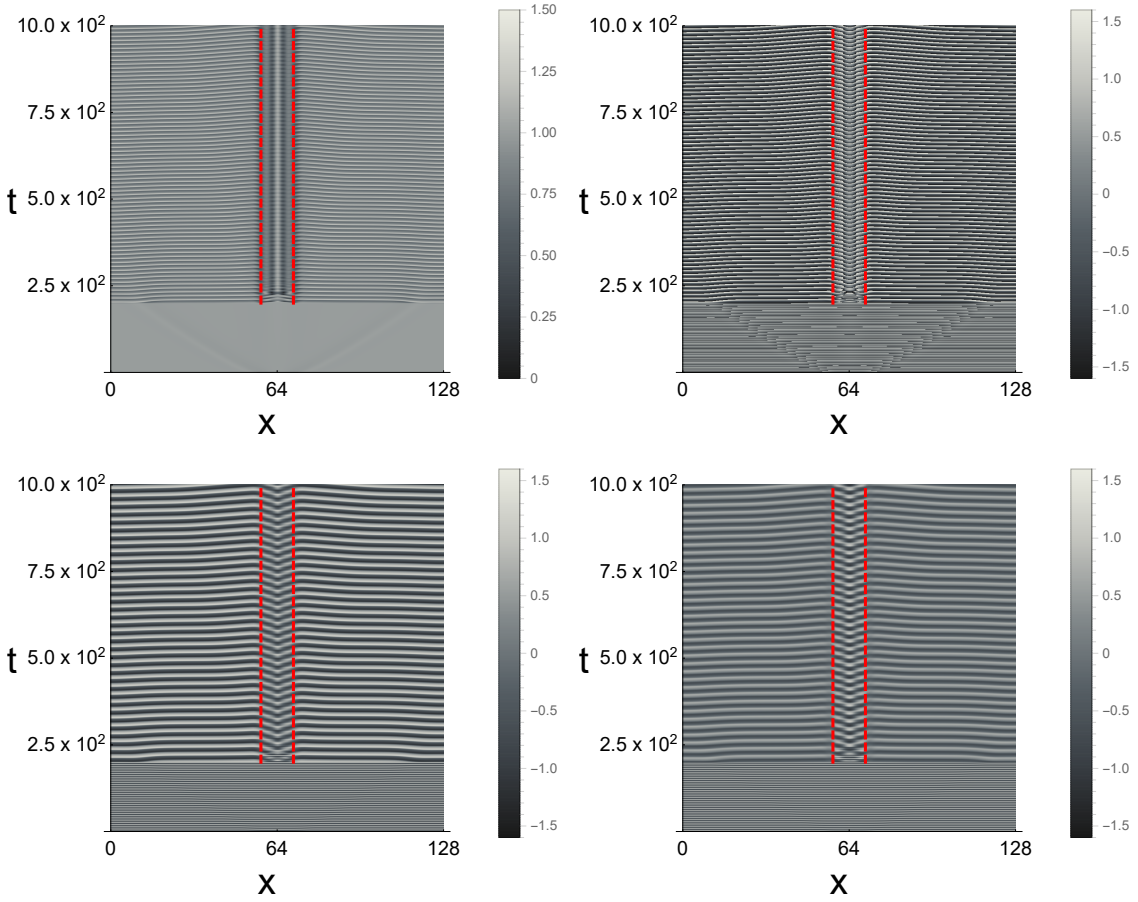

Figure 4.16: Using time-delayed feedback for the real component of the complex amplitude A_c everywhere in the system with the exception of the central region of width $W_{un} = 12.5$ for bi-chaos (α=1, β=-1.2). For this plot the strength $K = 0.3$ and delay time $\tau = 0.25$ were used and the perturbation started at $t = 200$. Top left: amplitude, top right: phase, bottom left: imaginary part, bottom right: real part.

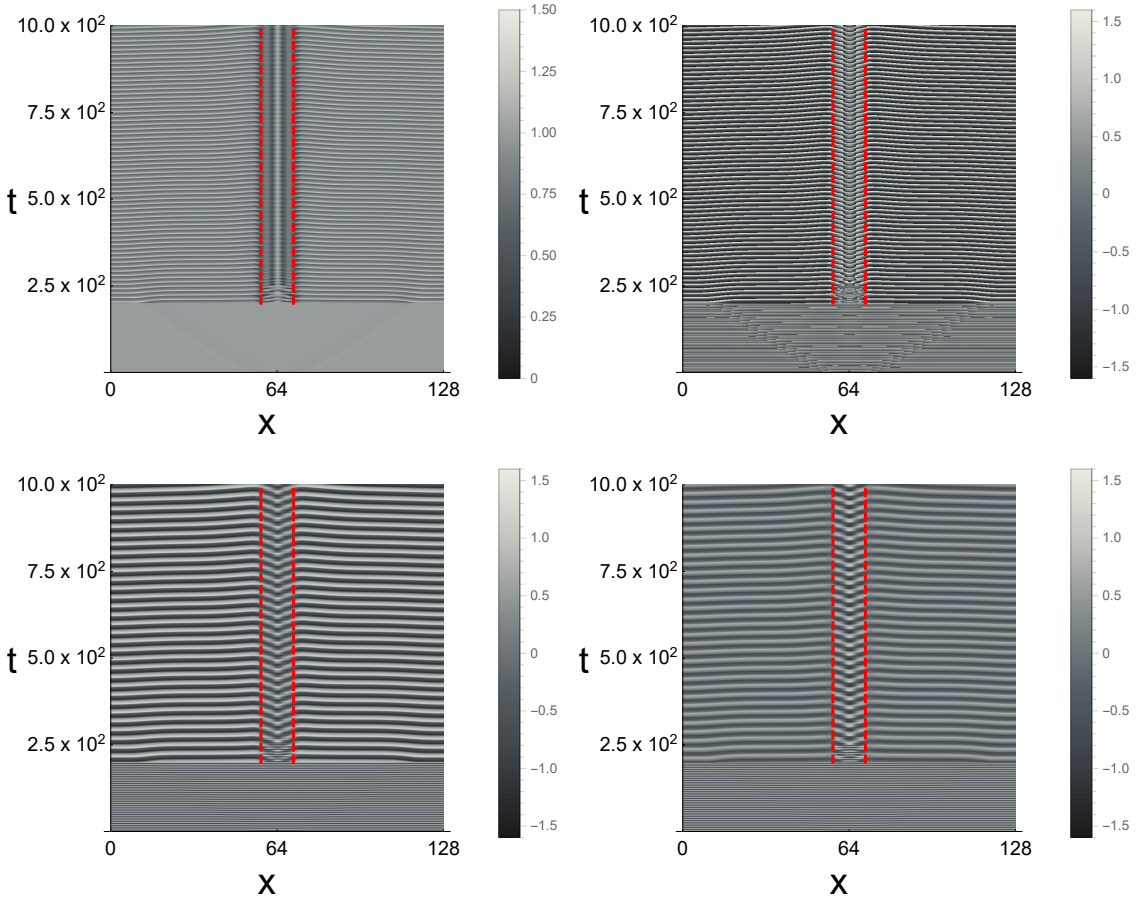

Figure 4.17: Using time-delayed feedback for the real component of the complex amplitude A_c everywhere in the system with the exception of the central region of width $W_{un} = 12.5$ for bi-chaos (α=1, β=-1.2). For this plot the strength $K = 0.35$ and delay time $\tau = 0.25$ were used and the perturbation started at $t = 200$. Top left: amplitude, top right: phase, bottom left: imaginary part, bottom right: real part.

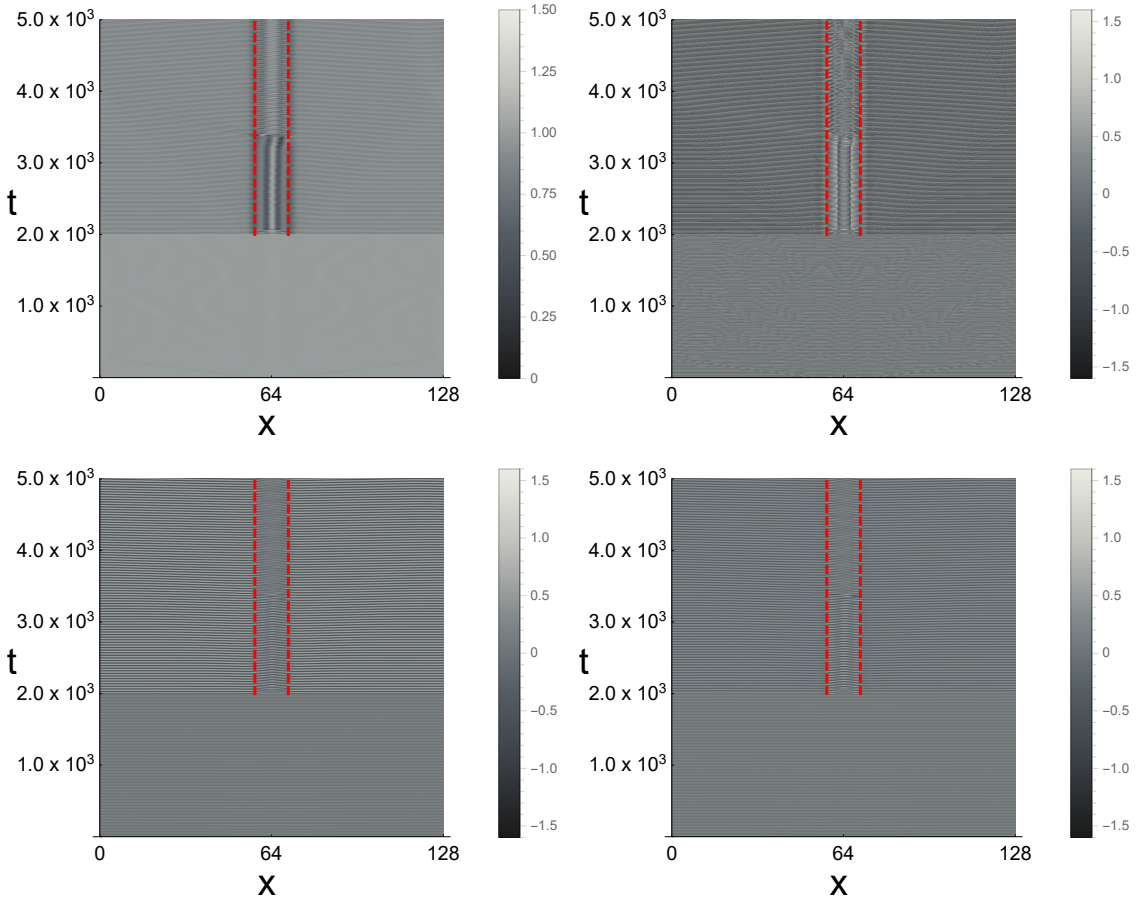

Figure 4.18: Using time-delayed feedback for the real component of the complex amplitude A_c everywhere in the system with the exception of the central region of width $W_{un} = 12.5$ for bi-chaos (α=1, β=-1.2). For this plot the strength $K = 0.3$ and delay time $\tau = 0.25$ were used and the perturbation started at $t = 2,000$. Top left: amplitude, top right: phase, bottom left: imaginary part, bottom right: real part.

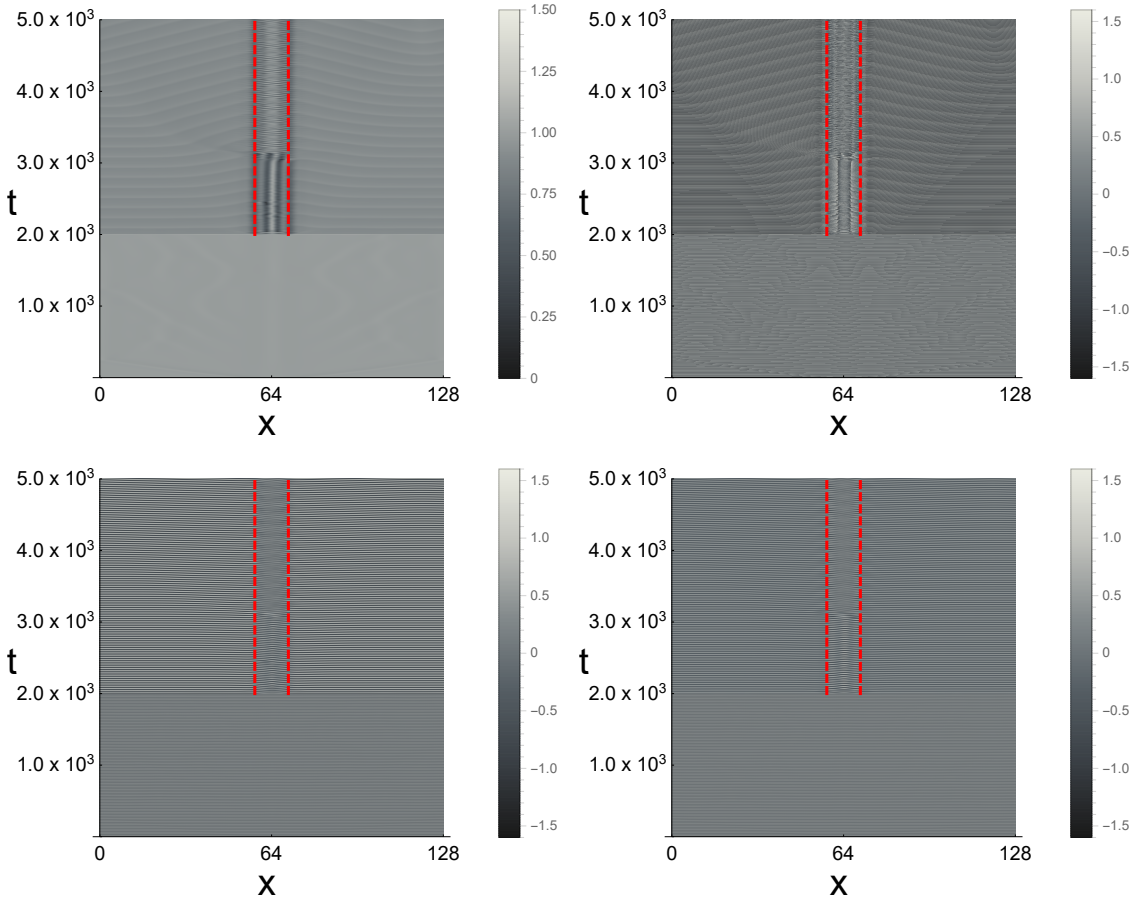

Figure 4.19: Using time-delayed feedback for the real component of the complex amplitude A_c everywhere in the system with the exception of the central region of width $W_{un} = 12.5$ for bi-chaos, (α=1, β=-1.2). For this plot the strength $K = 0.35$ and delay time $\tau = 0.25$ were used and the perturbation started at $t = 2,000$. Top left: amplitude, top right: phase, bottom left: imaginary part, bottom right: real part.

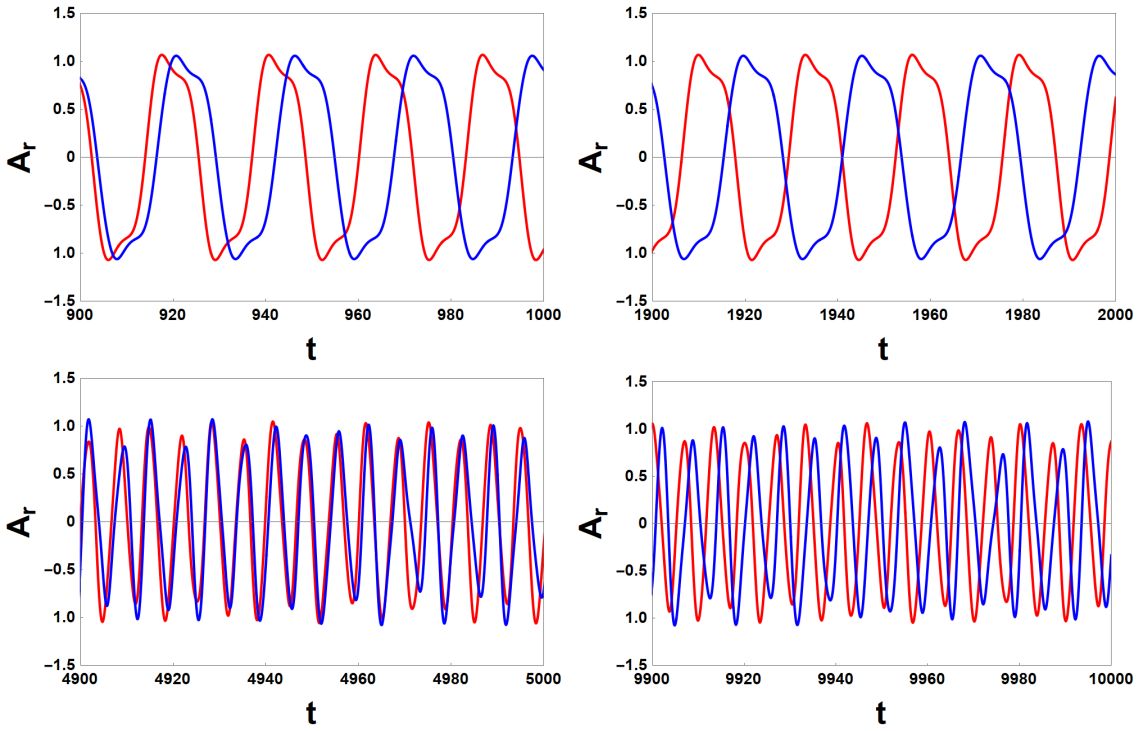

Figure 4.20: Time-dependent real component of the complex amplitude A_c in the middle of the unperturbed region for bi-chaos (α=1, β=-1.2) with $K = 0.3$ (red lines), $K = 0.35$ (blue lines), with the unperturbed region width $W_{un} = 12.5$. The top and bottom represent significantly different perturbation onset times. Top: $t = 200$, bottom: $t = 2,000$, see figures, 4.16, 4.17 and figures: 4.18, 4.19, respectively. For both values of K two different time intervals are shown. In stark contract to the results obtained for the amplitude and phase turbulence, the system shows significantly different periodic structures for different onset times and time length scales. When applying the time-delayed feedback outside of the middle region, the system maintains similar periodic pattern for continuous ranges of K values.

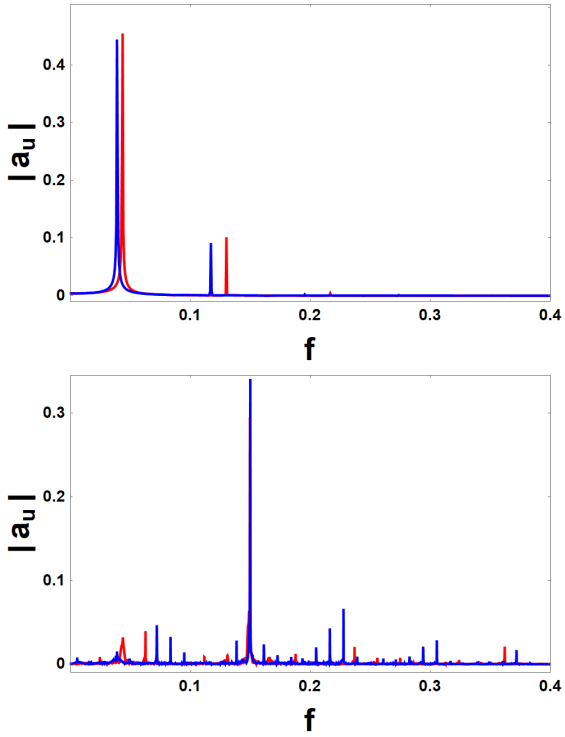

Figure 4.21: Frequency-dependent amplitude of the Fourier transform of the time-dependent real component of the complex amplitude A_c for $K = 0.3$ (red) and $K = 0.35$ (blue) for bi-chaos ($\alpha = 1$, $\beta = -1.2$) with unperturbed region width $W_{un} = 12.5$. Top: perturbation applied at $t = 200$, bottom: perturbation applied at $t = 2,000$. The system period depends on the strength K of the perturbation For early perturbation and lower running times the system forms periodic repeating patterns. For longer time runs the system transitions into imperfect repeating pattern with a consistent highest Fourier peak.

4.3 Conclusions and outlook

In this chapter we have shown numerically that applying a time-delayed feedback scheme to only part of the system can stabilize spatially localized periodic space-time patterns for for a chaotic system described by the complex Ginzburg-Landau equation. We discussed three cases, corresponding to amplitude turbulence, phase turbulence and bi-chaos. Using localized perturbations we have shown that we can take behavior from different regimes [74] and impose similar behavior in isolated spatial regions.

The results presented show that the interplay between diffusion across the boundaries separating the perturbed and unperturbed regions yields transition regions. These transition regions interact with time-delayed feedback perturbations to form and sustain periodic cycles. The values of the linear and nonlinear dispersion play a significant role for applying perturbations. For amplitude turbulence the closer the dispersion values are to the Benjamin-Feir-Newell limit, ($\alpha\beta = -1$), the more robust the system is for perturbation producing parameters. Phase turbulence has close proximity to the Benjamin-Feir-Newell limit and stable plane wave solutions. This is a plausible explanation to the broad range of system widths and perturbation strengths that generate periodic structures. For bi-chaos the parameter space location is between different chaotic regimes [30, 84]. The second shift in long-term behavior after a perturbation is applied can be a result of the competing dynamics between the phase and amplitude.

The use of time-delayed feedback has been shown experimentally to stabilize unstable periodic orbits of chaotic systems [76, 77, 78, 79, 80]. As we have shown, localized patterns can be stabilized through spatially localized time-delayed feedback within chaotic systems. The results presented here aim to start building the guiding framework for experiments to investigate the interactions of different spatially localized regions within chaotic parameter spaces.

Chapter 5

Conclusions and perspectives

The purpose of this study was to increase the understanding of the effects of applying spatially localized perturbations to systems exhibiting spatio-temporal patterns. The main focus has been on systems with chaotic regimes. We presented two studies investigating the effects of spatially localized perturbations on chaos producing models. Chapter 2 is focused on the analysis techniques necessary to understand the core results of the model specific Chapters 3 and 4. Chapter 3 presented the spatio-temporal patterns emerging from a spatially localized time-delayed feedback scheme for transient chaos within the framework of the the Gray-Scott model. Chapter 4 presented novel spatio-temporal patterns emerging from a spatially localized time-delayed feedback scheme for sustained chaos using the one-dimensional cubic complex Ginzburg-Landau equation.

We have shown that applying time-delayed feedback to only part of a chaos producing system may create novel spatially localized space-time patterns. We discussed two models with several cases for each model. The method presented works for both transient and sustained chaos. In general the surrounding behavior regimes within the models parameter space will determine where the perturbation is most impactfully applied. In this context, enhancing the substrate flow rate for the Gray-Scott model will take the system to a mutual coexistence regime of behavior. This can be accomplished by either changing the substrate flow parameter or using a time-delayed feedback on the substrate. Changing the substrate flow value without applying feedback will not give fluctuating interactions across the region boundaries. This feature of time-delayed feedback perturbations gives a self stabilizing effect to the system which allows the formation of perfect periodic patterns.

For the Gray-Scott model we discussed two cases, one leading to perfect periodic pattern in the unperturbed part of the system, the other leading to imperfect oscillations in the perturbed region. The creation of these patterns turns out to be robust and is encountered for a broad range of system parameters. Our study reveals that the needed ingredient is the diffusion across the boundaries separating the perturbed and unperturbed regimes which yields a transition region, straddling the boundary, that is necessary to stabilize the

spatially localized oscillations.

For the cubic complex Ginzburg-Landau equation we discussed three parameter space regimes, two leading to consistent periodic patterns in the unperturbed part of the system, the other leading to imperfect oscillations in the unperturbed region. For one of the perturbed parameter space regimes, phase turbulence, the creation of patterns turns out to be robust and is encountered for a broad range of system parameters. For two of the regimes, amplitude turbulence and bi-chaos, the perturbation region width has limited ranges for which periodic patterns will form. As with the transient chaos the diffusion induced transition region plays a vital role in stabilization of periodic patterns. The values of the linear and nonlinear dispersions play a significant role for applying perturbations. For amplitude turbulence the closer the dispersion values are to the Benjamin-Feir-Newel line, the more robust the system is for perturbation producing parameters. Phase turbulence has close proximity to plane wave producing regimes. This is a plausible explanation to the broad range of system widths and perturbation strengths that generate periodic structures. For bi-chaos the parameter space location is between chaotic regimes [30, 84]. The competing dynamics between the phase and amplitude is a likely cause of the imperfect repeating patterns.

Time-delayed feedback has been used experimentally to stabilize unstable periodic orbits of chaotic systems [76, 77, 78, 79, 80]. Our work on using time-delayed feedback in a spatially localized framework is a novel contribution to the field. We hope that our work on creating spatio-temporal patterns from a spatially localized time-delayed feedback scheme paves the way for experimental awareness and implementations of this scheme and for the investigation of the resulting spatially localized patterns. Potential future areas of research could be utilizing spatially localized perturbations in other chaos producing models such as the Swift-Hohenberg equation [85]. Another area of potential future study is quantifying the impact of site localized perturbations on the stability curves that define the parameter space features of spatially extended systems.

Bibliography

[1] M. C. Cross and P. C. Hohenberg, Rev. Mod. Phys. **65**, 851 (1993).

[2] D. Walgraef, *Spatio-Temporal Pattern Formation: With Examples from Physics, Chemistry, and Materials Science* (Springer, New York, 1997)

[3] N. Träger, P. Gruszecki, F. Lisiecki, F. Groß, J. Förster, M. Weigand, H. Głowiński, P. Kuświk, J. Dubowik, G. Schütz, M. Krawczyk, and J. Gräfe, Phys. Rev. Lett. **126**, 057201 2021

[4] F. X. Hu, G. X. Wu, G. X. Song, Q. R. Yuan, and S. Okamura, Astrophys. Space Sci. **302**, 43 (2006).

[5] M. Einasto, L. J. Liivamägi, E. Tempel, E. Saar, E. Tago, P. Einasto, I. Enkvist, J. Einasto, V. J. Martínez, and P. Heinämäki, Astrophys. J. **736**, 51 (2011).

[6] I. Mutabazi, J.E Wesfreid, and E. Guyon, (eds.) *Dynamics of Spatio-Temporal Cellular Structures: Henri Benard Centenary Review*, in Springer Tracts in Modern Physics **207** (Springer,Berlin, 2006).

[7] E. Ott, C. Grebogi, and J. A. Yorke, Phys. Rev. Lett. **64**, 1196 (1990).

[8] K. Pyragas, Phys. Lett. A **170**, 421 (1992).

[9] M. E. Bleich and J. E. S. Socolar, Phys. Rev. E **54**, R17 (1996).

[10] S. Boccaletti, C. Grebogi, Y.-C. Lai, H. Mancini, and D. Maza, Phys. Rep. **329**, 103 (2000).

[11] E. Schöll and H. G. Schuster (Editors), *Handbook of Chaos Control: Foundations and Applications* (Wiley-VCH, Weinheim, 2008).

[12] Y. N. Kyrychko, K. B. Blyuss, S. J. Hogan, and E. Schöll, Chaos **19**, 043126 (2009).

[13] A. L. Fradkov, Phil. Trans. R. Soc. A **375**, 20160223 (2017).

[14] D. W. Sukow, M. E. Bleich, D. J. Gauthier, and J. E. S. Socolar, Chaos **7**, 560 (1997).

[15] S. Bielawski, D. Derozier, and P. Glorieux , Phys. Rev. A **47**, R2492 (1993).

[16] K. Hall, D. J. Christini, M. Tremblay, J. J. Collins, L. Glass, and J. Billette, Phys. Rev. Lett. **78**, 4518 (1997)

[17] Th. Pierre, G. Bonhomme, A. Atipo, Phys. Rev. Lett. **76**, 2290 (1996).

[18] E. Benkler, M. Kreuzer, R. Neubecker, and T. Tschudi, Phys. Rev. Lett. **84**, 879 (2000).

[19] P. Parmananda, R. Madrigal, M. Rivera, L. Nyikos, I. Z. Kiss, and V. Gáspár, Phys. Rev. E **59**, 5266 (1999).

[20] A. Gjurchinovski and V. Urumov, Rom. J. Phys. **58**, 36 (2013).

[21] M. Tlidi, A. G. Vladimirov, D. Turaev, G. Kozyreff, D. Pieroux, and T. Erneux, Eur. Phys. J. D **59**, 59 (2010)

[22] M. G. Clerc, S. Coulibaly, and M. Tlidi, Phys. Rev. Res. **2**, 013024 (2020).

[23] T. G. Seidel, J. Javaloyes, and S. V. Gurevich, Chaos **32** (2022).

[24] E. E. Sel'kov, Eur. J. Biochem. **4**, 79 (1968).

[25] P. Gray and S. K. Scott, Chem. Eng. Sci. **39**, 1087 (1984).

[26] P. Gray and S. K. Scott, *Chemical Oscillations and Instabilities: Non-linear Chemical Kinetics* (Oxford University Press, Oxford, 1990).

[27] W. Mazin, K. E. Rasmussen, E. Mosekilde, P. Borckmans, and G. Dewel, Math. Comput. Simul. **40**, 371 (1996).

[28] I. S. Aranson and L. Kramer, Rev. Mod. Phys. **74**, 99 (2002).

[29] S. Boccaletti, J. Bragard, and F.T. Arecchi, Phys. Rev. E **59**, 6574 (1999).

[30] S. Boccaletti and J Bragard, Phil. Trans. R. Soc. A. **364**, 2383 (2006).

[31] S. H. Strogatz, *Nonlinear dynamics and chaos: with application to physics, biology, chemistry, and engineering* (Westview press, 2000).

[32] K. Alligood, T.D. Sauer, J.A. Yorke, *CHAOS: An Introduction to Dynamical Systems* (Springer-Verlag, New York, 1996).

[33] Y.-C. Lai and T. Tél, *Transient Chaos: Complex Dynamics on Finite Timescales* in Applied Mathematical Sciences Vol. 173 (Springer, New York, 2011).

[34] R. Wackerbauer and K. Showalter, Phys. Rev. Lett. **91**,174103 (2003)

[35] J. Gleick, *Chaos. Making a New Science* (Viking, New York. 1987).

[36] J. M. T. Thompson, and H. B. Stewart, *Nonlinear dynamics and chaos* (Chichester: Wiley 1986).

[37] F. C. Moon, *Chaotic and fractal dynamics* (New York: Wiley 1992).

[38] J.D Hoffman, and S. Frankel, *Numerical methods for engineers and scientists* (CRC press, 2018).

[39] J. Crank, *The mathematics of diffusion* (Oxford University press, 1979).

[40] T. Sauer, *Numerical Analysis* (Addison Wesley, Boston, MA, 2006).

[41] Y. Nishiura and D. Ueyama, Forma **15**, 281 (2000).

[42] Y. Nishiura and D. Ueyama, Physica D **150**, 137 (2001).

[43] N. Parekh, V. Ravi Kumar, and B. D. Kulkarni, Phys. Rev. E **52**, 5100 (1995).

[44] J. T. Betts, *Practical methods for optimal control and estimation using nonlinear programming* (Society for Industrial and Applied Mathematics, 2010).

[45] A. Quarteroni, F. Saleri, and P. Gervasio. *Scientific computing with MATLAB and Octave*, Vol. 3. Berlin: Springer, 2006.

[46] D. Ueyama, Hokkaide Mathematical Journal **28**, 175 (1999).

[47] F. Mahootian, D. J. Lauri, and J. E. Earley, J. Phys. Chem., **96** , No. 3, 1014-1015(1992).

[48] K. B. Yatsimirskii and P. E. Strizhak, Theor. Exp. Chem. **28**, 293 (1993).

[49] J. Czak and M. Pleimling, Phys. Rev. E **104**, 064213 (2021).

[50] M. Matsushita, J. Wakita, H. Itoh, I. Ràfols, T. Matsuyama, H. Sakaguchi, and M. Mimura, Physica A **249**, 517 (1998).

[51] H. Meinhardt, Curr. Top. Dev. Biol. **81**, 1 (2008).

[52] A. De Wit, Adv. Chem. Phys. **109**, 435 (1999).

[53] A. M. Turing, Phil. Trans. R. Soc. B **237**, 37 (1952).

[54] V. S. Zykov, G. Bordiougov, H. Brandtstädter, I. Gerdes, and H. Engel, Phys. Rev. Lett. **92**, 018304 (2004).

[55] A. S. Mikhailov and K. Showalter, Phys. Rep. **425**, 79 (2006).

[56] V. K. Vanak and I. R. Epstein, Chaos **18**, 026107 (2008).

[57] S. V. Gurevich, Phys. Rev. E **87**, 052922 (2013).

[58] J. Löber and H. Engel, Phys. Rev. Lett. **112**, 148305 (2014).

[59] R. O. Grigoriev, M. C. Cross, and H. G. Schuster, Phys. Rev. Lett. **79**, 2795 (1997).

[60] B. Fiedler, V. Flunkert, M. Georgi, P. Hövel, and E. Schöll, Phys. Rev. Lett. **98**, 114101 (2007).

[61] M. Kehrt, P. Hövel, V. Flunkert, M. A. Dahlem, P. Rodin, and E. Schöll, Eur. Phys. J. B **68**, 557 (2009).

[62] G. Brown, C. M. Postlethwaite, and M. Silber, Physica D **240**, 859 (2011).

[63] W. N. Reynolds, J. E. Pearson, and S. Ponce-Dawson, Phys. Rev. Lett. **72**, 2797 (1994).

[64] I. Berenstein, Chaos **25**, 064301 (2015).

[65] P. Gandhi, Y. R. Zelnik, and E. Knobloch, Phil. Trans. R. Soc. A **376**, 20170375 (2018).

[66] J. E. Pearson, Science **261**, 189 (1993).

[67] C. B. Muratov and V. V. Osipov, Eur. Phys. J. B **22**, 213 (2001).

[68] F. Lesmes, D. Hochberg, F. Morán, and J. Pérez-Mercader, Phys. Rev. Lett. **91**, 238301 (2003).

[69] P. Hanggi,P. Jung, *Colored noise in dynamical systems*, Adv. Chem. Phys. **89**, (1995).

[70] G. E. Uhlenbeck and L. S. Ornstein, Phys. Rev. **36**, 823 (1930.)

[71] D. T. Gillespie, Phys. Rev. E **54**, 2084 (1996).

[72] H. M. Taylor, and S. Karlin, *An Introduction to Stochastic Modeling* (Academic Press, San Diego, 1984)

[73] M. A. Pinsky, and S. Karlin. *An Introduction to Stochastic Modeling* (Academic Pres, Oxford, 2010).

[74] M. Bazhenov, M. Rabinovich, and L. Rubchinsky, J. Stat. Phys. **83**, 1165 (1996).

[75] J. Czak and M. Pleimling, in preparation.

[76] K. Pyragas and A. Tamaševičus, Phys. Lett. A **180**, 99 (1993).

[77] W. Just, E. Reibold, and H. Brenner, in *Proceedings of the 5th Experimental Chaos Conference*, edited by M. Ding, W. L. Ditto, L. M. Pecora, and M. L. Spano, 67 (2001).

[78] O. V. Popovych, C. Hauptmann, and P. A. Tass, Phys. Rev. Lett. **94**, 164102 (2005).

[79] K. Yamasue, K. Kobayashi, H. Yamada, K. Matsushige, and T. Hikihara, Phys. Lett. A **373**, 3140 (2009).

[80] T. Jüngling, A. Gjurchinovski, and V. Urumov, Phys. Rev. E **86**, 046213 (2012).

[81] L. Brusch, M. G. Zimmermann, M. van Hecke, M. Bär, and A.Torcini, Phys. Rev. Lett. **85**, 86 (2000).

[82] Y. Kuramoto, *Chemical Oscillations, Waves, and Turbulence* (Springer, Berlin, 1984).

[83] J. Bragard, S. Boccaletti, and F.T. Arecchi, Int. J. Bifurcation Chaos Appl. Sci. Eng.**11**, 2715 (2001).

[84] J. Bragard, S. Boccaletti, C. Mendoza, H. G. E. Hentschel, and H. Mancini, Phys. Rev. E **70**, 036219 (2004).

[85] A. Hariz, L. Bahloul, L. Cherbi, K. Panajotov, M. Clerc, M. A. Ferré, B. Kostet, E. Averlant, and M. Tlidi, Phys. Rev. A **100**, (2019).

[86] D. Puzyrev, S. Yanchuk, A. G. Vladimirov, and S. V. Gurevich, SIAM J. Appl. Dyn. Syst. **13**, 986 (2014).

[87] R. Faller and L. Kramer, Phys. Rev. E **57**, R6249 (1998).

[88] L. Junge and U. Parlitz, Phys. Rev. E **61**, 3736 (2000).

[89] C. C. Ballard, C. C. Esty, and D. A. Egolf, Chaos **26**, 113101 (2016).

[90] B. I. Shraiman, A. Pumir, W. van Saarloos, P. C. Hohenberg, H. Chate, and M. Holen, Physica D **57**, 241 (1992).

[91] J. Wolff, A. G. Papathanasiou, H. H. Rotermund, G. Ertl, X. Li, and I. G. Kevrekidis, Phys. Rev. Lett. **90**, 018302 (2003).

[92] H. Nakao, T. Yanagita, and Y. Kawamura, Phys. Rev. X **4**, 021032 (2014).